Effects of compositions and mechanical milling modes on hydrogen storage properties

Zhenguo Huang
University of Wollongong

Effects of compositions and mechanical milling modes on hydrogen storage properties

A thesis submitted in fulfilment of the requirements
for the award of the degree

Doctor of Philosophy

from

University of Wollongong

by

Zhenguo Huang B. Eng., M. Eng.

Institute for Superconducting and Electronic Materials

August 2007

Declaration

I, Zhenguo Huang, hereby certify that the work presented in this thesis is original and was carried out at the Institute for Superconducting and Electronic Materials, the University of Wollongong, New South Wales, Australia. To the best of my knowledge and belief this thesis contains no material previously published or written by another person, except where otherwise acknowledgement and references have been made in the thesis. This work has not been submitted previously, in part or in whole, to qualify for any other degree.

Zhenguo Huang

Acknowledgements

First and foremost, I would like to thank my principal supervisor, Professor Huakun Liu, for providing timely and insightful advice, financial and spiritual support, and encouragement above and beyond the call of duty during this work. I would also like to thank my co-supervisors, Dr. Zaiping Guo and Dr. Andrzej Calka, for their invaluable assistance and guidance. Without their help I would never have finished this work. All my supervisors' implicit trust in my research abilities not only allowed me to freely pursue my goals, but also gave me an opportunity to learn how to manage time and allocate resources. Special thanks go to Professor Shixue Dou, for his inspiration, generosity, and insightful instruction.

I would also like to express my appreciation to all other staff members, particularly Dr. Xiaoling Wang, Dr. Konstan Konstantinov, Dr. Jiazhao Wang, Dr. Guoxiu Wang, and Mr. Ron Kinnel, for their genuine help in many regards. Special thanks go to Dr. Tania Silver, who patiently provided thorough error checking of my papers with detailed explanations. Thank you also to my fellow work colleagues, Germanas Peleckis, Scott Needham, Ng See How, Xu Xun, and Olga Shcherbakova, whose knowledge and experience proved very helpful in this research. I would like to thank Brad Winton, in particular. Thank you very much for the informative, impassioned, and enjoyable discussions that we had together.

I would also like to thank my colleagues on the University Council, Vice-Chancellor Professor Gerard Sutton, Mr. Chris Grange, Professor Rob Castle, Professor John Patterson, Professor Margaret Sheil, and Professor Lee Astheimer. Their impressive managerial skills, marvelous strategic thinking abilities, brilliant leadership, accessible to only one postgraduate, me, in this university over the past two years, really broadened my horizons and enriched my experience.

To my great parents, I am forever indebted to their non-stop financial and spiritual support---I could never have asked for better parents. My dear Mum and Dad, I love you forever.

Most importantly, I wish to express my gratitude to my wife, Limei Yang. Her unfailing love, patience, perseverance, and encouragement enabled me to really concentrate on my study. Limei, I am extremely grateful for your love. Thank you.

List of Tables

List of Figures

Table of Contents

Abstract

The objectives of this work are to further enhance the hydrogen storage properties of some promising candidate materials and to investigate the impact of milling mode on the hydrogen storage properties.

$Mg_{1.9}Cu_{0.1}Ni_x$ (x = 1.8, 1.9, 2.0, and 2.1) alloys were synthesized using a high-energy Spex 8000 ball mill. The effects of nickel content on the thermal stability and on the hydrogenation of the alloys are discussed. It was found that the nickel content affects the recrystallization of the predominately amorphous alloys, and as a result, affects the formation of Mg_2NiH_4.

The $Mg_{1.9}Cu_{0.1}Ni_x$ (x = 1.8, 1.9, 2.0, and 2.1) alloys were also investigated with respect to the electrochemical performance. Ni was found to be effective in maintaining the reversibility and discharge capacity of the alloy electrodes.

With the aim of improving the hydrogen cycling properties of magnesium, two types of catalysts were studied. In order to investigate the differences in the catalysis arising from the respective valence states of a transition metal in the oxides, two types of iron oxides, i.e. Fe_2O_3 and Fe_3O_4, were ball milled with Mg in hydrogen using the low-

energy shearing mode of a Uni-Ball-Mill 5, as discussed below. The hydrogen cycling properties of the ball-milled composites were studied. There was little difference in the hydrogen absorption and desorption kinetics of the two composites, which is presumably due to the reduction reaction occurring during hydrogen cycling.

Three carbon allotropes with very different structure, i.e. graphite, carbon black, and multiwalled nanotubes, were also tried as catalysts. Although the graphitic structure experienced the most disruption, graphite showed a noticeable catalytic effect by improving the hydrogen absorption and desorption kinetics of Mg. The possible origins of the enhancement are probed.

In order to investigate the effects of milling energy on the hydrogen storage properties, a special mill was used, the Uni-Ball-Mill 5, which allows the control of the movements of the grinding balls. Two milling modes, a high-energy impact mode and a low-energy shearing mode can be realized through the adjustment of the attached external magnet.

Graphite, a very interesting material for hydrogen storage, was studied in particular. The influence of the different milling modes on the hydrogen absorption and storage capacity is discussed. It was found that there is a strong correlation between the composition of the milled graphite and the milling mode. As a result, different thermal behaviors were observed for the respective samples.

Boron was milled in hydrogen using both low-energy shearing and high-energy impact. The amount of hydrogen trapped during milling is dependent on the milling mode. The thermal behaviors were also different for the respective samples.

Key words: hydrogen storage, ball milling, nanocrystalline, graphite, magnesium, boron, nickel, carbon, catalyst

Chapter 1

Introduction

There are several crucial forces driving the pursuit of the “hydrogen economy”. Firstly, carbon-based natural resources, such as oil, natural gas, and coal, will definitely be depleted one day. In the long-term view, humanity has to find an effectively inexhaustible energy resource. Secondly, human being are suffering and very likely will continuously suffer the ramifications of using such carbon-based energy resources, i.e. global warming, which causes severe droughts, heavy precipitation, tropical cyclones, etc. Therefore, the new energy resource should be friendly to the environment. Finally, the increasing world population and scale of the economy demands more energy than ever.

The term “hydrogen economy” depicts a society powered by pollution-free energy. In that society, almost everything, from large scale manufacturing and transportation to small portable devices, will be powered by hydrogen, using fuel cells or combustion engines. Hydrogen production can take advantage of wind, solar, tidal, and geothermal forms of energy, which are sustainable and environmentally friendly.

In order to use hydrogen safely and economically, a proper storage method should be available to supply fuel upon demand. Considering the importance of transportation and the applicability of hydrogen in this sector, the U.S. Department of Energy (DOE) has issued updated holistic requirements for on-board hydrogen storage (DOE 2007). The requirements specify the storage capacity, gravimetric density, volumetric density,

hydrogen absorption and desorption kinetics, heat transfer, lifetime, and safety. So far, there is no single storage method meeting all the criteria.

The majority of current hydrogen storage methods are reviewed in Chapter 2. The review covers the strengths and weaknesses of each method. Attempts that have been made to improve the performance of each method are briefly discussed. The factors affecting the hydrogen storage properties are also summarized. The chapter closes with a review of the methods applied to synthesize and modify hydrogen storage materials.

Chapter 3 lists the materials used in my PhD study, including chemicals, gases, and equipments. It also describes the experiments carried out to obtain the results.

The Mg-based system has attracted intensive attention since: 1) the system has a high storage capacity, i.e. 7.6 wt. % for MgH_2 and 3.6 wt. % for Mg_2Ni; 2) the costs of the materials are low; and 3) the synthesis is simple, mainly by ball milling. Therefore, the Mg-based system is the subject of the main part of the thesis.

Mg_2Ni has a storage capacity of 3.6 wt. %, higher than most of the well known intermetallic alloys, such as AB type compounds, for which the paradigm is $TiFeH_2$, containing 1.9 wt. % hydrogen, and AB_5 type compounds, for which the paradigm is $LaNi_5H_6$, containing 1.5 wt. % hydrogen. However the absorption and desorption temperatures of coarser-grained Mg_2Ni are higher, and the hydrogen cycling kinetics is slow. By forming an amorphous and non-stoichiometric system through substitution and ball milling, significant improvements have been made (Nam and Lee 2002, Yang et al. 2002, and Song et al. 1999). Therefore, in Chapter 4, mechanical alloying was applied

to synthesize amorphous non-stoichiometric $Mg_{1.9}Cu_{0.1}Ni_x$ (x = 1.8, 1.9, 2.0, and 2.1) alloys. The thermal stability and hydrogen storage properties of the alloys are discussed in relation to the nickel content.

Mg_2Ni is a potential electrode material since it has the high theoretical discharge capacity of 999 $mAhg^{-1}$. However, the capacity can not be realized for conventional polycrystalline Mg_2Ni. In addition, the cyclic performance is very poor, due to the formation of $Mg(OH)_2$ in an alkaline solution. Substituting Mg and/or Ni (Iwakura et al. 2001), reducing the grain size (Woo and Lee 1999), and amorphizing the structure (Iwakura et al. 1998) have all been found effective to improve the electrochemical performance. The electrochemical performance of $Mg_{1.9}Cu_{0.1}Ni_x$ (x = 1.8, 1.9, 2.0, and 2.1) alloys is investigated in Chapter 5. The effects of Ni in relation to the discharge capacity and cyclic performance of the alloy electrodes are discussed.

Although MgH_2 contains 7.6 wt. % hydrogen, its thermodynamic stability impedes its real world application. Through surface modification, nanocrystallization, and combination with catalysts, the hydrogen storage properties have been dramatically enhanced (Song et al. 2004, Holtz and Imam 1999, and Yavari et al. 2005). Transition metal oxides (TMOs) such as Nb_2O_5 (Hanada et al. 2005), V_2O_5, and Fe_3O_4 (Oelerich et al. 2001) have been identified as effective catalysts in improving the hydrogen cycling performance of Mg. In Chapter 6, studies on Fe_2O_3 and Fe_3O_4 are reported, with the aim being to identify the effects on the hydrogen cycling properties of Mg of differences in catalysis that arise from the different valence states of Fe.

Carbon allotropes, such as graphite (Imamura et al. 2003), carbon nanotubes (Wu et al. 2006), and carbon nanofibres (Lukashev et al. 2006), have also been studied as catalysts to improve the hydrogen cycling properties of Mg. It was found that the graphite significantly improves both the hydrogen absorption and desorption kinetics (Imamura et al. 2003) only when the integrity of the graphitic structure is maintained after ball milling. Chapter 7 discusses how three types of carbon: graphite, carbon black, and multiwalled carbon nanotubes, were ball milled with Mg in hydrogen using the low-energy milling mode of a Uni-Ball-Mill 5 (Calka and Radlinski 1991). Investigations on the respective catalytic effects were carried out. The observed enhancements in the hydrogen cycling performance of Mg that are associated with the presence of graphite are discussed.

The properties of a milled product are dependant on a variety of milling factors, such as the nature of milling equipment, the milling speed, the duration, the weight ratio of balls to powder, etc. (Huot et al. 2001). Conventional high-energy Spex 8000 and planetary Fritsch mills are widely used to fabricate and modify hydrogen storage materials. In both mills the movements of the balls are difficult to control. Uni-Ball-Mill 5 is a mill that allows the control of the movements of grinding balls (Calka and Radlinski 1991). A high-energy impact mode and low-energy shearing mode can both be realized. As a result, the properties of the ball-milled products using the two modes are expected to be different.

Graphite itself has been studied intensively as a hydrogen storage medium. However, the reported storage capacities are spread out widely, from 0 to 7 wt. % (Kajiura et al. 2003, Orimo et al. 2001, Awasthi et al. 2002, Isobe et al. 2004, and Ichikawa et al.

2004). Most of the experiments have been carried out by ball milling graphite using Spex 8000 or Fritsch mills. In Chapter 8, the high-energy impact and low-energy shearing modes of the Uni-Ball-Mill 5 are applied to mill graphite in hydrogen. The observed differences associated with the different milling modes are investigated.

Boron is a crucial element in some very promising hydrogen storage materials, such as $LiBH_4$ and $NaBH_4$. Nanostructured boron nitrides, in the form of nanotubes, nanocages, etc., have been studied with respect to their hydrogen storage capacities (Oku et al. 2001 and 2002). Boron can form a variety of polyhedral boranes by covalent bonding (Grimes 2004). By ball milling boron in hydrogen, a certain amount of hydrogen can be stored by boron (Wang et al. 2003 a). Chapter 9 reports on how the high-energy impact and low-energy shearing modes of the Uni-Ball-Mill 5 were applied to mill boron in hydrogen. The effects of the different milling modes on the hydrogen storage capacities of boron are investigated.

Finally, the main results of the research are summarized in Chapter 10, followed by the list of references. The thesis closes with the list of papers published during my PhD study.

Chapter 2

Literature review

2.1 Background

Energy is essential to our way of life, to the economy, and to the national security. The pursuit of economic growth and a better quality of life is the driving force for global energy demands. The global economy is expected to double in size by 2030, and at the same time, world population is expected to reach 8 billion (World Bank 2004). Both these types of growth will have a dramatic impact on energy demand. By 2030, the world's energy needs will increase almost 50 % from the 2005 level, according to Exxon Mobil's prediction (2006).

Oil, natural gas, and coal are the predominant components in the global energy sector. In 2003, they constituted 35 %, 21 %, and 24 %, respectively (IEA 2005). This gives rise to the following challenges and questions: are there inexhaustible oil, gas, and coal in the earth? If not, how long will they last? It is hard to give an accurate peak oil prediction, as can be seen from the different figures published by different organizations. However, the fact that the oil industry is spending more money and using all available high technologies to explore for oil in unfavorable areas, such as the Arctic Ocean and Caspian Sea, might be interpreted as the industry's admission of the fact that ever less oil is to be found at other (easier to access) places (L-B-Systemtechnik GmbH 2003).

The upcoming depletion of natural carbon-based energy resources is not the only factor forcing us to exploit other energy resources. Global warming, which is due to the dramatically increased global atmospheric concentrations of carbon dioxide, methane, and nitrous oxide as a result of human activities since 1750 (Fig. 2.1, IPCC 2007), is another driving force. Global warming alters the energy balance of the climate system, which results in

- rising average sea level,
- diminishment in snow cover and ice sheets,
- changes in wind patterns and rainfall,
- frequent extreme weather, including droughts, heavy precipitation, and tropical cyclones.

People all over the world have already experienced these severe impacts. The inhabitability and sustainability of the earth will be totally destroyed if the global warming situation deteriorates.

Therefore, humanity has to seek new energy resources that are renewable in nature and clean for the environment.

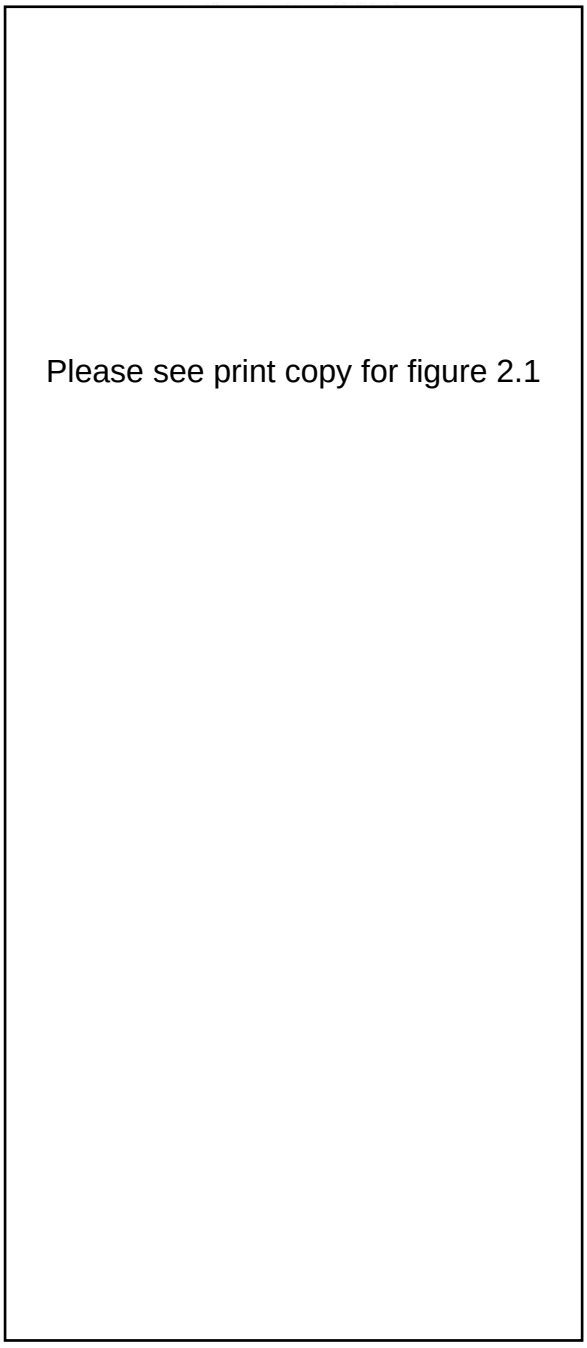

Fig. 2.1. Atmospheric concentrations of carbon dioxide, methane, and nitrous oxide over the last 10,000 years (large panels) and since 1750 (inset panels). The corresponding radiative forcings are shown on the right hand axes of the large panels (IPCC, 2007).

There are many energy resources that have the characteristics of being renewable and clean, such as hydropower, geothermal, wind, and solar. However, their total

contribution to energy consumption was less than 10 % in 2003 (IEA 2005). All these energy sources have their own advantages and disadvantages.

Hydropower is reliable, efficient, and cheap compared with geothermal, nuclear, wind, and solar energy. More important, it is very clean, with almost no air emissions. Today, hydropower provides 20 % of the electricity used by the whole world (IEA 2005). The problem with hydropower is its impact on the ecosystems where the generators are based. With proper location, design, and operation, this impact can be largely reduced.

Geothermal energy is using the heat beneath the surface of the earth. Although there is almost inexhaustible heat inside the earth, the usable geothermal energy is very “site specific”, which means that it is possible only in a few places under unique geological conditions.

Wind and solar account for only a small share, but they have been attracting the attention of politicians and business for some time. The beauty of these two energy resources is that they are carbon-free and inexhaustible in nature, which perfectly matches the current energy criteria. With foreseeable technological breakthroughs, they can be used to generate electricity at a price comparable with carbon-fired electricity. This can dramatically reduce greenhouse gas emissions. The main drawback is that they are not available all the time. However, this can be solved if there is some energy carrier to store the energy produced by them. The traditional means to store electricity is by using batteries. However, the limited capacity, high cost, and short life cycle make it unfeasible to store large amounts of electricity. Hydrogen generated using wind and

solar energy is a promising candidate. When the wind speed is very low, or the sunlight disappears, hydrogen can be used to generate energy to maintain the supply level.

2.2 Hydrogen economy

2.2.1 Why hydrogen?

As discussed above, humanity has to exploit renewable and environmentally friendly energy resources to meet the major energy challenges for the future. However, all the renewable and clean energy resources such as wind and solar can not maintain the same level of output over a long time. The intermittent energy production can not meet the demands of intensive human activities. Using hydrogen as the primary energy carrier, energy from all kinds of resources can be stored safely, efficiently, and in an almost unlimited quantity. When required, the chemical energy carried by hydrogen can be transformed into electrical energy. The electrical power can be tailored to a great variety of applications: from large-scale manufacturing, to transportation vehicles and to small consumer devices like mobile telephones and laptop computers (US DOE 2004). Finally, hydrogen is the third most abundant element in the world, and it can be really inexhaustible if it can be produced from water economically. Hence come the questions: how to produce hydrogen, i.e. store energy chemically by hydrogen; how to store and/or transport hydrogen, i.e. deliver energy; and how to use hydrogen, i.e. release energy?

2.2.2 How to produce hydrogen?

Minimizing impacts on the environment should be the first issue when it comes to hydrogen production. Therefore, only carbon-free hydrogen production technologies

should be exploited in the long term. For the time being, some production processes still involve greenhouse gas emissions, since these technologies are relatively mature and economical.

Electrolysis is a very traditional way to produce hydrogen. The electricity needed can come from wind, solar, hydro, and geothermal sources. Steam reforming has been widely applied in industry for producing hydrogen from natural gas. Current production is 9 million tons per year on an industrial scale in the US (US DOE 2004). Solar power can also be utilized to produce hydrogen through water electrolysis using solar cells, or by direct photocatalytic water splitting or photobiological water splitting. Currently, all of these technologies still face their respective sets of challenges, and substantial improvements in efficiency and reductions in both capital and operating costs are needed.

The CUTE (Clean Urban Transportation for Europe) project (Evobus GmbH 2006) gives a fair try to different hydrogen production methods. More than 56 % of the hydrogen produced on-site comes from renewable resources, which helps to collect invaluable real-world experience in connecting renewable energy resources with end usage via hydrogen.

2.2.3 How to use hydrogen?

Combustion engines and fuel cells are the two primary means to release the energy stored by hydrogen. In 2007, the EU endorsed the hydrogen combustion engine (Scoop 2007), which is believed to offer clear advantages over other propulsion systems in

terms of performance and costs. During the transitional period from fossil fuel to the clean hydrogen era, hydrogen can also be blended with natural gas, which generates significantly lower emissions than when operating on diesel or natural gas (Hythane 2007). Fuel cells can convert the chemical energy stored by hydrogen into electrical energy at high efficiency and with no pollution. The size of the fuel cell can be varied to meet the energy requirements of applications, from large-scale manufacturing to tiny electronic devices. There are many hydrogen fuel cell demonstration programs around the world, such as the CUTE fuel cell bus (Evobus GmbH 2006), the Ford fuel cell car (Ford 2007), and Canon fuel cell cameras (Digital Trends 2005).

2.2.4 How to store hydrogen?

Flexible use of hydrogen as an energy carrier requires a means to store hydrogen efficiently and safely. Broadly speaking, hydrogen storage needs to meet two types of energy output requirements. One is for stationary applications, such as residential heating, neighborhood electrical generation, and specific applications in many industries. This type of application requires a storage method that suits operation at high temperature and pressure with extra capacity. The other type is related to mobile applications, such as portable devices and transportation, which need a hydrogen storage method with high hydrogen volume density and weight density. Transportation, for instance, requires a hydrogen storage method that occupies the minimum space in the vehicle, supplies enough hydrogen to enable a decent driving range, charges/recharges near room temperature, and provides hydrogen at rates fast enough for fuel cells. The hydrogen storage requirements for transportation applications are far more stringent and difficult to achieve than those for stationary applications.

Considering the high contribution to greenhouse gas emissions from transportation, i.e. 24 % for the EU in 2004 (EEA 2006) and 33 % for the US in 2003 (Greene and Schafer 2003), finding suitable onboard hydrogen storage solutions for transportation applications is an important step towards the carbon-free hydrogen economy.

2.3 Requirements for hydrogen storage

On a weight basis, hydrogen (120 MJ/Kg) has nearly three times the energy content of gasoline (44 MJ/kg). However, on a volume basis, hydrogen (8 MJ/L) has only a quarter of the energy content of gasoline (32 MJ/L) (Satyapal et al. 2007). Therefore, the volumetric energy density of hydrogen storage on board should be high enough in order to avoid encroaching on the passenger and cargo space, and at the same time, to achieve a driving distance comparable with vehicles fuelled by gasoline. The weight of the storage system should also be appropriate, without imposing an unnecessary load. Considering the huge market represented by the transportation industry, developing an effective hydrogen storage system is a central challenge for basic research and a key factor in enabling the success of the hydrogen economy. The US DOE (2007) issued updated operating requirements for on-board hydrogen storage (Table 2.1). In brief, it requires that an applicable hydrogen storage system should possess high storage capacity, high gravimetric and volumetric densities, fast kinetics, effective heat transfer, long life cycle, high mechanical strength and durability, safety under normal use, and acceptable risk under abnormal conditions.

Table 2.1 US DOE (2007) hydrogen storage system performance targets.

Please see print copy for table 2.1

In Fig. 2.2, most candidates currently under investigation are listed in light of the 2010 and 2015 targets (Satyapal et al. 2006). Obviously, most of them can not meet all the requirements specified in Table 2.1. Some have high volumetric density, but possess very low mass density, such as NaH and Mg_2NiH_4; while some, such as liquid hydrogen and compressed gaseous hydrogen, have high mass density, but the volumetric density

falls short of requirements. Efforts are underway to improve current storage methods and discover new materials to store hydrogen.

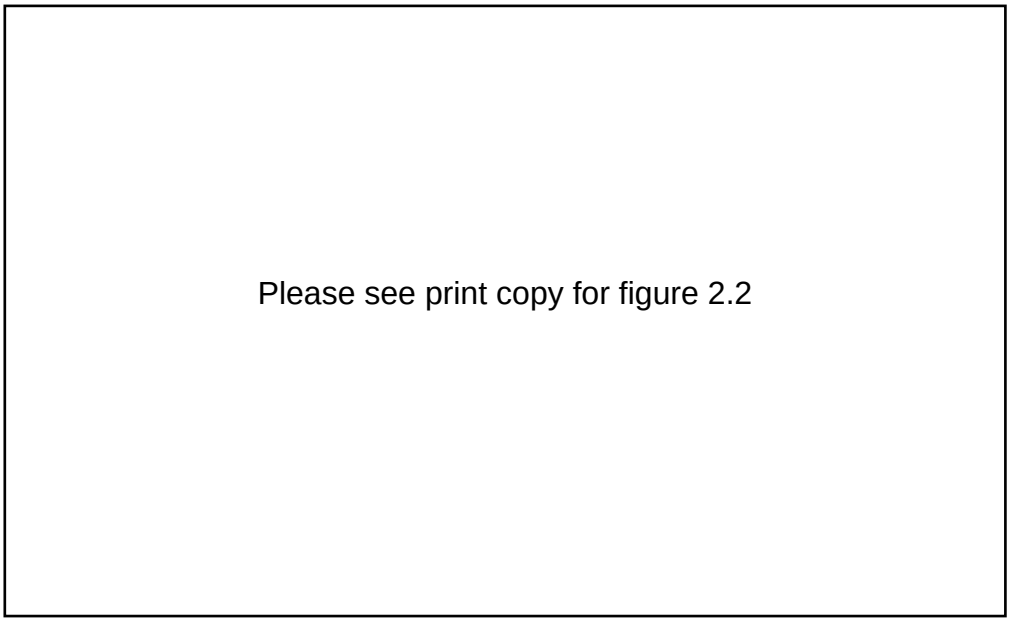

Fig. 2.2. Hydrogen density of materials (Satyapal et al. 2006).

2.4 Various hydrogen storage methods

2.4.1 Liquid hydrogen (LH_2)

By cooling the temperature to -253 ^{o}C, hydrogen gas is shrunk to a thousandth of its original volume, thus raising the energy density (Satyapal et al. 2007). LH_2 stored on board has been used to feed fuel to BMW's internal combustion engine (Zenner and Pehr 2004). LH_2 possesses two distinct properties: rapid refueling (3 min) (Hettinger et al. 1996) and extremely low heat transfer between the vessel and the environment (~1W in a 5 kg H_2 tank) (Pehr et al. 2002).

However, the maintenance of cryogenic temperatures and the flammability characteristic of hydrogen necessitate a very complicated storage system, as illustrated

in Fig. 2.3 (Green Car Congress 2006). The ***Linde*** LH_2 tank has an inner and an outer vessel, each fabricated from low-temperature-resistant materials. Between them is a super-insulated space consisting of vacuum and 70 layers of aluminum foil alternating with glass-fiber fleece. The outer vessel is mounted with an encapsulated auxiliary system, monitored by a "gas" warning system, comprising the valves, hydrogen heater, and sensors. Gaseous hydrogen is drawn from the tank once the engine starts up. As soon as the tank pressure drops beneath a given threshold, the pressure-restoration system is activated. An electric element, positioned inside the tank, heats the liquid hydrogen, which builds up the pressure to ensure enough fuel supply. There are two safety systems to prevent overpressure. If the insulation system is accidentally damaged, the resulting heat transfer will lead to intense evaporation, which will trigger the pressure-limiting safety valve. Hydrogen is then bled off. In case of failure of the pressure-limiting system, the inner tank's rupture disc breaks before pressure can overstress the tank, and the pressure is lowered in a predefined manner. This complicated structure makes the LH_2 tanks very expensive. New materials and design are needed to reduce the cost while meeting all the specifications. Safety is also an issue, even though there are safety systems attached to LH_2 tanks (Zenner and Pehr 2004). The hydrogen bled off after an accident may form an explosive mixture, which poses a potential threat to the people on board.

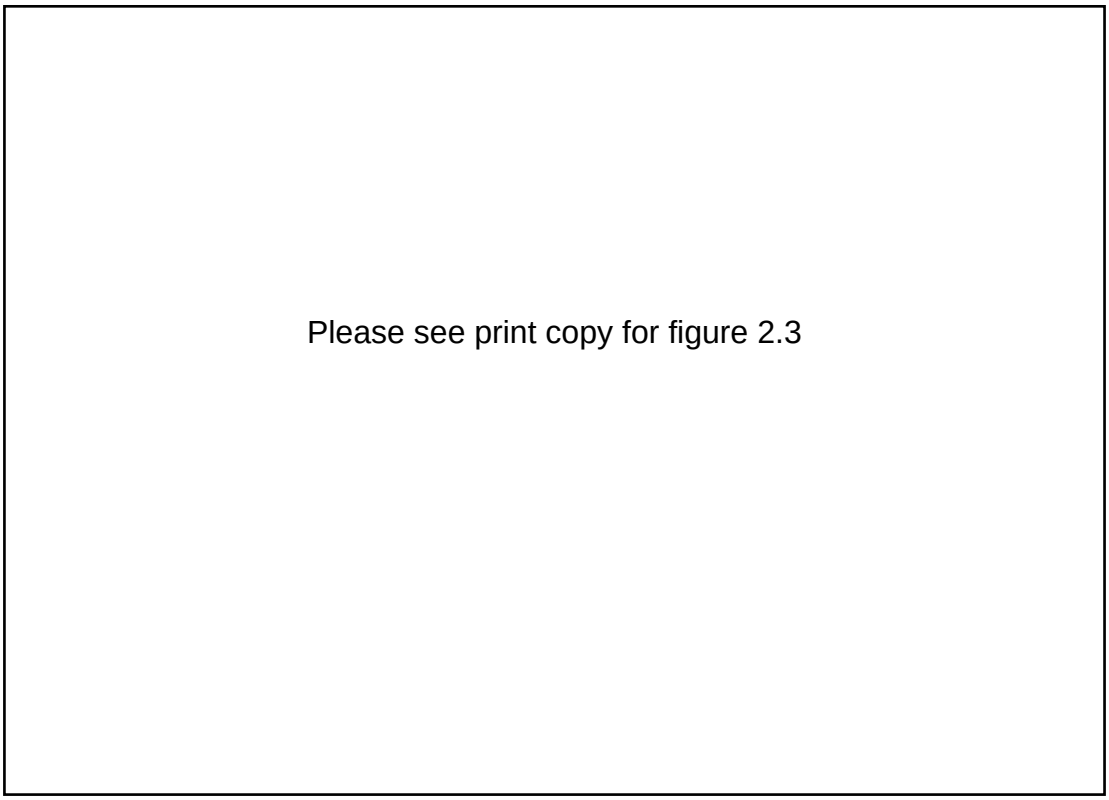

Fig. 2.3. Schematic structure of a liquid-hydrogen tank (Green Car Congress 2006).

There are other disadvantages inherent in the cryogenic storage which impede the application of LH_2. The first and greatest problem is boil-off. There are many factors affecting the hydrogen boil-off, such as the amount of hydrogen stored, the effectiveness of the thermal insulation, the ambient conditions, the geometry of the vessel, and the length of time between driving. Typical boil-off rates range from slightly less than 1 % to a few percent per day (Satyapal et al. 2007). Boil-off is an issue in terms of refueling frequency, cost, energy efficiency, and safety, particularly for vehicles parked in confined spaces such as parking garages, where the boil-off may cause damage to property and human health by forming an explosive mixture (Utgikar and Thiesen 2005). Secondly, there is inevitable energy loss due to the liquefaction process, which amounts to over 30 % of the energy available from burning the hydrogen (Satyapal et al. 2007). This dramatically reduces the net energy efficiency. Finally, LH_2

expands considerably as it warms between 20K and the critical point (33 K). Therefore, LH_2 tanks are fueled to only 85–95 % full to prevent LH_2 spills, leaving 5–15 % for vapor space (Aceves et al. 2006).

Super-insulation, high strength, and very reliable safety systems are critical aspects for cryogenic LH_2 storage. How to reduce and hopefully eliminate the fear of potential explosion due to collision in the event of accident is a huge challenge for the future, since this is not only a technical problem, but also a psychological issue.

2.4.2 Compressed gaseous hydrogen (CGH_2)

CGH_2 stored in conventional steel hydrogen cylinders (150 bar) and carbon fibre reinforced composite tanks (350 and 700 bar) is already used in prototype hydrogen fuelled vehicles (Evobus GmbH 2006 and US DOE 2005).

Compared with LH_2, the structure of CGH_2 tanks is much simpler due to the technical requirements. Since cryogenic conditions are not required, the main function of the tank is to endure high pressure and to prevent hydrogen leakage. The primary components of the ***Quantum*** 700 bar hydrogen tank (Fig. 2.4, Warner 2005) are an outer impact-resistant shell, a structural composite shell, and an inner polymer gas permeation barrier. The compressed gas can be drawn from the tank through the regulator for usage. If the inner pressure exceeds a predetermined level, the pressure relief device will be triggered, and hydrogen is bled off.

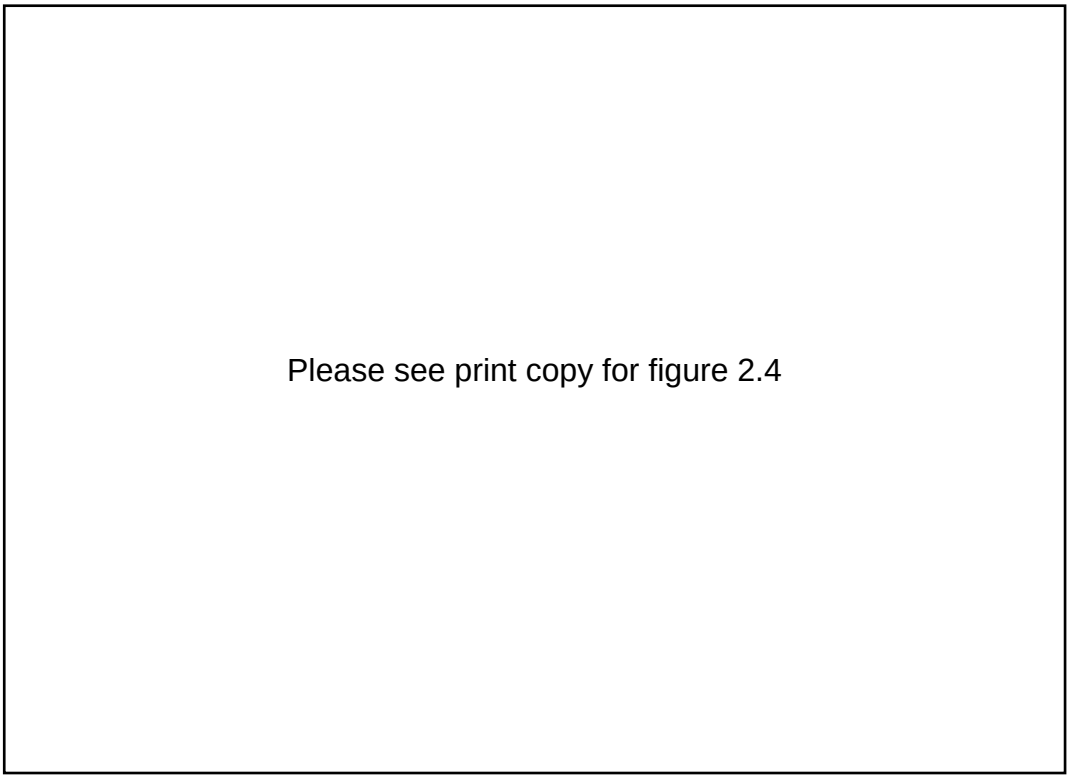

Fig. 2.4. Schematic of the compressed hydrogen Type-IV Storage Tank (Warner 2005).

CGH_2 has several distinct advantages over LH_2. Since it does not require super-insulation to maintain cryogenic conditions, the structure is less complicated and the cost of tanks is lower (Conte et al. 2001). Compressing hydrogen gas consumes 15-20 % of the heating value of hydrogen (Züttel 2004), in contrast to over 30 % for liquefaction, which improves the energy efficiency. There are also drawbacks to CGH_2, however. The volumetric capacity of CGH_2 is lower, 0.039 kg/L at 700 bar, compared with 0.07 kg/L for LH_2. Therefore, for a particular vehicle with a fixed space for hydrogen storage, the driving range using LH_2 is longer than for using CGH_2. For example, the General Motors Hydrogen3 Opel Zafira minivan is specified with a driving range of 400 km for 4.6 kg of liquid hydrogen, versus 270 km for a 700 bar tank (Satyapal et al. 2007). To improve the driving range, more space is needed, which will squeeze the passenger and cargo space, introducing extra weight and associated costs.

Efforts are underway to increase the pressure limit of the tank with the aim of enhancing the volumetric capacity. Currently carbon fibre is used in structural reinforcement for the composite vessel. The cost of the tanks is essentially dictated by the cost and amount of carbon fibre used (Satyapal et al. 2007). How to design and manufacture low carbon fibre tanks while meeting all the specification is a huge challenge. On the other hand, it seems that there is a trade-off point in the pressure limit. At high pressure, an increase in CGH_2 pressure produces less than a proportional increase in energy density, since producing and/or pumping high pressure hydrogen require more energy (Aceves et al. 2006). Advancement in compression technology is required to improve the efficiency. Safety is always an issue for storing hydrogen at high pressure. The potential is there for hydrogen leakage from a stationary vehicle to form an explosive mixture, which may cause severe damage (Utgikar and Thiesen 2005). How to prevent the potential explosion is another challenge.

2.4.3 Intermetallic compounds

Table 2.2 (Züttel 2004) gives the most important families of hydride-forming intermetallic compounds. The A element is usually a rare earth or an alkaline earth metal and tends to form a stable hydride. The B element is often a transition metal and forms only unstable hydrides. The different families of intermetallic compounds are classified on the basis of their crystal structures, such as AB_2 type (Laves phase), AB_5 type (Haucke phase), and Ti-based body centered cubic (BCC) (Sakintuna et al. 2007). Research on intermetallic compounds for hydrogen storage started more than 20 years ago. One of the most interesting features of the intermetallic hydrides is the very high volumetric density of the hydrogen atoms present in the host lattice. As can be seen

from Fig. 2.2, the hydrogen volume density of both $LaNi_5H_6$ and $TiFeH_2$ exceed the 2015 target. In addition, the properties of the intermetallic compounds can be tailored by modifying their compositions. This opens up many possibilities for improvements and applications. However, for practical applications at ambient temperature and pressure, their low energy per unit weight is an important disadvantage. For instance, the hydrogen capacity of $LaNi_5$, the most widely studied of these compounds, is only 1.5 wt. %, far below the 2015 target (Fig. 2.2).

Table 2.2 The most important families of hydride-forming intermetallic compounds (Züttel 2004).

Please see print copy for table 2.2

The thermodynamic aspect of the hydride formation from gaseous hydrogen is described by means of pressure-composition-temperature (PCT) plots (Fig. 2.5, Züttel 2004). When the solid solution (α-phase) and hydride phase (β-phase) coexist, the isotherms show a flat plateau, the length of which determines the amount of hydrogen stored. In the pure hydride phase, the hydrogen pressure rises steeply with the concentration. The two-phase region ends in a critical point T_c, above which the

transition from α-phase to β-phase is continuous. The equilibrium pressure (P_{H_2}) increases with increasing temperature according to the van't Hoff equation:

$$\ln P_{H_2} = \frac{\Delta H}{RT} - \frac{\Delta S}{R} \tag{2.1}$$

where R is the gas constant, T is the absolute temperature, and ΔS and ΔH are the entropy and enthalpy changes per mole H_2. In an equilibrium state, these thermodynamic data can be calculated from the van't Hoff plots on the right side in Fig. 2.5.

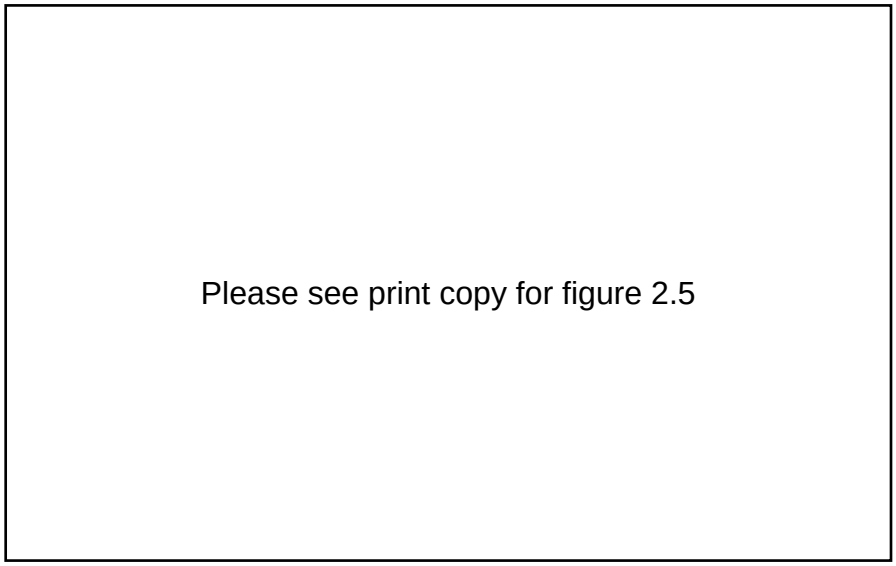

Fig. 2.5. Pressure-composition-temperature plots (left-hand side) for a hypothetical metal hydride. The corresponding van't Hoff plot is shown on the right-hand side (Züttel 2004).

The enthalpy of formation for a hydride can be calculated from the slope of the straight line by plotting $\ln P_{H_2}$ versus $1/T$. The entropy change for the hydride can be calculated from the intercept of the straight line ($1/T = 0$). ΔH can vary widely from alloy to alloy and is a measure of the strength of the metal hydrogen bonding (Züttel 2004). ΔS can also vary, but not as much as ΔH . The van't Hoff plot is a convenient way to describe

the pressure-temperature stability of metal hydrides. Fig. 2.6 shows van't Hoff plots of some real hydrides.

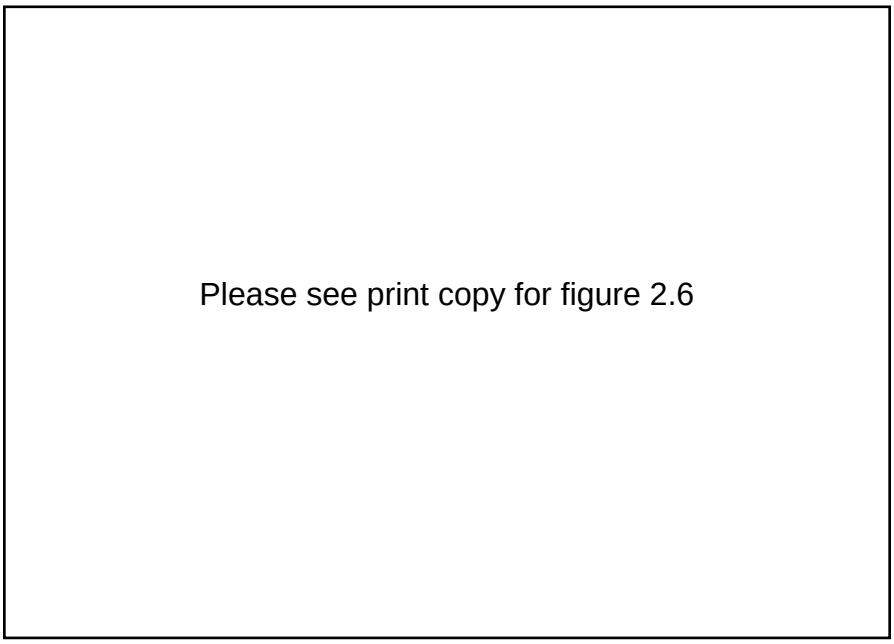

Fig. 2.6. Van't Hoff plots of some selected hydrides. The stabilization of the hydride of $LaNi_5$ by the partial substitution of nickel with aluminium in $LaNi_5$ is shown, as well as stabilization by the substitution of lanthanum with mischmetal (e.g. 51 % La, 33 % Ce, 12 % Nd, 4 % Pr) (Züttel 2004).

2.4.3.1 AB_5 type compounds

The prime example of an intermetallic hydride is lanthanum nickel hydride ($LaNi_5H_6$). This hydride was first investigated by Buschow and Miedema (1978) at Philips, and its use in rechargeable metal hydride batteries operated in KOH was subsequently demonstrated by Notten (1991). $LaNi_5$/H itself is not a practical system for a battery since the lattice tends to fragment after a few hydrogenation cycles, but a series of AB_5 compounds based on this system were developed. Batteries made from these compounds have largely replaced Ni-Cd rechargeable batteries.

Many investigations on the $LaNi_5$ based system have been devoted to the crystal structure and to the thermodynamic and electrochemical properties. So far, the multicomponent $La_{1-x}RE_xNi_{5-y}M_y$ system has been extensively studied (M = Mn, Cr, Fe, Co, Cu, Al, Sn, Ge, Si and RE = Mischmetal, Ce, Nb) (Corre et al. 1998, Lu et al. 2006, and Joubert et al. 1999). Both the thermodynamic and electrochemical properties were found to be strongly dependent on the nature and content of the substituting elements. The effects of mechanical milling and surface treatment have also been studied (Aoyagi et al. 1995, Wang et al. 1995, Suda et al. 2001). However, until now, except for the success in battery development, there has been little in the way of a breakthrough in the $LaNi_5$ based hydrogen storage materials. Since the hydrogen storage capacity is no higher than 1.5 wt. %, far below the updated 2010 DOE target of 4.5 wt. %, which is for the system mass density (Table 2.1), and the cost of the metal elements is relatively high, research on the $LaNi_5$ based hydrogen storage materials has been gradually decreased recently.

2.4.3.2 AB type compounds

In 1974, Reilly and Wiswall reported on the formation and properties of titanium iron hydride. Due to the inexpensive metal elements and the high hydrogen volume density, TiFe has since become a well known hydrogen storage compound with a total hydrogen storage capacity of around 1.9 wt. %. However, the activation process for TiFe is troublesome, due to the formation of a Ti oxide layer. Both high temperature and high pressure are required to achieve a reproducible absorption/desorption of the maximum amount of hydrogen in the compound (Reilly and Wiswall 1974 and Bououdina et al. 2006). The application of mechanical alloying under different atmospheres with the use

of catalytic elements, e.g. Pd, can dramatically enhance the activation process and the hydriding/dehydriding kinetics (Zaluski et al. 1996). Much like $LaNi_5$, the low hydrogen mass density of TiFe impedes its application. As a result, there have been very few reports on TiFe recently.

2.4.3.3 AB_2 type compounds

The AB_2 type compounds are derived from the Laves phase crystal structures. The potential AB_2 types are obtained with Ti and Zr on the A site. The B elements are represented mainly by different combination of 3d atoms, such as V, Cr, Mn, and Fe. Multicomponent Laves phase $Zr_{1-x}T_x(Mn, Cr)_{2-y}M_y$ (T = Ti, Y, Hf, Sc, Nb and M = V, Mo, Mn, Fe, Co, Al, Si, Ge) have been studied extensively as hydrogen storage materials, where both the thermodynamic and electrochemical properties have been found to be dependent on the nature and the content of the substitution (Bououdina et al. 1997 and 1998). Most of the AB_2 compounds show relatively higher capacities, faster kinetics, longer life, and a relatively lower cost in comparison with the $LaNi_5$ based systems (Bououdina et al. 2000). However, their hydrides are too stable at room temperature. In addition, the AB_2 type seems to be more sensitive to gaseous impurities than the AB_5 type compounds (Sakintuna et al. 2007).

2.4.3.4 BCC type compounds

New BCC solid solution alloys have been reported to absorb more hydrogen than the conventional intermetallic compounds. In recent years, Ti-based BCC phase alloys have attracted considerable attention due to their remarkable hydrogen storage capacities.

Ti–10Cr–18Mn–27V–5Fe and Ti–10Cr–18Mn–32V have hydrogen storage capacities of 3.01 and 3.36 wt. %, respectively (Yu et al. 2006). Increasing the V content is an effective way to accelerate hydrogen absorption, improve the hydrogen storage capacity, and flatten the hydrogen desorption plateau (Sakintuna et al. 2007). The maximum hydrogen storage capacity of Ti–V–Cr–Mn alloys is 3.99 wt. % (Yu et al. 2004). However, it is well known that vanadium is expensive. Therefore, the high cost is one of the critical drawbacks limiting their practical applications.

2.4.4 Magnesium hydride

There has been a considerable amount of research on magnesium hydride due to its high storage capacity of 7.7 wt. %, low cost, and abundance in nature (Imamura et al. 2005, Zaluski et al. 1997, and Zhu et al. 2006). However, there are several disadvantages impeding its real world application. The thermodynamic stability of MgH_2 results in a relatively high desorption enthalpy, which leads to an unfavorable desorption temperature of 300 ^{o}C at 1 bar H_2 (Grochala et al. 2004 and Imamura et al. 2005). This temperature is too high for on board applications (Bogdanovic et al. 1999). Another drawback is the high reactivity towards water and oxygen (Zaluska et al. 1999b and Barkhordarian et al. 2004)

Many investigations on MgH_2 have focused on improving the kinetics of hydrogen absorption and desorption, and reducing the operating temperature. These have been accomplished to some extent by modifying the surface, reducing grain size, and introducing catalysts.

2.4.4.1 Surface modification

The properties of the magnesium surface are very critical in terms of hydrogen molecule absorption, hydrogen molecule dissociation onto the surface, and hydrogen atom diffusion into the metal. There are several steps affecting hydrogen absorption. Initially, there are sufficient active sites on the Mg surface, and the dissociation step is the limiting step in the hydride formation process (Holtz 1996 and Friedlmeier and Groll 1997). As the reaction progresses, hydrogen diffuses into the bulk, and the magnesium hydride layer grows. Diffusion through the hydride layer then becomes the rate-determining step (Friedlmeier and Groll 1997). In addition to the hydride layer, a dense and stable MgO layer also inhibits the hydrogen absorption rate and slows down hydrogen diffusion (Zaluska et al. 1999b and Andreasen et al. 2005).

Ball milling can create a fresh surface through the collisions between powders and balls/walls. The newly formed surfaces contain no MgO, and this reduces the diffusion impedance and consequently facilitates the hydrogen diffusion. Along with the new surfaces, there are many defects and dislocations on the surface, which are believed to facilitate hydrogen absorption by accelerating nucleation (Song et al. 1985 and Vijay et al. 2005). At the same time, the specific surface area (SSA) also increases dramatically. It could be increased more than 10 fold after just one hour of ball milling (Hanada et al 2004). The increased SSA enlarges the surface contact between Mg and hydrogen, and ultimately contributes to hydrogen absorption (Shang et al. 2004, Wang et al. 1995, and Gross et al. 1998).

2.4.4.2 Nanocrystallization

Numerous experiments have proved that the hydrogen cycling properties of magnesium can be improved dramatically by obtaining nanocrystalline magnesium. Fig. 2.7 illustrates the absorption behavior of magnesium at 300 ^{o}C for samples with different grain sizes (Zaluska et al. 1999b). The samples were all prepared by ball milling to ensure similar surface properties in all the samples, and even the polycrystalline sample was milled – although for a very short period of time (5 min). The polycrystalline sample did not exhibit any significant hydrogen absorption at 300 ^{o}C, whereas the nanocrystalline samples absorbed hydrogen relatively quickly. Hout et al. (1999) reported that the activation energy for desorption was 120 MJ/mol for nanocrystalline MgH_2, compared with 156 MJ/mol for the un-milled coarser powders. The nanocrystalline MgH_2 released hydrogen completely after around 13 minutes at 350 ^{o}C, in contrast with less than a quarter released for the un-milled powders. From a quantum chemistry perspective, small MgH_2 clusters have a much lower desorption energy than bulk MgH_2, which enables hydrogen desorption to occur at lower temperature. An MgH_2 crystal size of 0.9 nm corresponds to a desorption temperature of only 200 ^{o}C (Wagemans et al. 2005).

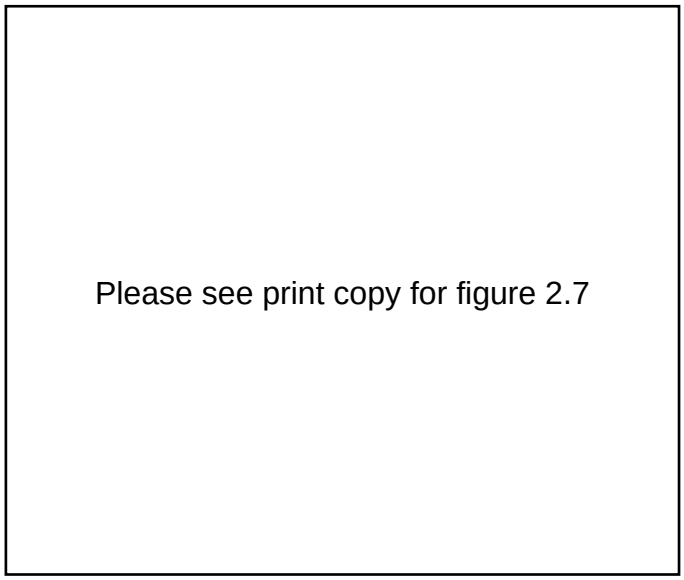

Fig. 2.7. Effect of grain size on hydrogen absorption of magnesium powders (Zaluska et al. 1999 [b]).

The improvements in hydrogen cycling kinetics by nanocrystallization are believed to be due to a combination of several reasons. Firstly, the reduction in grain size shortens the hydrogen diffusion distance, which consequently accelerates absorption and desorption. Secondly, nanoscale materials contain more grain boundaries than un-milled samples, and these boundaries facilitate hydrogen diffusion in the matrix (Huot et al. 2001 and Yavari et al. 2005). Thirdly, the nanocrystals obtained through ball milling have large amounts of defects, which provide more nucleation sites for the hydride phase (Song et al. 1985 and Vijay et al. 2005).

2.4.4.3 Effect of additives

Additives have been intensively studied in attempt to improve the sluggish hydrogen cycling kinetics and reduce the operating temperature. The additives investigated mainly fall into four groups: metal elements, metal oxides, alloys, and carbon.

2.4.4.3.1 Metal elements

Palladium is a good catalyst for the hydrogen dissociation reaction on the metal surface. By coating Pd on the magnesium surface, the hydriding properties were dramatically improved (Zaluska et al. 1999b). The catalytic effects of Pd can be maintained, since Pd oxide decomposes easily during hydrogen cycling (Zaluski et al. 1995). The high cost of Pd, however, inhibits its wide application. Nickel also shows catalytic effects on the hydrogen cycling properties of magnesium. Ni has a strong affinity to hydrogen, and this can facilitate the hydrogen dissociation and absorption onto a metal surface (Bloch and Mint 1997 and Baer et al. 1997). The introduction of 1 at. % Ni could lead to a reduction in the hydrogenation temperature of Mg from 275 ^{o}C to 175 ^{o}C and a lowering of the desorption temperature from 350 ^{o}C to 275 ^{o}C (Holtz and Imam 1999). Niobium was also found to act as a catalyst for hydrogen absorption and desorption. This is believed to be associated with the formation of a metastable niobium hydride phase, which acts as a gateway through which hydrogen released from MgH_2 can flow (Pelletier et al. 2001). It has been proposed that vanadium's catalytic effect was also due to the formation of a hydride, $VH_{0.81}$, which serves as a "hydrogen pump" (Huot et al. 2001).

2.4.4.3.2 Metal oxides

Many metal oxides have been used to improve the hydrogen cycling kinetics of magnesium. Although the mechanism remains unclear, the observed enhancement after the addition of oxides seems to be mainly due to two factors: milling effects and catalytic effects. Fe_2O_3 (Song et al. 2004) and WO_3 (Castro and Bobet 2004) were

found to enhance the hydrogen cycling properties of Mg. It was suggested that the brittle oxides and their pulverization during mechanical milling help the magnesium to become finer, which shortens the hydrogen diffusion distance. In addition, there were more defects and dislocations on the Mg surface after ball milling, which accelerated nucleation. Oelerich et al. (2001) agreed with this explanation, but they also proposed that the valence states of metals in the oxides played an important role with respect to the hydrogen cycling kinetics. Transition metal oxides, such as Cr_2O_3, V_2O_5, and Fe_3O_4, exhibited remarkable catalytic effects on the hydrogen cycling, while Al_2O_3, SiO_2, and Sc_2O_3, in which the metal atoms appear with only a single valence state, caused little change. Barkhordarian et al. (2003) studied a series of metal oxides and found that Nb_2O_5 was the best in terms of catalysis towards hydrogen absorption/desorption (Fig. 2.8). They attributed this to the oxide state of Nb. However, it was also proposed (Hanada et al. 2005) that it was the reduction to metallic Nb that actually facilitated the hydrogen cycling.

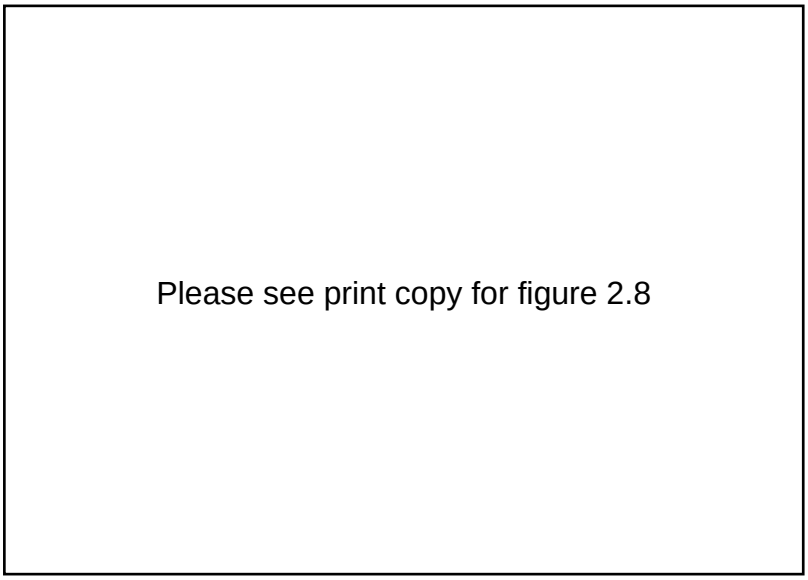

Fig. 2.8. Comparison of the desorption rates of MgH_2 with different metal oxide catalyst additions (Barkhordarian et al. 2003).

2.4.4.3.3 Alloys

Some low operating temperature metal hydrides, for example, $LaNi_5$ (Liang et al. 2000 and Sun et al. 2000) and TiFe (Wang et al. 2002), have been tried in an attempt to improve the cycling properties of Mg. The impetus behind these attempts is presumably to try to generate a synergetic reaction between the high operating temperature MgH_2 and the low operating temperature hydrides. Sun et al. (2002) reported that composites of Mg-$LaNi_5$ were more easily activated than pure magnesium. Wang et al. (2002) found that magnesium with amorphous $TiFe_{1.2}$ exhibited rapid absorption and a low operating temperature, as well as superior oxidation resistance. These properties were attributed to the combined effects of amorphous $TiFe_{1.2}$ and the nanostructure of Mg. However, although there were some improvements, synergetic reactions between the hydrides were not found. Zaluska et al. (1999a) observed synergy between MgH_2 and Mg_2NiH_4 after ball milling. The mixture operated at temperatures of 220 ^oC-240 ^oC, with excellent cycling kinetics and with a total hydrogen capacity exceeding 5 wt. %.

2.4.4.3.4 Carbon

Graphite and CNTs have been investigated as catalysts to improve the hydrogen cycling properties of magnesium. Imamura et al. (1999 and 2003) found that once the graphite was amorphized after ball milling, there was no improvement in the hydriding kinetics. After organic additives such as benzene, tetrahydrofuran, and cyclohexane were introduced during ball milling, magnesium showed remarkable hydriding (Fig. 2.9, Imamura et al. 2000) and dehydriding properties (Fig. 2.10, Imamura et al. 2000). This was attributed to the fact that graphite broke along cleavage planes under the protection

of organic additives, rather than becoming amorphous. The cleavage along the graphite layers promoted charge-transfer from magnesium to carbon, as evidenced by XPS studies, and this type of charge-transfer site is known to be usually active towards the catalytic activation of hydrogen molecules. However, Shang et al. (2004) found that the presence of crystalline graphite had little influence on desorption, but only led to a rapid absorption. Montone et al. (2006) later reported that the addition of benzene helped preserve the structural integrity of graphite and induce finer Mg particles, and that these two together contributed to the rehydrogenation.

Wu et al. (2006) compared the catalytic effects of graphite and SWCNTs, and found that Mg-SWCNT composite showed better hydrogen storage performance than Mg-graphite, which was attributed to the special nanostructure of the SWCNTs. The catalytic effects of graphite nanofibre (GNF) and graphite were compared by Lukashev et al. (2006). It turned out that MgH_2-GNF composite and MgH_2-graphite exhibited almost the same hydriding kinetics under the same conditions, although GNF and graphite are different in structure.

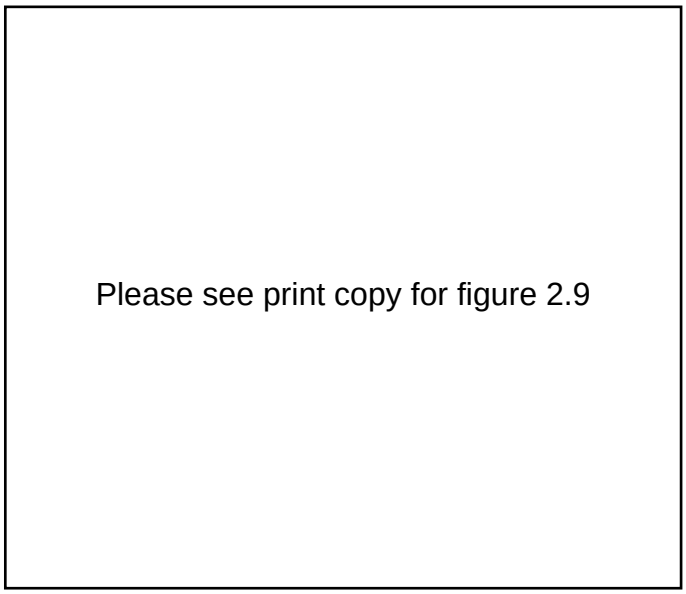

Fig. 2.9. Hydriding behavior of various Mg/G composites. $(Mg/G)_{none}$ was prepared without organic additives; the rest were prepared as follows: with cyclohexadiene, i.e. $(Mg/G)_{DIENE}$; with cyclohexene, i.e. $(Mg/G)_{ENE}$; with tetrahydrofuran, i.e. $(Mg/G)_{THF}$; with cyclohexane, i.e. $(Mg/G)_{CH}$; and with benzene, i.e. $(Mg/G)_{BN}$. Hydrogen absorption conditions: H_2 = 66.7 kPa; 453 K (Imamura et al. 2000).

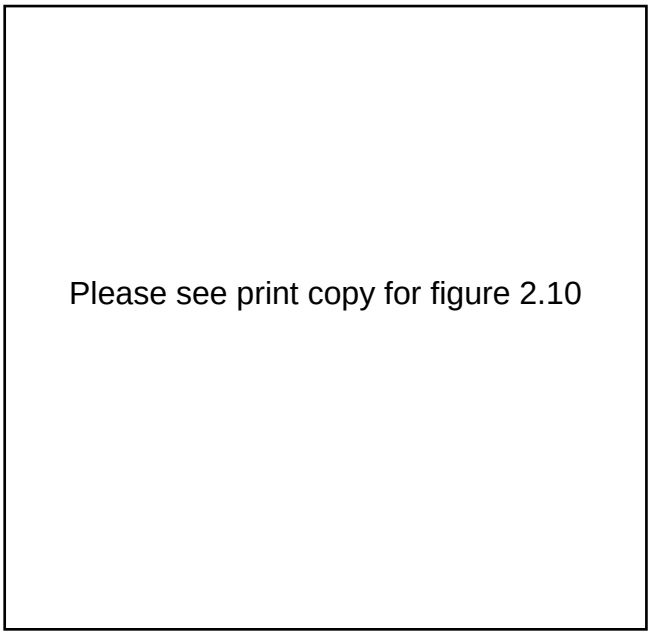

Fig. 2.10. DSC measurements of various Mg/G composites. $(Mg/G)_{none}$ was prepared without organic additives; the rest were prepared with cyclohexadiene, i.e. $(Mg/G)_{DIENE}$ or with cyclohexene, i.e. $(Mg/G)_{ENE}$ (Imamura et al. 2000).

2.4.4.3.5 Other additives

More recently, transition metal fluorides such as FeF_3 (Yavari et al. 2005) and NbF_3 (Luo et al. 2007) have been tried, and significant improvements in the hydrogen cycling performance of Mg have been reported. The explanation for the improvement was that the fluorine transfer reaction generated protective MgF_3 plus Fe catalyst in form of nanoparticles.

Luo (2004) suggested that $LiNH_2$-MgH_2 is likely to be a viable hydrogen storage system since it was found that the lithium amide-hydride system could be significantly destabilized by partially replacing Li by Mg, and this new system could absorb 4.5 wt. % hydrogen or possibly more at 200 ^oC.

MgH_2-$LiBH_4$ composite has been studied recently, and interesting results have been published. The desorption of the composite takes place in two steps:

$$MgH_2 + 2LiBH_4 \rightarrow Mg + 2LiBH_4 + H_2 \quad (2.2)$$

$$Mg + 2LiBH_4 + H_2 \rightarrow MgB_2 + 2LiH + 4H_2 \quad (2.3)$$

In the first step, desorption of MgH_2 takes place and Mg is formed. Thereafter, $LiBH_4$ decomposes and LiH and MgB_2 are formed. As for the absorption, MgB_2 and LiH composite can start absorbing hydrogen at 250 ^oC and 50 bar hydrogen (Bosenberg et al. 2007), while in the case of pure $LiBH_4$, 600 ^oC and 350 bar hydrogen is required for rehydrogenation (Orimo et al. 2005).

2.4.4.4 Cycling properties

The cycling properties of Mg/MgH_2 depend on the starting microstructure, the cycling temperature, the nature of the catalysts, and the purity of the hydrogen gas. Mischmetals were observed to maintain the cyclic stability at high temperature (420-440 ^oC) (Tran et al. 2003). Dehouche et al. (2002) studied the cycling properties of MgH_2–Cr_2O_3 composite at 300 ^oC up to 1000 cycles. An 8 % increase in the hydrogen storage capacity was found, which was attributed to the structural relaxation and crystallite growth. While the absorption remained the same, the desorption kinetics slowed down dramatically, which was believed to be a result of microstructural coarsening. Dehouche et al. (2000) also found that MgH_2 with 5 at. % V exhibited good decrepitation resistance upon cycling at 300 ^oC. The slight deterioration in desorption after 2000 cycles is related to crystal growth during cycling. Friedlmeier et al. (1995) observed that after 4300 cycles, a partial sintering occurred for a sample that contained Mg with 2 wt. % Ni, which led to a reduction in SSA and, in turn, to a reduction in adsorption kinetics.

Depending on the technology and hydrogen source used, different impurities can be present to different degrees. These impurities can affect the performance of the storage system over its lifetime. The effects of O_2, N_2, CO, and CO_2 on the hydrogen cycling properties of Mg have been investigated by Pedersen et al. (1993). O_2 reacted with Mg, but still allowed the formation of hydride at a reduced rate; N_2 slowed down the absorption speed; CO_2 prevented hydrogen uptake. Moisture was found to have an adverse effect on the desorption kinetics (Dehouche et al. 2003). In the presence of 100 ppm moisture, the desorption properties of the MgH_2-V-Ti system deteriorated after 1000 cycles, which was due to the surface modification.

2.4.5 Magnesium-nickel alloys

There has been a considerable amount of research on the hydrogen storage properties of the Mg-Ni system due to the high hydrogen storage capacities by weight and the low cost. In this system, nickel has the role of either making up the alloy, as in Mg_2Ni, or acting as catalyst, such as with Ni added to Mg_2Ni. Through ball milling and substitution, a variety of nanocrystalline and amorphous, stoichiometric and non-stoichiometric Mg-Ni based alloys have been obtained, and interesting results have been published.

2.4.5.1 Gas-solid reactions

There are two compounds that exist in the Mg-Ni phase diagram: Mg_2Ni and $MgNi_2$. The latter does not react with hydrogen at pressures up to 540 atm. in the temperature range of -196 ^oC to 300 ^oC (Liu 2004). Mg_2Ni reacts with hydrogen to form the ternary hydride Mg_2NiH_4. The hydrogen content in the hydride is 3.6 wt. %, which is higher than for most of the intermetallic hydrides. Therefore Mg_2Ni has attracted a tremendous amount of attention as a hydrogen storage material. However, the absorption and desorption require temperatures above 300 ^oC, and the hydriding/dehydriding kinetics is slow at temperatures lower than 250 ^oC (Janot et al. 2004).

Similarly to the case of magnesium hydride, nanocrystallization is an effective way to improve the hydriding/dehydriding properties of Mg_2Ni. It was found that nanocrystalline Mg_2Ni obtained through ball milling displayed a noticeable hydriding/dehydriding reaction at 200 ^oC (Nam and Lee 2002). This improvement is due to the small grain size and large amounts of defects in the alloys.

Substitution is another widely used method to improve the hydrogen cycling properties. Both Mg and Ni have been partially substituted in numerous experiments. The partial replacement of Ni in Mg_2Ni by 3d elements alters the dissociation temperature dramatically. For example, the dissociation temperature in 1 atm. pressure for the Cu-containing alloys drops from 250 ^oC to 227 ^oC. However, the absorption and desorption rate for the Cu-containing alloys are close to those of Mg_2Ni (Darnaudery et al. 1983). Yang et al. (2002) have successfully synthesized $Mg_2Ni_{0.75}M_{0.25}$ (M = Ti, Cr, Mn, Ni, Cu, and Zn) alloys by the ball-milling diffusion method. Results show that the alloys have the best performance after treatment: the hydrogen desorption capacity reaches the highest value after only two hydrogen cycling cycles. Partially replacing Ni by Zr has also led to better hydriding/dehydriding kinetics (Zhang et al. 1998). Au et al. (1995) found that the alloying elements such as Ni, Cu, and Re had positive effects on the kinetics of the Mg-based alloys. Compounds composed of Mg, Ni, and Cu, namely $Mg_2(Cu,Ni)$, played a key role in improving the kinetics of the Mg-based alloys.

Nanocrystalline and amorphous MgNi based non-stoichiometric alloys were developed during the research, mainly through ball milling. Song et al. (1999) investigated the hydriding and dehydriding properties of mechanically milled Mg with x wt. % Ni (x = 5, 10, 25, 55). The mixtures show much larger hydrogen storage capacities and much faster hydrogen cycling kinetics than other Mg-based alloys. Tanaka et al. (1999) studied the hydrogen absorption rates and pressure-composition isotherms (PCT) of nanocrystalline MgNi and MgNi-RE (RE = La, Nd) alloys prepared by the melt spinning and crystallization method. These nanocrystallized alloys, particularly those from the MgNi-RE system, exhibit excellent hydrogen absorption kinetics and PCT characteristics in comparison with the corresponding as-cast alloys with a coarse

eutectic structure. Orimo et al. (1997) investigated the hydrogenation properties of amorphous MgNi alloys prepared by ball milling under a hydrogen atmosphere, and it was found that the desorption occurred at the much lower temperature of 160 ^{o}C. Terashita et al. (1999) studied amorphous $Mg_2Ni_{1.9}M_{0.1}$ (M = Ca, Cu) and found that elemental substitutions in amorphous MgNi alloys could effectively change the hydrogen cycling properties.

2.4.5.2 Electrochemical performance

Theoretically, Mg_2Ni has a high discharge capacity of 999 $mAhg^{-1}$. Thus, an electrochemical approach has been used to investigate the hydriding and dehydriding properties of Mg_2Ni electrode. However, the coarser grained Mg_2Ni alloys have extremely low discharge capacities of only 15 or 18 $mAhg^{-1}$ at a discharge current density of 50 mAg^{-1} (Liu 2004). In addition, the cycling performance of the Mg_2Ni electrode is very poor, since the electrode surface is easily corroded to $Mg(OH)_2$ in alkaline solutions after several cycles (Ma et al. 2004). Several methods have been tried in attempts to improve the discharge capacity and cycling performance.

Microencapsulation of Mg_2Ni alloys by metal and alloy coatings can improve the electrode performance. Luo and Cui (1998) increased the discharge capacity of $Mg_{1.9}Al_{0.1}Ni_{0.9}Y_{0.1}$ alloy to about 175, 200, and 230 $mAhg^{-1}$ at a current density of 10 mAg^{-1} by microencapsulation with Ni-B, Ni-P, and Ni-Pd-P, respectively. Kohno and Kanda (1997) reported that by ball milling Mg_2Ni with Ni powder, a discharge capacity of 750 $mAhg^{-1}$ (Mg_2Ni) was obtained at a discharge current density of 20 mAg^{-1}. A

higher discharge capacity of 780 $mAhg^{-1}$ was achieved at a higher discharge current density of 50 mAg^{-1} for Ni-coated $Mg_2Ni_{0.9}Mn_{0.1}$ electrodes (Chen et al. 1998).

Zhang et al. (1999) reported that the cycling performance of $MgNi_x$ alloys could be significantly enhanced by increasing the x value. Partial substitution of Mg with Ti and V can also improve the cycling performance of the MgNi alloy electrode (Iwakura et al. 2001). Surface modification by graphite was found effective in suppressing the formation of $Mg(OH)_2$, and as a result, improving the cycling performance (Iwakura et al. 2002). However, the capacity decay of the Mg_2Ni based alloy electrode is still serious. After 50 cycles, the discharge capacity of electrode coated by Ni and graphite was only 45 % and 76 % of the maximum capacity, respectively (Han et al. 2002). The short cycle life makes it inadequate for practical use as an electrode material.

2.4.6 Complex hydride

The complex hydrides are of interest because of the high number of hydrogen atoms per metal atom, and as a result, the very high hydrogen storage capacity, with the highest value of 18.4 wt. % (Table 2.3, Züttel et al. 2003). The hydrogen storage capacities exceed the latest DOE 2010 target, and some of them, such as $LiBH_4$, $NaBH_4$, and $LiAlH_4$, are even well above the 2015 target (Fig. 2.2). The main difference of the complex hydrides from the above-mentioned metallic hydrides is the transition to an ionic or covalent compound of the metals upon hydrogen absorption (Züttel 2004). The hydrogen in the complex hydrides is often located in the corners of a tetrahedron with boron or aluminum in the centre. The negative charge of the anion, $[BH_4]^-$ and $[AlH_4]^-$ is compensated by a cation, e.g. Li or Na. The tetrahydroborates $M(BH_4)$ and the

tetrahydroaluminate $M(AlH_4)$ (M = Li, Na) are interesting storage materials; however, they are very stable and decompose only at elevated temperatures, and sometimes above the melting point of the complex.

Table 2.3 Physical properties of selected complex hydrides (Züttel et al. 2003).

Please see print copy for table 2.3

2.4.6.1 $NaAlH_4$

Although $NaAlH_4$ contains 7.4 wt. % hydrogen and its cost is low, it was never considered as a rechargeable hydrogen carrier due to the irreversibility and poor kinetics. This situation was changed by Bogdanovic and Schwickardi (1997), whose pioneering studies demonstrated that upon doping with selected titanium compounds, the dehydriding of anionic aluminum hydrides could be enhanced and rendered reversible under moderate conditions in the solid state. Their report has triggered extensive research on the hydrogen storage performance of $NaAlH_4$. Since then, several types of catalysts have been investigated, such as liquid alkoxides $Ti(OBu^n)_4$ and $Zr(OPr^i)_4$

(Gross et al. 2002), $TiCl_3$ (Sandrock et al. 2002), TiN (Bogdanovic et al. 2003), $ZrCl_3$ (Anton 2003), and TiF_3 (Anton 2003).

$NaAlH_4$ releases hydrogen through two steps:

$$3NaAlH_4 \rightarrow Na_3AlH_6 + 2Al + 3H_2 \quad (2.4)$$

$$Na_3AlH_6 \rightarrow 3NaH + Al + 3/2H_2 \quad (2.5)$$

These two steps result in 3.7 wt. % and 1.9 wt. % hydrogen release, respectively, totaling 5.6 wt. %. Since the decomposition of NaH occurs at the very high temperature of 425 ^oC, for a practical storage system only these two steps are considered. However, the maximum theoretical value of 5.6 wt. % is below the 2010 system target of 6 wt. %. The hydrogen desorption kinetics are too slow for vehicular application. In addition, the packing density of the powder is low (roughly 50 % of the theoretical crystal density), making the system's volumetric capacity a challenge (Satyapal et al. 2007).

2.4.6.2 $LiAlH_4$

In theory, $LiAlH_4$ is very attractive for hydrogen storage, because of its high hydrogen content of 10.5 wt. %. The desorption of $LiAlH_4$ occurs in two steps:

$$3LiAlH_4 \rightarrow Li_3AlH_6 + 2Al + 3H_2 \quad (2.6)$$

$$Li_3AlH_6 \rightarrow 3LiH + Al + 3H_2 \quad (2.7)$$

The hydrogen released in the two reactions corresponds to 5.3 wt. % from the decomposition of $LiAlH_4$ and 2.65 wt. % from the decomposition of Li_3AlH_6 at temperatures between 160 ^oC and 200 ^oC. After completion of the reactions, 2.65 wt. % of the total hydrogen content in $LiAlH_4$ remains unreleased in form of LiH, which can be desorbed only at very high temperatures above 680 ^oC (Zaluski et al. 1999). There

are several drawbacks hindering the commercialization of $LiAlH_4$: 1) it can not be rehydrogenated (Kojima et al. 2007); 2) it has an extremely high hydrogen equilibrium pressure, even at room temperature (Sakintuna et al. 2006); and 3) it has very slow kinetics.

2.4.6.3 $NaBH_4$

$NaBH_4$ has been the most studied to date as a hydrogen carrier, with the hydrogen released via hydrolysis reactions:

$$NaBH_4 + 2H_2O \rightarrow NaBO_2 + 4H_2 \quad (2.8)$$

The exothermic reaction can be controlled in an aqueous medium via pH and the use of a catalyst. A $NaBH_4$-based system has been reported to possess a system gravimetric capacity of about 4 wt. % (Satyapal et al. 2007). While the hydrogen storage capacity is high and the release kinetics is fast, current boron hydride production from borate requires multi-step conditions, and regeneration is difficult to conduct on-board. In addition, the heat released during the reaction, 75 kJ per mole H_2, is not used directly for propulsion, so that the efficiency of the process is inevitably somewhat limited in energy terms. Thus, while being very attractive for small portable devices, this process still seems somewhat impractical for vehicle propulsion systems (Ross 2006). The key to a successful implementation of this system is centered around a more energy efficient regeneration process converting borate to boron-hydride.

2.4.6.4 $LiBH_4$

$LiBH_4$ has a gravimetric hydrogen density of 18.4 wt. %. The compound was first synthesized by Schlesinger and Brown (1940) in an organic solvent. $LiBH_4$ can desorb three of the four hydrogens in the compound when heated to above its melting temperature of 368 ^oC. The desorption process can be catalysed by adding SiO_2, and significant thermal desorption was observed, starting at 200 ^oC (Züttel et al. 2003). It has been shown (Orimo et al. 2005) that the rehydriding process can proceed to completion under 35 MPa at 600 ^oC. Vajo et al. (2005) found that $LiBH_4$ could reversibly store 8–10 wt. % hydrogen at temperatures of 315-400 ^oC by addition of MgH_2. Formation of MgB_2 destabilizes the $LiBH_4$. However, the kinetics is too slow, with the absorption time up to 6000 min, which hinders practical applications. A scientific understanding of the mechanism of the thermal desorption from $LiBH_4$ and the rehydrogenation remains a challenge, and more work needs to be carried out.

2.4.7 High specific surface area (SSA) materials

Hydrogen molecules can be physically absorbed on the surface of a solid via van de Waals forces. Materials with high SSA, such as activated carbon and zeolites, have been investigated for hydrogen storage. However, these materials are ineffective in storing hydrogen at RT, which is due to the weak interaction between hydrogen and the absorbent. Their relatively high storage capacity is observed only at cryogenic temperatures, where interaction through physisorption is much stronger.

The advent of new materials, such as carbon nanotubes (CNTs), graphite nanofibres (GNFs), and metal organic frameworks (MOFs), have triggered intensive investigations on their hydrogen storage performance. The interest in these materials mainly arises from their particular structures and very high SSA. There is a large amount of variation

in the structural parameters of the CNTs and GNFs. As for the MOFs, a great variety of organic ligands and metal ions can form many types of MOFs. This large variety may result in varying hydrogen storage performance.

2.4.7.1 Carbon nanotubes (CNTs)

CNTs consist of graphene sheets rolled up into a cylindrical shape with a diameter on the nanometer scale. Both ends are usually sealed by hemispherical fullerenes when synthesized (Fig. 2.11, Dresselhaus 1997). A single wall nanotube (SWCNT) is formed by only one graphene sheet, while a multiwall nanotube (MWCNT) is formed by multiple concentric graphene sheets. The diameter, length of the tubes, and number of walls are dependent on the synthesis method. The potential fields from the walls of the mircropores overlap, leading to stronger gas-solid interaction than would occur for absorption on a flat carbon surface. This bestows CNTs with a unique capacity to store hydrogen (Züttel et al. 2004).

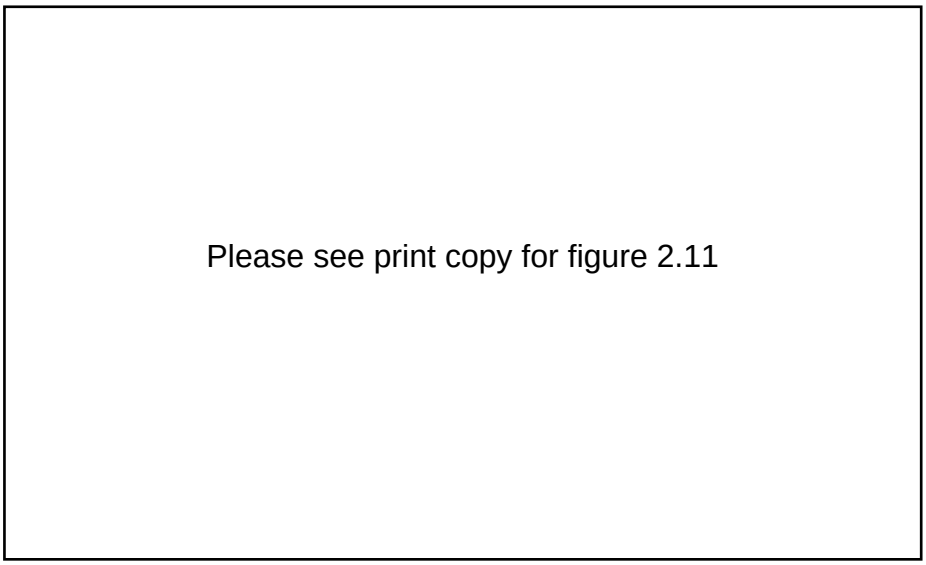

Fig. 2.11. Stable forms of carbon clusters: (a) a piece of a graphene sheet, (b) the fullerene C_{60}, and (c) a model for a carbon nanotube (Dresselhaus 1997).

Since the first experimental result was published by Dillon et al. in 1997 on the hydrogen storage properties of SWCNTs, there has been very intensive research, both theoretical and experimental, on the mechanism of hydrogen storage and how to improve the storage capacity. However, there exist large discrepancies in the claimed hydrogen storage capacities. Liu et al. (1999) revealed a hydrogen uptake of 4.2 wt. % at RT and 100 bar by SWCNTs with a large mean diameter of 1.85 nm. Ye et al. (1999) reported that more than 8 wt. % hydrogen was stored by pure SWCNTs at 120 bar and around 77 K. Poirier et al. (2004) found that a value of 4 wt. % was reached at 1 bar and 77 K; on the contrary, only 0.2 wt. % was attained at RT at 1 bar. In 2004, a DOE sponsored external panel reviewing the hydrogen storage capacity of SWCNTs came to the conclusion that there was essentially no hydrogen stored on/in pure SWCNTs at RT, while metal doped SWCNTs were found to take up 2-3 wt. % at RT (National Renewable Energy Laboratory 2004).

With regard to MWCNTs, different results have also been published. Hou et al. (2003) showed that the storage capacity of MWCNTs was proportional to their diameters, and the highest value of 4.6 wt. % was observed at 293 K and 13.5 MPa. Li et al. (2001) reported that the hydrogen storage capacity of MWCNTs depended on the structure, ranging from 1.29 to 3.98 wt. % at RT. Lueking and Yang (2002) investigated the effect of the catalyst used for synthesizing MWCNTs on the hydrogen storage capacity and found that, at atmospheric pressure, removal of the catalyst decreased the uptake from 0.6 wt. % to below detection limits. Hydrogen uptake of MWCNTs with metal oxide as catalyst ranged from 0.25 wt. % to 0.98 wt. %, depending on surface area.

Despite these discrepancies, most of the research so far has demonstrated that the hydrogen storage capacity of CNTs is less than 1 wt. % at ambient temperature and about 10 MPa (Züttel et al. 2002, Zhou et al. 2004, Furuya et al. 2004, and Panella et al. 2005), but it can reach 4.5-8 wt. % when the temperature is reduced to 77 K (Ye et al. 1999, Züttel et el. 2002, and Panella et al. 2005).

The mechanism of hydrogen storage by CNTs is still not clear. It appears that at elevated temperature hydrogen can become covalently bonded to carbon, with hydrocarbons detected in the desorption spectrum (Langmi et al. 2007). However, the many low hydrogen uptake values at RT suggest that there is little chemisorption occurring at RT. At cryogenic temperatures physisorption appears to be the interaction between hydrogen and the absorbent. The physisorption results in a large amount of hydrogen being absorbed at this temperature.

Hirscher and Panella (2005) found that the hydrogen storage capacities of various types of nanostructured carbon, including purified and unpurified SWCNTs, amorphous nanotubes, activated carbon, porous carbon with uniform pore dimensions, and mixtures of MWCNTs and SWCNTs, have an almost linear relationship with the SSA (Fig. 2.12). The material with the highest SSA shows the highest hydrogen storage capacity. This observation was corroborated by Züttel et al. (2002), who found that the storage capacity is a function of the surface and temperature. Furthermore, inelastic neutron scattering measurements indicated that the structure of carbon nanomaterials, e.g. the curvature of graphene sheets and long-range order, have little influence on the hydrogen storage capacity (Schimmel et al. 2003 and 2004).

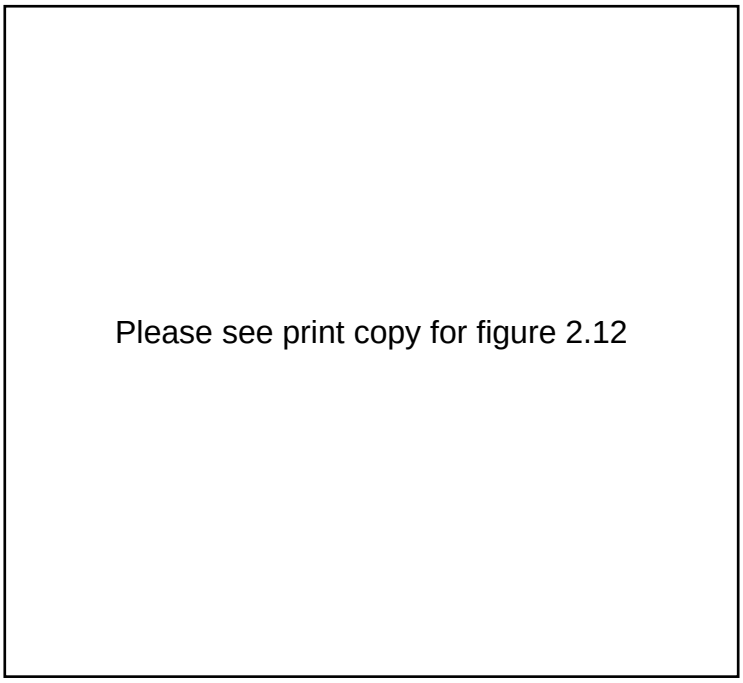

Fig. 2.12. Hydrogen storage capacity of various carbon nanostructures versus SSA at RT and at 77 K. The slopes of the curves are 0.23 × 10−3 at RT and 1.91 × 10−3 at 77 K (Hirscher and Panella 2005).

So far, CNTs exhibit a high storage capacity only at cryogenic temperatures, at which hydrogen and the absorbent interact through physisorption. It has been demonstrated that the amount of hydrogen absorbed by the absorbent is proportional to the SSA of CNTs (Hirscher and Panella 2005). Therefore, how to engineer the structure of CNTs with the aim of increasing the SSA should be the focal point of future research.

2.4.7.2 Graphite nanofibers (GNFs)

The impetus behind the research on hydrogen storage by GNFs is their special conformation. The structural features (Fig. 2.13) were depicted by Chambers et al. (1998). X-ray diffraction analysis coupled with electron diffraction indicated that prior to adsorption experiments the spacing between platelets for nanofibers that were

suitable for hydrogen storage was 3.37 Å, which is interesting, considering that the kinetic diameter of hydrogen is only 2.89 Å.

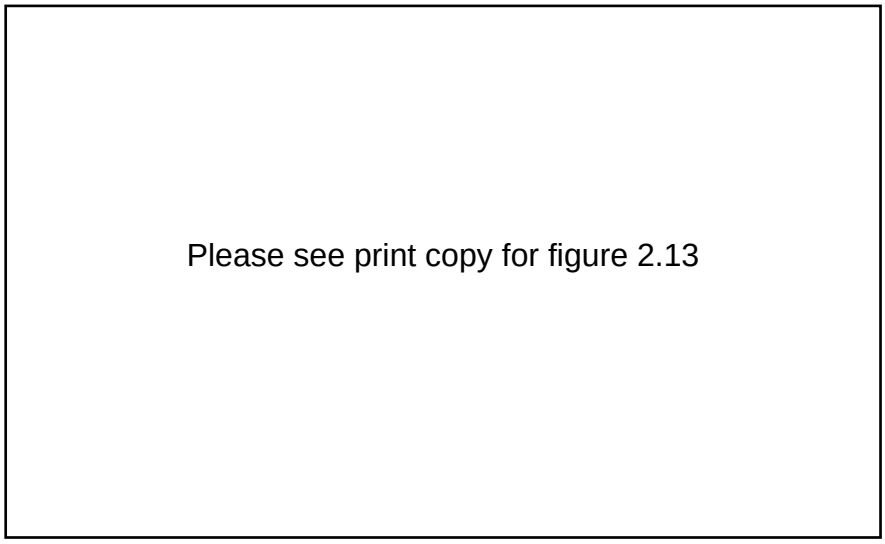

Fig. 2.13. Schematic representation of the arrangement of platelets in a graphite nanofiber; (b) an enlarged section showing the detail of area marked in (a) (Chambers et al. 1998).

In a similar way to CNTs, there are scattered results on the hydrogen storage capacities of GNFs. Chambers et al. (1998) reported an extraordinarily high hydrogen storage capacity, 67 wt. % at about 112 bar and at RT. However, this result has not been corroborated to date. Ahn et al. (1998) studied various GNFs and found that the storage was generally below 0.08 wt. %. Ströbel et al. (1999) attempted to reproduce the ambitious claims of Chambers, however, a maximum of only 1.5 wt. % was achieved for GNFs at 125 bar and at RT. Ritschel et al. (2002) reported an even lower value, around 0.04 wt. % at RT and 45 bar. Most of the research results so far have shown that at RT, GNFs store tiny amounts of hydrogen. Their storage capacity is even lower than for some types of activated carbon (Wu et al. 2007), which has a very high SSA.

2.4.7.3 Metal organic frameworks (MOFs)

The term “metal organic frameworks” (MOFs) refers to a new class of crystalline materials composed of metal ions linked together by organic ligands. The great advantage of MOFs over other high SSA materials is that there exist a great variety of organic ligands and metal ions that can be used to synthesize MOFs. This offers many opportunities for the design and tailoring of the properties of MOFs. Recently, a BET of 4000 m^2/g, more than four times the SSA of zeolite, was obtained for MOF-77 (Wong-Foy et al. 2006) and MOF-101 (Ferey et al. 2005). The high SSA and tailorable pore dimensions of MOFs have triggered intensive research on their prospects for hydrogen storage.

In 2003, the first investigations of hydrogen storage in MOFs were reported for MOF-5 (Rosi et al.). The results revealed that MOFs could store more hydrogen than any other crystalline microporous material at 77 K. At such a low temperature, hydrogen molecules are absorbed on the MOF surface by van de Waals forces (Rowsell et al. 2004). The hydrogen storage capacity of MOF-5 of 4.5–5.2 wt. % at 50 bar and 77 K has been corroborated in different laboratories (Wong-Foy et al. 2006 and Panella et al. 2006). This value is more than two times higher than for the best zeolites (Langmi et al. 2005) and comparable to that of the best carbonaceous material, i.e. high-grade activated carbon AX-21 (Chahine and Bose 1994 and Panella et al. 2005). However, there was also a lower value of less than 2 wt. % reported (Panella et al. 2005), which was due to the lower SSA resulting from a different synthesis and activation process. In 2006, hydrogen uptakes up to 7 wt. % at 77 K have been reported for MOFs with a BET SSA of 3000–4700 m^2/g (Wong-Foy et al. 2006 and Lin et al. 2006). This

extraordinarily large storage capacity is the highest so far for physisiorption on porous materials.

There are two factors that influence the hydrogen storage capacity of MOFs, the pore dimensions and the SSA. Small pore size can enhance the interaction between hydrogen and the absorbent, allowing a steep increase in the hydrogen storage at low pressures (Frost et al. 2006). At higher pressures the amount of hydrogen absorbed is correlated with the SSA. The maximum hydrogen uptake at 77 K correlates almost linearly with the SSA. This correlation is independent of the framework structure and the central metal ions (Hirscher and Panella 2007). However, the pore dimensions and SSA typically counteract each other, i.e. materials with very small pores often possess a reduced SSA. One Mg-based MOF with pores only 3.5 Å in diameter (Dinca and Long 2005) had a SSA of less than 200 m^2/g, and as a result, it stores only 0.5 wt. % of hydrogen at 77 K.

MOFs display excellent storage capacity only at cryogenic temperatures to date. At RT, both experiments (Panella et al. 2006 and Xin et al. 2006) and simulations (Garberoglio et al. 2005) show that the storage capacity is less than 1 wt. % at pressures up to 100 bar, even for MOFs possessing a high SSA or strong adsorption sites. Therefore the application of MOFs for H_2 storage will be limited to the very low temperature range.

Although research on MOFs as hydrogen storage materials started only recently, there have been some very appealing results. Moreover, the results are reproducible. Considering the variety of MOFs, considerable work can be done in the future. The focus should be on finding materials possessing an optimum combination of small pores and high SSA.

2.5 Factors affecting hydrogen storage properties

All the above mentioned materials naturally display their own hydrogen storage capacity, absorption and desorption temperatures, and kinetics, which are correlated with the material's structure and the nature of the interaction between hydrogen and the host material. However, for most of the materials, the absorption and desorption temperatures and the kinetics can be altered through modifying the structure and surface properties, and by introducing catalysts. For some materials, such as high SSA materials, the hydrogen storage capacities can also be altered. Also, the grain size, defects, and fabrication procedure affect the hydrogen storage properties.

2.5.1 Nature of interaction

Hydrides exist as ionic, polymeric covalent, volatile covalent, and metallic hydrides. The demarcation between the various types of hydrides is not sharp; they merge into each other according to the electronegativities of the elements concerned (Züttel 2004). The interaction between hydrogen and the host material predominantly determines the hydrogen storage capacity, absorption/desorption temperature, and kinetics. As summarized above, Mg, $LaNi_5$, $NaBH_4$, CNTs, and MOFs display different hydrogen storage properties, mainly due to the respective interactions between hydrogen and the hosts. However, the bonding can be changed from one type to another to a certain degree, and the bond strength can be modified more or less by substitution, doping, and ball milling. As a result, the hydrogen storage properties can be tailored (DOE report 2004).

2.5.2 Grain size

Figure 2.7 illustrates the effect of grain size on the hydrogen absorption behavior of magnesium. Clearly, nanocrystalline Mg displays remarkable absorption kinetics, in contrast with the negligible absorption by coarser grained Mg powder. Similar enhancements in hydrogen absorption have been reported in many nanostructured hydrides, such as TiFe (Zaluski et al. 1996), $LaNi_5$ (Zaluski et al. 1995), and $NaAlH_4$ (Anton 2003).

Nanocrystalline metals have properties markedly different from their conventional crystalline counterparts. Nanostructured materials are defined as having a grain size not exceeding 100 nm, with the range between 5 and 50 nm being more typical (Zaluska et al. 2001). Such a small grain size facilitates hydrogen diffusion, which consequently accelerates the absorption and desorption. In addition, nanoscale materials contain more grain boundaries than coarser grained samples, and these boundaries facilitate hydrogen diffusion in the matrix (Huot et al. 2001 and Yavari et al. 2005). Finally, nanocrystals obtained through ball milling are characterized by large amounts of defects, which provide more nucleation sites for the hydride phase (Song et al. 1985 and Vijay et al. 2005).

2.5.3 Specific surface area

The specific surface area (SSA) of the material powders is another key factor determining the kinetics of hydrogen storage capacities, in particular for hydrogen storage through physisorption. It has been found that the hydrogen storage capacity of various types of nanostructured carbon has an almost linear relationship with the SSA

(Fig. 2.12, Hirscher and Panella 2005). This means that the hydrogen storage capacities of certain materials can be improved by just increasing the SSA. As for hydrogen storage through chemisorption, i.e. the formation of ionic, covalent, and metallic bonding, the SSA also plays a significant role. An increase in SSA provides more sites allowing hydrogen molecules to approach the surface, which consequently improves the dissociation rate of hydrogen molecules on the surface. As a result, the formation of all kinds of bonding is accelerated.

2.5.4 Defects

Nanocrystalline materials contain a larger fraction of atoms located in defect cores with distorted coordination, for example, in large angle grain boundaries and at dislocation lines (Gleiter 2000). The parameters of interaction of such atoms with hydrogen should be different from those of the atoms in the perfect bulk (Skripnyuk et al. 2004). It has been established experimentally that these defects are favorable to hydrogen absorption/desorption (Huot et al. 1999 and Pelletier et al. 2001). The defects on the surface act as hydrogen pick-up centers that allow faster hydrogen entrance, diffusion, and hydride nucleation (Song 1995 and Vijay et al. 2005). Defects in the interior of the bulk can dramatically facilitate the hydrogen diffusion (Zaluska et al. 2001).

2.6 Hydrogen storage material fabrication

Figure 2.14 (Varin and Czujko 2002) illustrates the most common ways that have been applied to synthesize nanostructured activated intermetallic hydrides. Conventionally, arc/induction melting of elemental powders and subsequent homogenization annealing

of bulk ingots have been used to fabricate polycrystalline intermetallics. Recently, non-equilibrium processing techniques, such as mechanical alloying (MA), mechanical milling (MM), and reactive mechanical alloying/milling (RMA/RMM), have been widely used to synthesize/manufacture hydrogen storage media.

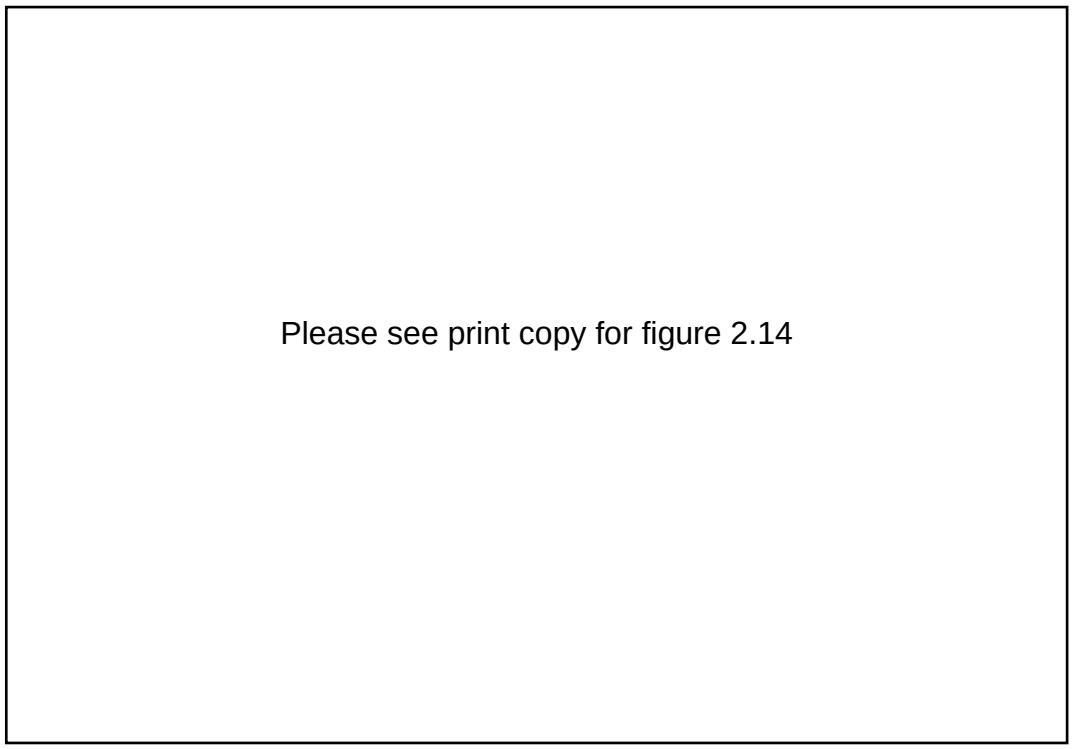

Fig. 2.14. Flow chart showing the possible routes for the manufacture of nanostructured activated intermetallics and their composites and hydrides (Varin and Czujko 2002).

Figure 2.15 illustrates the effects of ball milling on the hydrogen absorption (a) and desorption (b) properties of magnesium. The kinetics appeared to be significantly improved after ball milling, which could mainly be attributed to the reduced crystallite size, increased SSA, and the presence of defects induced by ball milling (Huot et al. 2001).

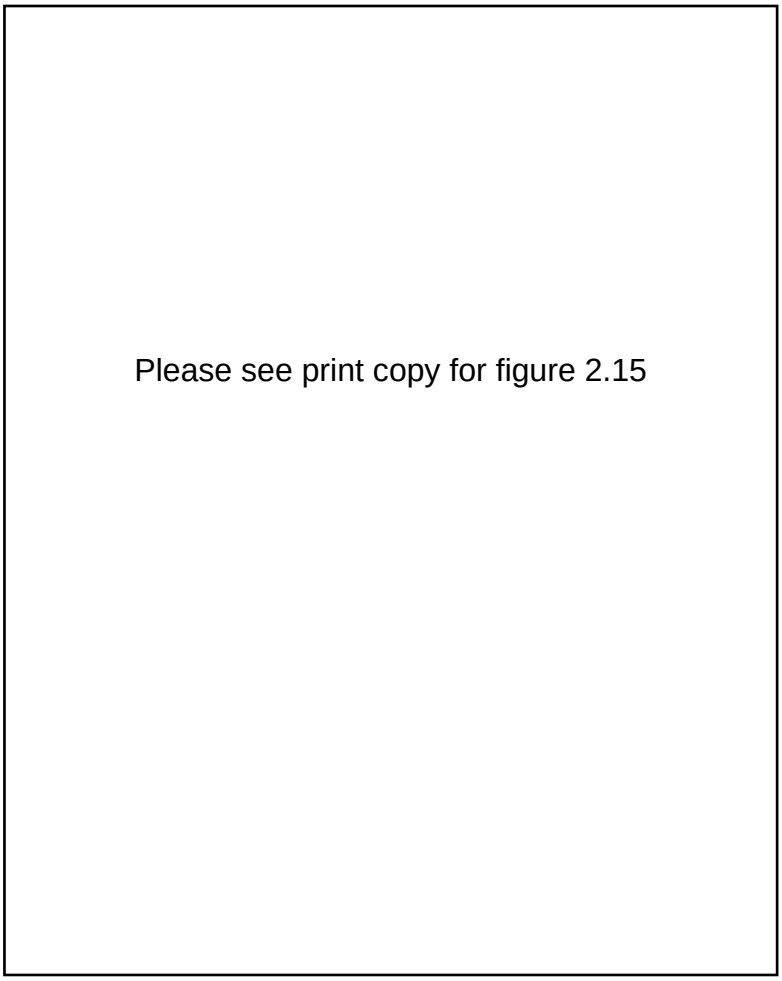

Fig. 2.15. Hydrogen absorption (a) and desorption (b) curves of un-milled MgH_2 (filled symbols) and milled MgH_2 (open symbols) (Huot et al. 2001).

2.6.1 Ball milling

As discussed above, mechanical alloying (MA), mechanical milling (MM), and reactive mechanical alloying/milling (RMA/RMM) have now become very important ways to synthesize hydrogen storage materials. No matter what name is used, it is all about the effect exerted by the moving balls on the powder in the cylinder. Starting with elemental powders, ball milling can lead to the formation of a variety of materials, such as crystalline and amorphous alloys, and stoichiometric and non-stoichiometric alloys. It can also help to increase the SSA of the particles, introduce more defects into the grains, and add in catalysts. Depending on the design and goal of the experiment, some

or all of the above aspects can be realized through a single ball milling. For example, ball milling Mg with a small amount of Ni can result in a product composed of nanocrystalline and high SSA magnesium powders, as well as uniformly dispersed nickel catalyst.

2.6.2 Ball milling modes

It is well known that the final microstructure of the milled products depends on a variety of parameters, such as the nature of the milling machine, the materials of the balls and bowl, the speed, the ball to powder weight ratio, the duration, the atmosphere, the process control agents, etc. (Huot et al. 2001). Some of these variables, such as the ball to powder weight ratio and speed, are related to the milling energy applied on the powders in the cylinder. The milling energy is also related to the nature of the milling machine. The Spex 8000 is designed as a high-energy mill, while the Fritsch is a mill with adjustable energy output, from low energy to high energy. These two mills are commonly used to synthesize hydrogen storage materials. The movement of the grinding balls in both mills is very chaotic, which generates strong impacts and irregular, weak shearing. As a result, there is a large spectrum of local milling energies, which adversely affects the structural uniformity in the milled products.

The Uni-Ball-Mill 5 is a ball mill that allows the control of the milling energy by adjusting the movements of the grinding balls (Calka and Radlinski 1991). It is convenient to realize both low-energy shearing (Fig. 2.16) and high-energy impact (Fig. 2.17) in experimental practice. In the shearing mode, the balls both rotate and oscillate around an equilibrium position at the bottom of the milling cylinder (Fig. 2.16). In the

impact mode, the ball movement during the milling process is confined to the vertical plane by the cylinder walls and is controlled by an external magnetic field (Fig. 2.17). In both cases, the magnetic field is provided by FeNdB magnets. The intensity and direction of the magnetic field can be externally adjusted, allowing the ball trajectories and milling energy to be varied in a controlled manner.

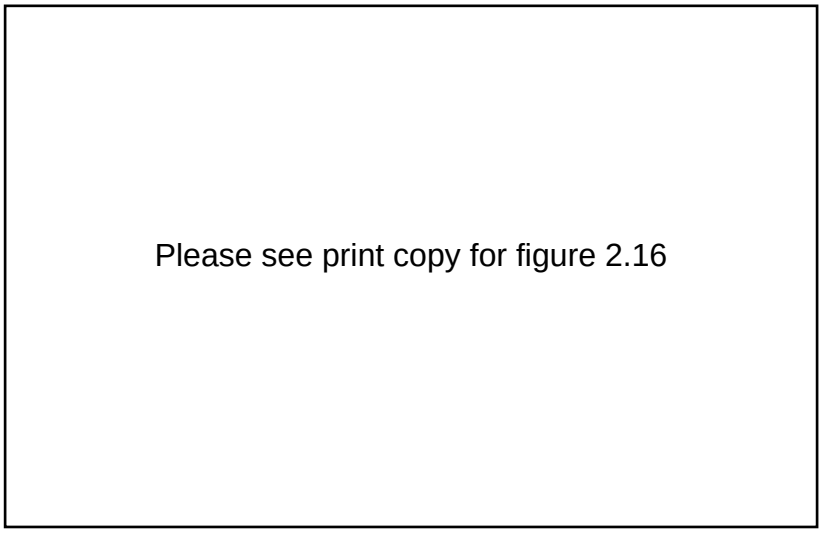

Fig. 2.16. The Uni-Ball-Mill 5 with the FeNdB external magnets operating in the shearing mode (Calka and Radlinski 1991).

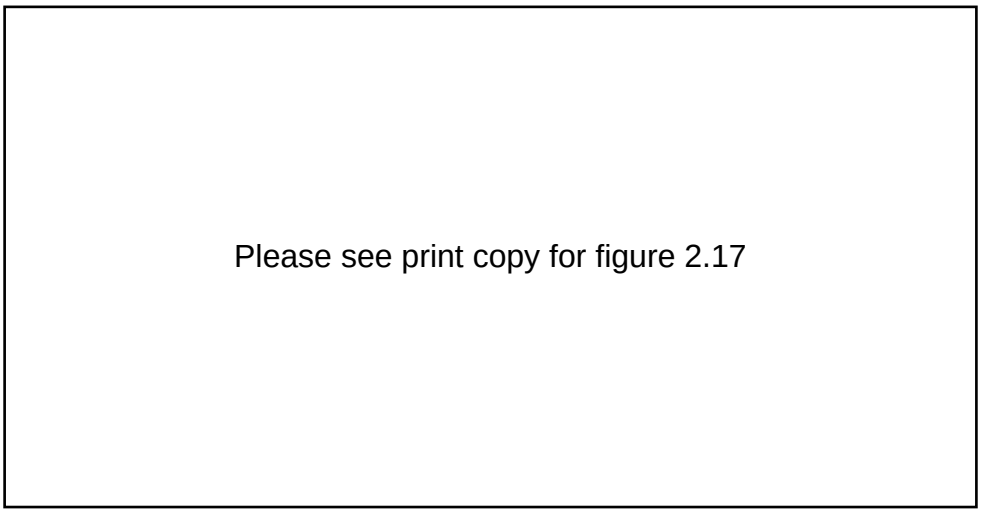

Fig. 2.17. The Uni-Ball-Mill 5 with the FeNdB external magnets operating in the impact mode (Calka and Radlinski 1991).

Chapter 3

Experimental details

3.1 Materials

All the metals and chemicals used are listed in Table 3.1. Relevant information is provided as well.

Table 3.1 Description of metals, chemicals, and gases.

Name	Molecular formula	Purity	Particle size
Magnesium	Mg	≥99 %	44 μm
Copper	Cu	99.7 %	3 μm
Nickel	Ni	99.8 %	<1 μm
Graphite	C	99.95 %	<45 μm
Boron	B	99 %	<3 μm
Iron(III) oxide	Fe_2O_3	≥99%	<5 μm
Iron(II,III) oxide	Fe_3O_4	98%	<5 μm
Carbon nanotubes (multiwalled)	C	>95%	outer diameter 20-30 nm, length 0.5 μm
Carbon black	C	99 %	1-2 μm
Hydrogen	H_2	>99.5%, gas	n/a
Helium	He	>99.99 %, gas	n/a

3.2 Materials synthesis

3.2.1 Spex 8000

This high energy mechanical mill was employed to synthesize $Mg_{1.9}Cu_{0.1}Ni_x$ (x = 1.8, 1.9, 2.0, and 2.1) alloys. The starting elemental metals were first weighed out according to the alloy ratio and put into a stainless steel jar, then the jar was sealed with a rubber O ring and filled with high purity argon in a glove box before operation. The ball-to-powder weight ratio was 10:1. Because of the severe cold welding during ball milling, especially for high energy milling, after each 99 minutes the jar was cleaned, and any bulk materials were crushed into powder using a mortar, ensuring that all three elements were fully mixed together and the composition was uniform. The whole duration of the milling was 10 h.

3.2.2 Uni-Ball-Mill 5

Graphite was milled under hydrogen using this mill under low-energy shearing (Fig. 2.16) and high-energy impact (Fig. 2.17) conditions, respectively. The milling cylinder was purged several times, using helium at first, and then filled up with hydrogen gas up to 500 kPa pressure. The duration of milling was 100 hours. For comparison, graphite powder was milled in helium under the same conditions. The same experimental methods were applied to mill boron in hydrogen and helium, respectively.

MgH_2 + Fe_2O_3 and MgH_2 + Fe_3O_4 composites were obtained using the low-energy shearing mode. The atomic ratio of Mg to Fe was 20:1. The ball-to-powder weight ratio was about 44:1, and the rotational speed was 60 rpm. After purging the cylinder with helium four times, high purity hydrogen was introduced to a final pressure of 600 kPa. After 24 hours of milling, the cylinder was refilled with hydrogen to the same pressure. The powder was milled for up to 48 hours.

Composites of MgH_2 + CB (carbon black), MgH_2 + G (graphite), and MgH_2 + MWCNT (multiwalled carbon nanotubes) were also synthesized through the low-energy shearing mode. The weight ratio of carbon allotropes to magnesium was 1:20. The experimental conditions were the same as those applied for obtaining MgH_2 + Fe_2O_3 and MgH_2 + Fe_3O_4 composites.

3.3 Physical analysis

3.3.1 Structure

X-ray diffraction (XRD) patterns were obtained using a Philips PW 1730 generator and diffractometer with Cu Kα radiation (λ = 0.15418 nm). The microstructure of the powders was investigated by Transmission Electron Microscopy (TEM) using a JEOL EM 2011 analytical instrument. TEM samples were prepared by dispersing powders onto holey carbon support films. A Labram HR 800 Raman spectrometer from Jobin Yvon was used with a 15 mW laser operating at a wavelength of 632.82 nm to investigate the structural changes of carbon allotropes before and after ball milling. The infrared (IR) absorbance was recorded using a Nicolet Avatar 360 FTIR spectrometer with an OMNI-sampler installed.

3.3.2 Morphology

The morphology was characterized using a Scanning Electron Microscope (SEM), a JEOL JSM 6460A analytical instrument, equipped with Energy Dispersive X-ray Spectrometry (EDS). EDS mapping allows visualization of the distribution of the elements.

3.3.3 Crystallite size

One way to obtain crystallite size is through calculations based on X-ray diffraction. The starting powders were used as reference samples to obtain the instrumental-broadening-corrected line profile width of each reflection 2θ, calculated from the parabolic approximation correction (Klug and Alexander 1974) given in Eq. (3.1)

$$\delta(2\theta) = \sqrt{B^2 - b^2} \tag{3.1}$$

where B and b are the widths of the same Bragg peak (in radians) for the experimental and reference powders, respectively. They were calculated by the software package TRACES^{TM} v.6.5.1 as the full-widths at half-maximum (FWHM) after automatic background removal. Separation of crystallite size and strain was obtained from a Williamson–Hall plot (Williamson and Hall 1953) as given in Eq. (3.2)

$$\delta(2\theta)\cos\theta = \frac{k\lambda}{L} + 4e\sin\theta \tag{3.2}$$

where θ is the Bragg angle of the analyzed peak, k a constant (≈1), λ the incident X-ray wavelength, L the crystallite size obtained from the intercept, and e the strain from the slope. The other method used to estimate the crystallite size was through observation of the TEM preliminary dark-field images.

3.3.4 Particle size

Three means were applied to measure the particle size. A rough estimate was obtained via observation of SEM images of MgH_2 + Fe_2O_3 and MgH_2 + Fe_3O_4 composites. The mean particle size of magnesium hydride and carbon allotrope composites was obtained using a Zetasizer Nano ZS (ZEN 3500, Malvern) with highly dry dispersion media. This method can give a reliable and accurate size analysis for nanoparticles. The particle

sizes of $Mg_{1.9}Cu_{0.1}Ni_x$ (x = 1.8, 1.9, 2.0, and 2.1) alloys and the size distribution were determined by a Mastersizer Laser Particle Size Analyzer (Malvern), which is suitable for measuring the particle size and size distribution of these alloy particles.

3.4 Electrochemical characterization

3.4.1 Preparation

$Mg_{1.9}Cu_{0.1}Ni_x$ (x = 1.8, 1.9, 2.0, and 2.1) alloy powder was mixed with nickel powder according to a mass ratio of 1:2. The mixture was first made into a slurry with the addition of 5 wt. % PVA solution, then the slurry was pasted onto nickel foam, which acted as the current collector for the negative electrode. After heat-treating at 100 ^oC under vacuum for 2 hours, the electrode was pressed at 900 kg cm^{-2}. Then the electrode was wrapped with a non-woven fabric separator. A $NiOOH/Ni(OH)_2$ electrode was selected as the counter electrode and 6 M KOH as the electrolyte.

3.4.2 Test

The charge and discharge properties of the alloy electrodes were measured with a DC-5 battery tester controlled by a computer at room temperature. The electrode was charged at 100 mAg^{-1} for 10 h and discharged at 20 mAg^{-1} with a cut-off voltage of 0.900 V. Linear polarization, cyclic voltammetry (CV), and a.c. impedance measurements were performed using a CHI660B electrochemical workstation. A three electrode system was used with Hg/HgO as the reference electrode and $NiOOH/Ni(OH)_2$ as the counter electrode. The apparent surface area of the electrode was 1 cm^2.

3.5 Hydrogen storage properties

3.5.1 Hydrogenation and heat treatment

In order to minimize experimental error, hydrogenation and heat treatment of the $Mg_{1.9}Cu_{0.1}Ni_x$ (x = 1.8, 1.9, 2.0, and 2.1) alloys were carried out in the same heating chamber at the same time, with each sample (100 mg) put into a small crucible. For obtaining the crystalline alloys, the as-prepared powders were annealed in argon at 600 ºC for 2 hours. For hydrogenation, the as-prepared powders were heated at 200 ºC, 250 ºC, and 300 ºC in 5 atm. hydrogen for 20 minutes.

3.5.2 Absorption and desorption

A volumetric Sieverts apparatus (Fig. 3.1) was used to test the hydrogen absorption and desorption kinetics. After half a gram of sample was put into the reactor, the system was evacuated and refilled with argon (valves 1 and 3) three times before heating. Hydrogen was introduced (valve 2) to a predetermined pressure. The absorption properties were investigated at 300 ^{o}C under 2 MPa, and desorption properties at 350 ^{o}C under 0.05 MPa. The residual gas was pumped out after the experiment (valve 4).

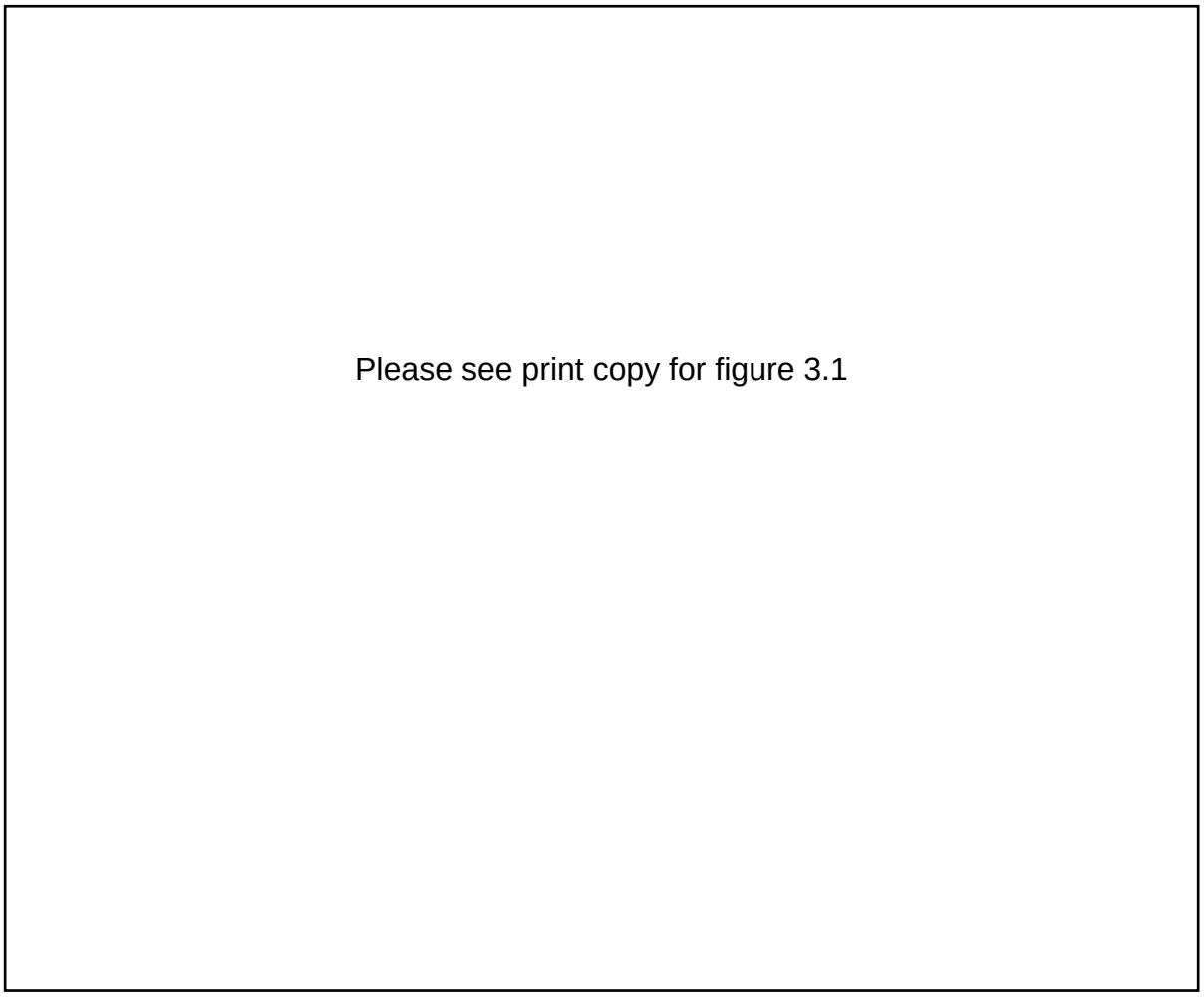

Fig. 3.1. Schematic of the volumetric Sieverts apparatus.

3.5.3 Differential scanning analysis

For boron and graphite, a differential scanning calorimeter (Perkin-Elmer DSC-4) was used with an argon flow rate of 70 ml/min at a heating rate of 20 ºC /min up to 500 ºC. For all other samples, a DSC Q100 (TA Instruments) was used at a heating rate of 6 ºC/min from room temperature to 500 ºC under an argon flow rate of 50 ml/min. These two types of DSC were used in order to maintain the consistency of the experimental results.

3.5.4 Hydrogen content

To determine the hydrogen content absorbed by boron and graphite during ball milling, carbon-hydrogen-nitrogen (CHN) analysis was carried out using a Carlo Erba Elemental Analyser Model 1106. This technique was applied since it gives reliable and accurate measurements for small amounts of sample. Thermogravimetry (TG, SETARAM) was used at a heating rate of 10 ºC /min with an argon flow rate of 50 ml/min to determine the amount of hydrogen stored by all the other samples.

3.5.5 Composition

The composition of graphite milled in hydrogen was investigated through a linear mode of time-of-flight mass spectrometry (LTOF MS) (Bajuk et al. 2001). For the measurements, a sample of the graphite powder (5 mg) was mixed with methanol (10 µL), placed on a flat stainless-steel sample holder, and then dried in air at room temperature, giving a visible and apparently homogenous spot with a diameter of about 5 mm. The ion acceleration voltage was 17 kV. All spectra were registered as an average of 64 laser shots.

Chapter 4

Thermal stability and hydrogen storage properties of $Mg_{1.9}Cu_{0.1}Ni_x$ (x = 1.8, 1.9, 2.0, and 2.1) alloys

4.1 Introduction

Mg-Ni alloys have attracted attention due to their low cost and high hydrogen storage capacity (3.6 wt. % for Mg_2Ni). Unfortunately, the high desorption temperature and sluggish absorption kinetics still render these alloys unsuitable for real world applications. Many efforts have been made to overcome these problems (Au 2005, Orimo et al. 2001, Janot et al. 2004, Yu et al. 2002, Liang et al. 1998, Ruggeri et al. 2002a, and Inoue et al. 2004). Basically, there are two approaches, i.e. changing the composition of alloys through substitution for Mg and/or Ni and synthesizing nanocrystalline and/or amorphous materials through ball milling.

Mechanically produced nanoscale hydrogen storage alloys possess different thermodynamics and kinetics from those of the conventional crystalline or amorphous ones (Au 2005 and Orimo et al. 1998). In nanocrystalline materials, there are more grain boundaries, which provide suitable paths to facilitate the hydrogen diffusion and consequently favour the absorption/desorption kinetics (Orimo et al. 2001 and Janot et al. 2004). A nanostructural material produced by ball milling can be regarded as a nanostructural composite, consisting of nano-grains, highly reactive grain boundaries, and disordered or amorphous regions. There is substantial evidence suggesting that the

hydriding properties of nanocrystalline materials are predominantly affected by the disordered regions at the interfaces of nano-grains, which comprise a huge volume fraction of the material (Zhu et al. 1987, Lu et al. 1994, and Orimo et al. 1997). However, the volume fractions of both nano-grains and disordered regions in the composite change during hydrogen cycling. This is because the amorphous regions will crystallize, while the nano-grains will recrystallize and grow during repeated heat treatment. As a result, the alloys will lose their initial notable hydriding properties.

The crystallization of an amorphous alloy is diffusion controlled, and the energy of activation is proportional to the enthalpy of formation of a hole having the size of the smaller type of atom (Buschow et al. 1980 and Buschow 1981). In the Mg-Ni system, nickel has a smaller atomic size and larger enthalpy of formation of a monovacancy, therefore, the thermal stability of the materials, i.e. the volume fractions of nano-grains, grain boundaries, and amorphous regions, is believed to be strongly affected by the content of nickel in the alloys. As a result, the nickel content should influence the hydrogen cycling properties of the Mg-Ni system, since the hydrogen cycling properties are dependent on the structure.

Nickel is well known as an effective catalyst for hydriding and dehydriding (Orimo et al. 1998, Ruggeri et al. 2002a, and Inoue et al. 2004), and copper also leads to some improvement in hydrogen cycling (Yu et al. 2002 and Liang et al. 1998), therefore, in this study, $Mg_{1.9}Cu_{0.1}Ni_x$ (x = 1.8, 1.9, 2.0, and 2.1) alloys were prepared using a Spex high-energy ball mill. The thermal stability of the as-prepared alloys and the corresponding hydrogen storage properties were examined in relation to the nickel content.

4.2 Morphology and particle size

Figure 4.1 shows an SEM image of the as-prepared $Mg_{1.9}Cu_{0.1}Ni_{1.9}$ alloy and the Mg, Ni, Cu, and O distributions in the alloy. All the other alloy powders with different Ni content have similar morphology to this, so they are not shown here. The characteristics of the products obtained through mechanical alloying are displayed in the image. Ball milling constantly creates new surfaces as a result of repeated cold-welding and fracturing. The fragments created are cold welded together by impacts, with irregular particles formed. From the Energy Dispersive x-ray Spectroscopy (EDS) mapping, all the elements are homogenously distributed, including the oxygen impurities, which were introduced from the raw materials and/or leaking of the milling jar. This means that the high-energy ball milling is an effective way to obtain alloys with uniform composition. The particle size varies from several microns to several tens of microns, as observed from the Mastersizer Laser Particle Size Analyzer, and more than fifty percent of the particles are about 5 microns in size, which is regarded as the mean particle size.

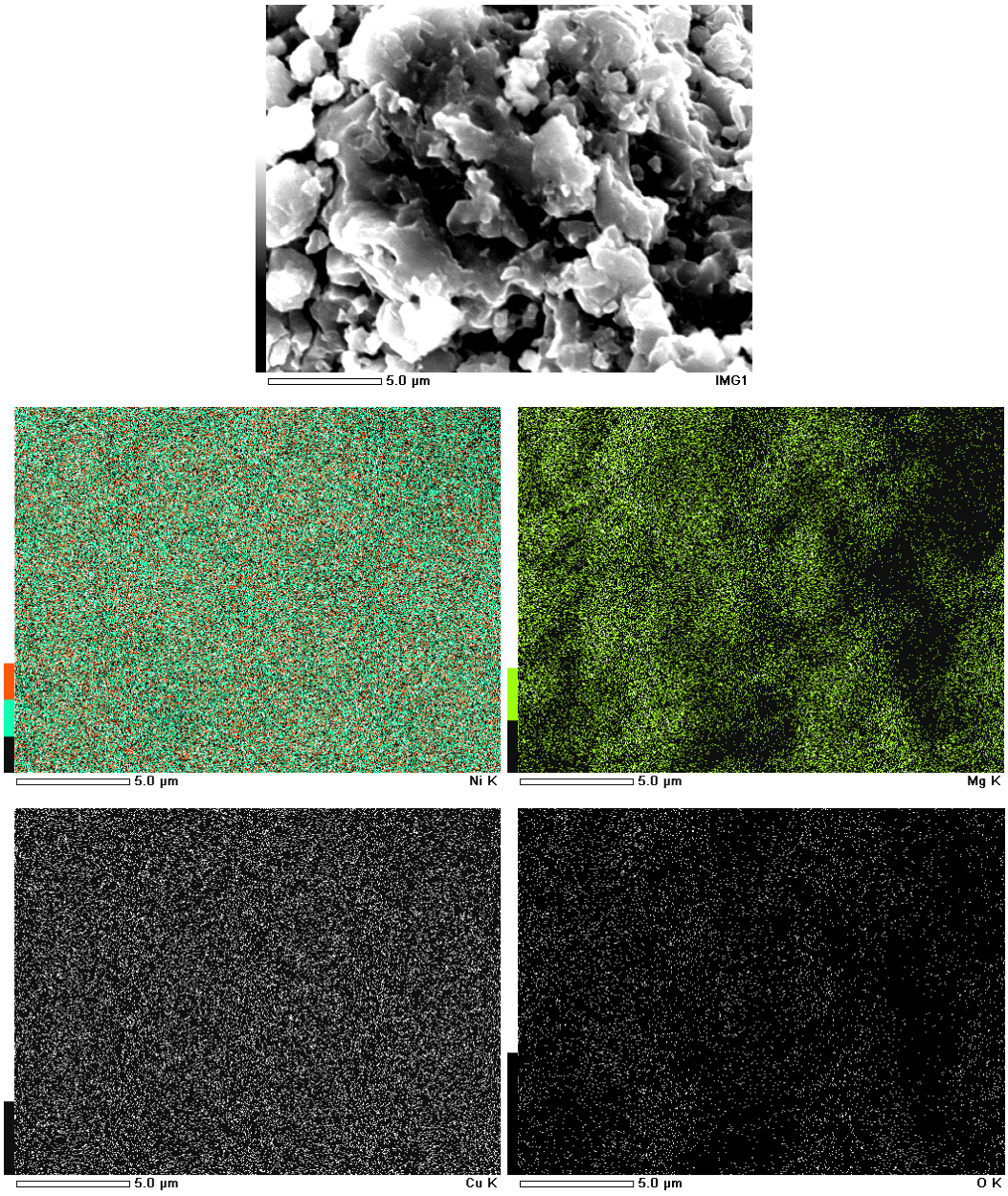

Fig. 4.1. SEM image of the as-prepared $Mg_{1.9}Cu_{0.1}Ni_{1.9}$ alloy and Mg, Ni, Cu, and O distributions in the alloy.

4.3 Structure

4.3.1 X-ray diffraction

Figure 4.2 shows the X-ray diffraction patterns of the as-prepared alloys produced through high-energy ball milling. The broad peaks obtained from the as-prepared alloys indicate that an amorphous or mixed amorphous/nanostructural product had been formed. There are no peaks related to Cu and Ni, implying that copper and nickel atoms were dissolved in the alloys without any significant changes to the structure.

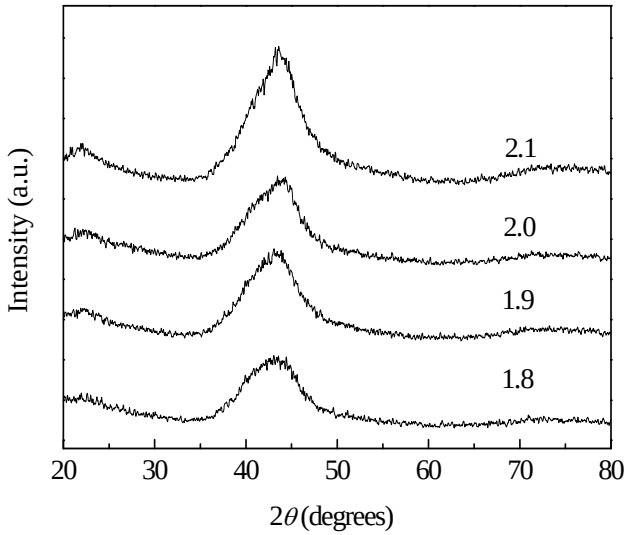

Fig. 4.2. X-ray diffraction patterns of the as-prepared $Mg_{1.9}Cu_{0.1}Ni_x$ (x = 1.8, 1.9, 2.0, and 2.1) alloys.

4.3.2 TEM analysis

Preliminary transmission electron microscopy (TEM) investigations, using TEM bright field imaging combined with selected area electron diffraction (SAED), indicated that much of the as-prepared product was in fact amorphous. However, the milling product was unstable, and it partially transformed to a mixed amorphous/nanocrystalline product under the heat of the electron beam. The SAED pattern (Fig. 4.3(b)) shows a typical predominantly diffuse ring pattern obtained from the region of the as-prepared sample

shown in the bright field image, Fig. 4.3(a), while Fig. 4.3(c) shows a typical diffraction pattern obtained from a region that had been heated in the electron microscope by the electron beam and was subsequently transformed to a mixed amorphous/ultra-fine grained nanostructural product. The latter SAED pattern contains diffuse rings in addition to fine spotty rings. The formation of an amorphous product from Mg and Ni based starting elements is believed to result from the gradual accumulation of disorder without high enough local heating effects to result in crystallisation.

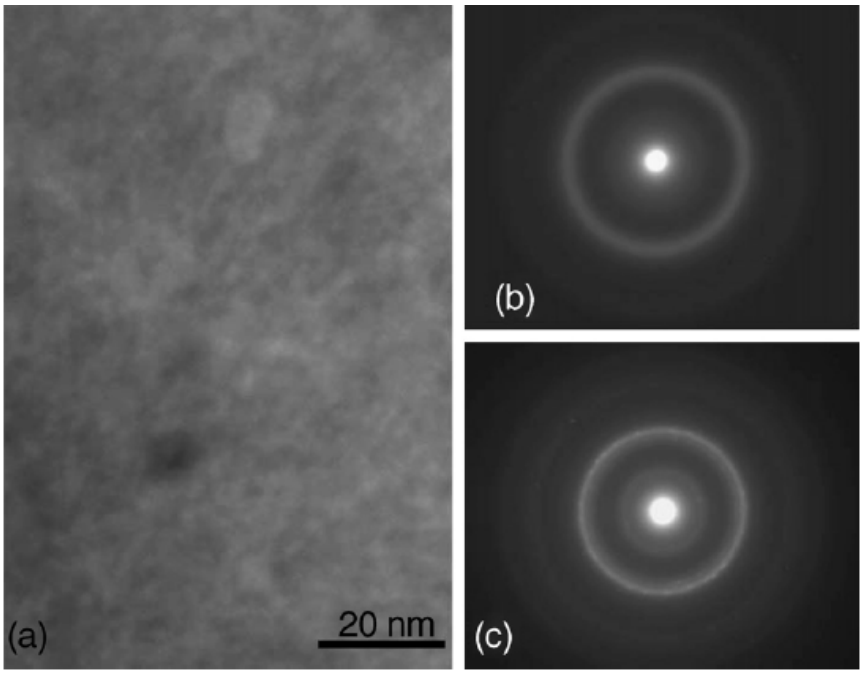

Fig. 4.3. Bright field and selected area electron diffraction (SAED) patterns obtained from as-prepared $Mg_{1.9}Cu_{0.1}Ni_{1.8}$: (a) TEM image, (b) SAED pattern of an amorphous region, and (c) SAED pattern of a region that was heated by the electron beam.

4.4 Thermal stability

The DSC traces of the as-prepared alloys are shown in Fig. 4.4. Each trace has a broad peak situated at around 150 ^{o}C, which is associated with the structural relaxation of the ball-milled amorphous structure. There are another two exothermic peaks in each trace, with the one at lower temperature related to crystallization of the as-prepared alloys into Mg_2Ni and the other at higher temperature related to the crystallization into $MgNi_2$ (Ruggeri et al. 2002a and Inoue et al. 2004). The temperature of crystallization into Mg_2Ni increases from 294 ºC to 351 ºC as the content of nickel increases from x = 1.8 to 2.1. The temperature of crystallization into $MgNi_2$ also goes up to higher temperatures from 406 ºC to 427 ºC. As the two crystallization temperatures increase with the increase of nickel content in the alloys, it can be concluded that nickel can help stabilize the amorphous structure of the as-prepared alloys.

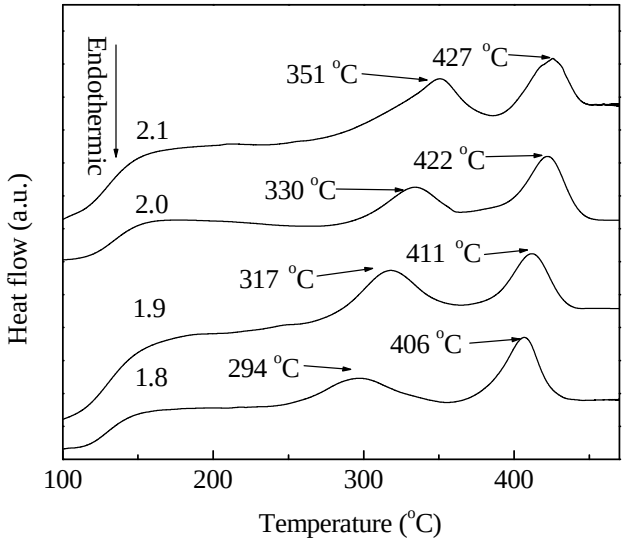

Fig. 4.4. DSC curves of the as-prepared $Mg_{1.9}Cu_{0.1}Ni_x$ (x = 1.8, 1.9, 2.0, and 2.1) alloys.

As was reported by Buschow et al. (1980), the crystallization of amorphous alloys is diffusion controlled, and the energy of activation is proportional to the formation

enthalpy ΔH of a hole having the size of the smaller atom. The hole formation enthalpy for an amorphous alloy $A_{1-x}B_x$ can be calculated by means of the following equation (Miedema 1979):

$$\Delta H_h^B = c\Delta H_{1V}^B + (1-c)(V_B/V_A)^{5/6}\Delta H_{1V}^A \quad (4.1)$$

Here, c is the effective concentration defined as

$$c_B = xV_B^{2/3}/\left\{xV_B^{2/3} + (1-x)V_A^{2/3}\right\} \quad (4.2)$$

where V represents the molar volume of an element (Miedema 1992). ΔH_{1V}^B and ΔH_{1V}^A are the formation enthalpies of the elements A and B. In this experiment, copper was used to substitute for a small percentage (around 5 at. %) of the magnesium, and its content in the alloy (2.5 at. %) is very small compared with that of the nickel (about 50 at. %). The atomic radius of copper (0.128 nm) is larger than that of nickel (0.124 nm). Based on these data, the effect of copper on crystallization may be ignored. During the following discussion $Mg_{1.9}Cu_{0.1}Ni_{2.0}$ is treated as MgNi. According to equations (4.1) and (4.2), the formation enthalpy of a nickel monovacancy in MgNi is given as

$$\Delta H_h^{Ni} = 0.376\Delta H_{1V}^{Ni} + 0.624(V_{Ni}/V_{Mg})^{5/6}\Delta H_{1V}^{Mg} \quad (4.3)$$

which is deduced to be 63.8 kJ/mol using ΔH_{1V}^{Ni} = 122 kJ/mol and ΔH_{1V}^{Mg} = 54 kJ/mol for the two metals (Miedema 1979).

According to Buschow's model, there is a linear relationship between the crystallization temperature (T_c) and the formation enthalpy (ΔH):

$$T_c = C\Delta H \quad (4.4)$$

where C is between 7 and 8 when T_c is expressed in the units of K and ΔH is expressed in the units of kJ/mol (Buschow 1981). The calculated values of ΔH_h^{Ni}, according to

(4.1) and (4.2), are 61.5 kJ/mol, 62.6 kJ/mol, 63.8 kJ/mol, and 64.9 kJ/mol, corresponding to nickel contents x = 1.8, 1.9, 2.0, and 2.1, which means that the hole formation enthalpies of nickel in the alloys increase with increasing nickel content. According to (4.4), the crystallization temperature should increase with the increasing nickel content, which is verified by the DSC traces (Fig. 4.4).

XRD patterns of the as-prepared alloys annealed at 600 ^{o}C for two hours in argon are shown in Fig. 4.5. It was found that there were three phases (Mg_2Ni, $MgNi_2$, and a small amount of Mg) in the annealed samples. There was no evidence of Mg_2Cu, which suggests that the copper had presumably been dissolved into Mg_2Ni and/or $MgNi_2$ (Ikeda 1998). Since $MgNi_2$ does not form a hydride, and it constitutes such a high percentage in the annealed alloys, it is very important to avoid the formation of $MgNi_2$ during hydrogen cycling.

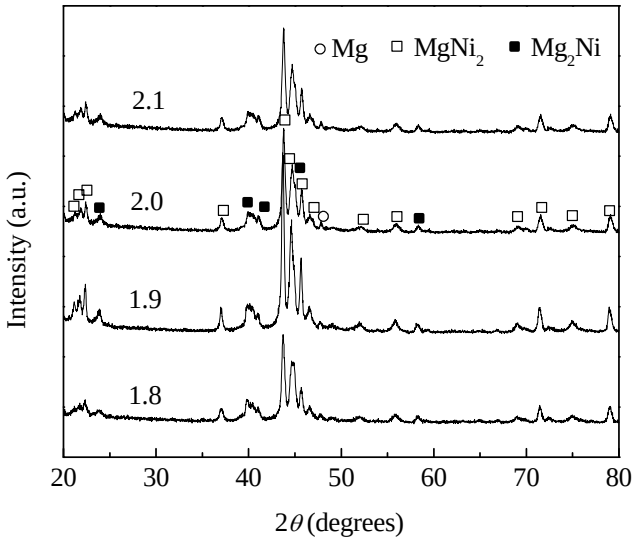

Fig. 4.5. XRD patterns of the as-prepared $Mg_{1.9}Cu_{0.1}Ni_x$ (x = 1.8, 1.9, 2.0, and 2.1) alloys annealed at 600 ^{o}C for two hours.

4.5 Hydrogenation and desorption

4.5.1 200 ^{o}C

Figure 4.6 reveals the XRD patterns of the as-prepared alloys hydrogenated at 200 ^{o}C in 5 atm. hydrogen for 20 mins. These patterns are similar to those of the as-prepared alloys (Fig. 4.2). It is hard to judge from the XRD pattern whether there is hydride in the alloys, since there are no visible hydride peaks.

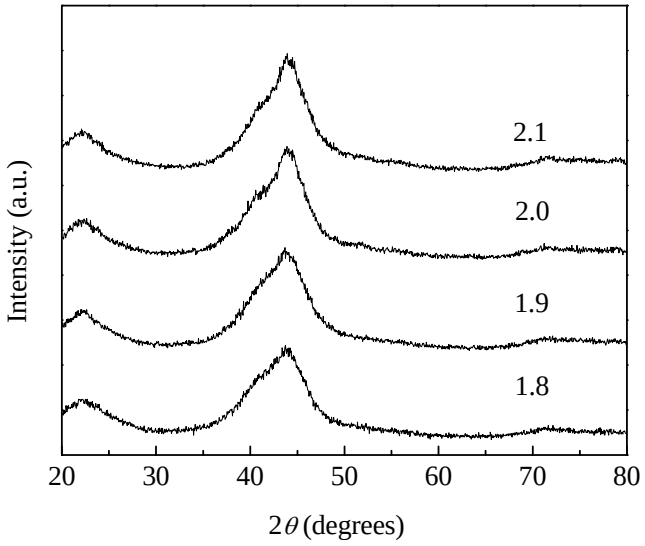

Fig. 4.6. XRD patterns of the as-prepared $Mg_{1.9}Cu_{0.1}Ni_x$ (x = 1.8, 1.9, 2.0, and 2.1) alloys hydrogenated at 200 ^{o}C in 5 atm. hydrogen for 20 mins.

However, there are endothermic peaks in the DSC curves (Fig. 4.7) that certify the existence of hydrides in all the alloys. The lack of hydride peaks in Fig. 4.6 is presumably due to: (1) the amount of hydride being below the level of detection of the X-ray diffractometer, and (2) hydride being in the form of nanocrystals. As can be seen from these DSC traces, the peak temperature decreases from 235 ^{o}C to 213 ^{o}C as the nickel content increases from x = 1.8 to 2.1. The origins of the endothermic peaks at

about 350 °C are not clear at this stage. The exothermic peaks marked by the circle in the upper right corner are attributed to the crystallization into $MgNi_2$.

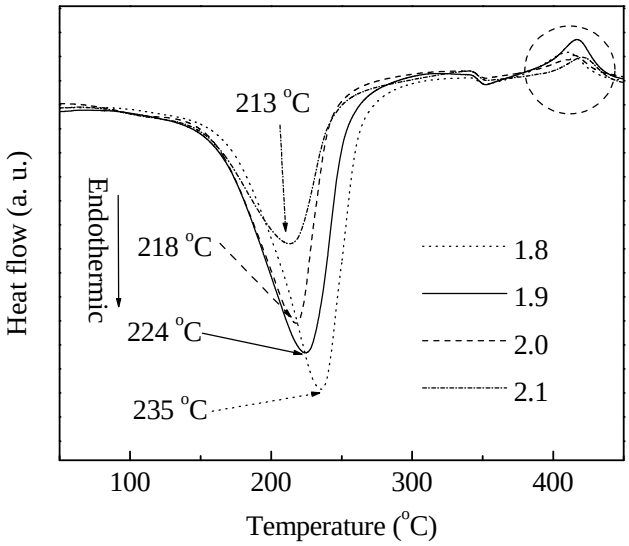

Fig. 4.7. DSC traces of the as-prepared $Mg_{1.9}Cu_{0.1}Ni_x$ (x = 1.8, 1.9, 2.0, and 2.1) alloys hydrogenated at 200 °C in 5 atm. hydrogen for 20 mins.

4.5.2 250 °C

The XRD patterns of alloys hydrogenated at 250 °C in 5 atm. hydrogen for 20 mins are shown in Fig. 4.8. In the pattern of $Mg_{1.9}Cu_{0.1}Ni_{1.8}$, there are peaks related to Mg_2NiH_4. The intensity of the Mg_2NiH_4 peaks decreases with increasing nickel content, until it is below the level of detection when the nickel content reaches 2.1. The crystallite size of Mg_2NiH_4 in $Mg_{1.9}Cu_{0.1}Ni_{1.8}$ is only several nanometers.

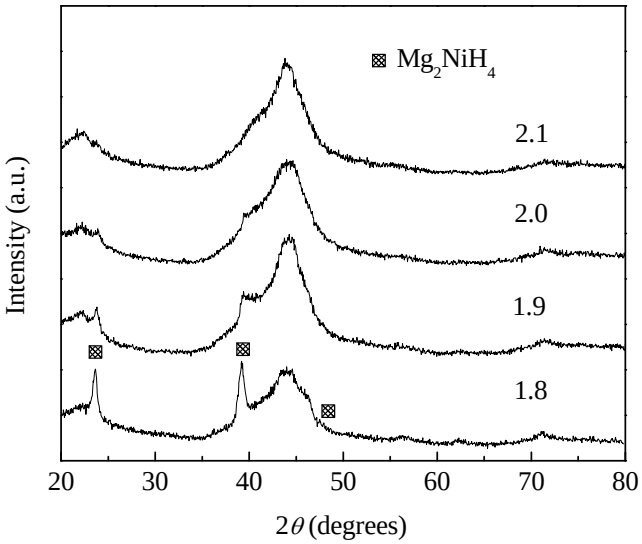

Fig. 4.8. XRD patterns of the as-prepared $Mg_{1.9}Cu_{0.1}Ni_x$ (x = 1.8, 1.9, 2.0, and 2.1) alloys hydrogenated at 250 ^oC in 5 atm. hydrogen for 20 mins.

Figure 4.9 shows DSC traces of these alloys hydrogenated at 250 ^oC in 5 atm. hydrogen for 20 mins. The peak temperature of endothermic peaks resulting from the decomposition of Mg_2NiH_4 decreases from 260 ^oC to 222 ^oC when the nickel content increases from 1.8 to 2.1. Again, there are exothermic peaks in the upper right corner, which originate from the crystallization into $MgNi_2$. There are also unknown endothermic peaks situated at around 350 ^oC.

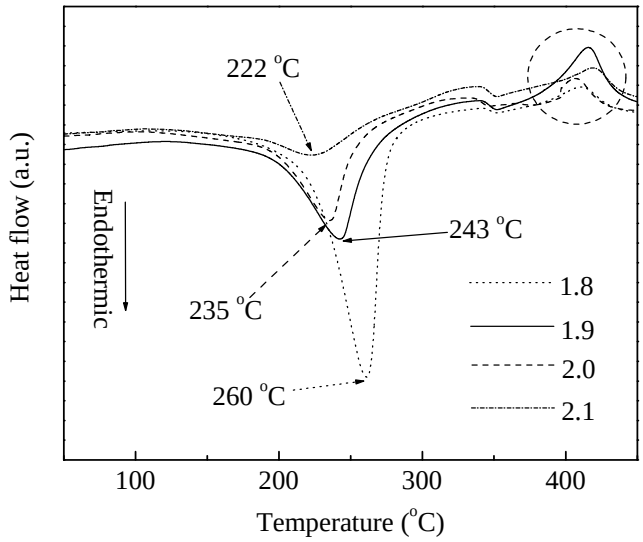

Fig. 4.9. DSC traces of the as-prepared $Mg_{1.9}Cu_{0.1}Ni_x$ (x = 1.8, 1.9, 2.0, and 2.1) alloys hydrogenated at 250 °C in 5 atm. hydrogen for 20 mins.

4.5.3 300 °C

Figure 4.10 shows XRD patterns obtained from alloys hydrogenated at 300 °C in 5 atm. hydrogen for 20 mins. Peaks corresponding to Mg_2NiH_4 are visible in all the patterns, with the intensity decreasing as the nickel content increases.

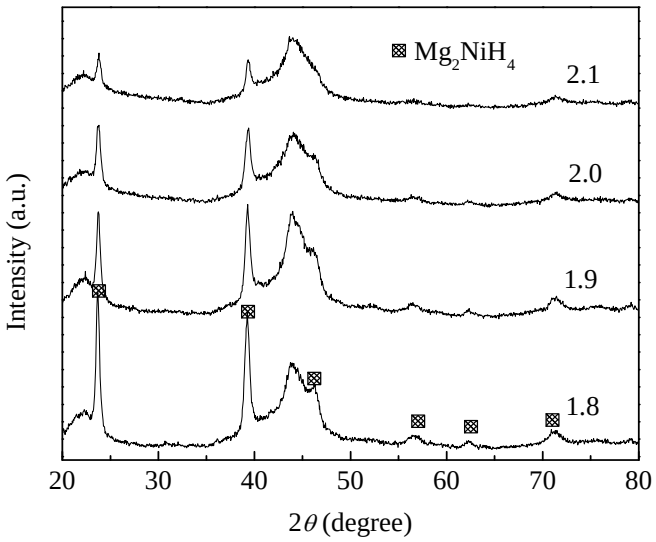

Fig. 4.10. XRD patterns of the as-prepared $Mg_{1.9}Cu_{0.1}Ni_x$ (x = 1.8, 1.9, 2.0, and 2.1) alloys hydrogenated at 300 ^oC in 5 atm. hydrogen for 20 mins.

Desorption information on the alloys hydrogenated at 300 ^oC in 5 atm. hydrogen for 20 mins can be deduced from the DSC traces shown in Fig. 4.11. The same trend was observed as was found in Fig. 4.7 and Fig. 4.9. However, the difference between the peak temperatures becomes very small, only a few degrees. Apart from the exothermic peak attributed to the crystallisation of the amorphous alloy into $MgNi_2$, another endothermic event was observed commencing at around 200 ^oC. This event was not detected in samples hydrogenated at 200 ^oC and 250 ^oC (Fig. 4.7 and Fig. 4.9), and the heat evolution associated with the endothermic event appeared larger for samples with lower Ni contents (1.8 and 1.9). The origin of this event is not clear.

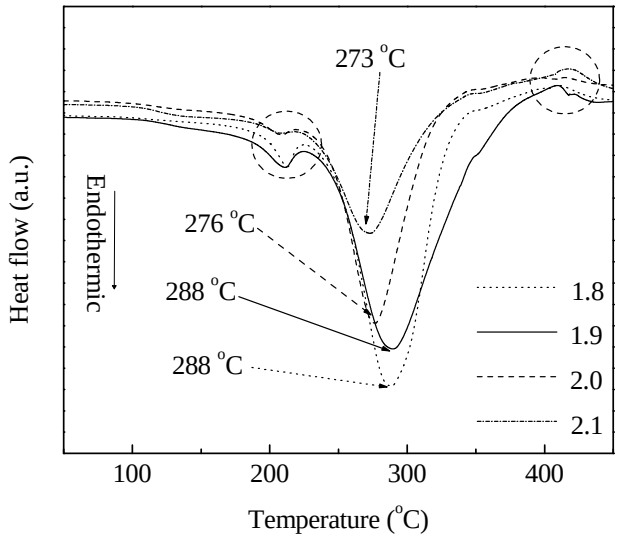

Fig. 4.11. DSC traces of the as-prepared $Mg_{1.9}Cu_{0.1}Ni_x$ (x = 1.8, 1.9, 2.0, and 2.1) alloys hydrogenated at 300 °C in 5 atm. hydrogen for 20 mins.

The variation of the peak desorption temperatures for all the alloys hydrogenated at 200 °C, 250 °C, and 300 °C is shown in Fig. 4.12. For each dehydrogenation temperature, there is a descending trend with increasing nickel content. However, the temperature difference becomes smaller when the hydrogenation temperature increases. For alloys with nickel content x = 1.8 and 2.1, there is a 38 °C difference when they are hydrogenated at 250 °C, compared with a 15 °C difference for the samples hydrogenated at 300 °C. The other notable point in the figure is that for the alloys with the same amount of nickel, the peak desorption temperatures increase with increasing hydrogenation temperature, which indicates that Mg_2NiH_4 becomes more stable with increasing hydrogenation temperature.

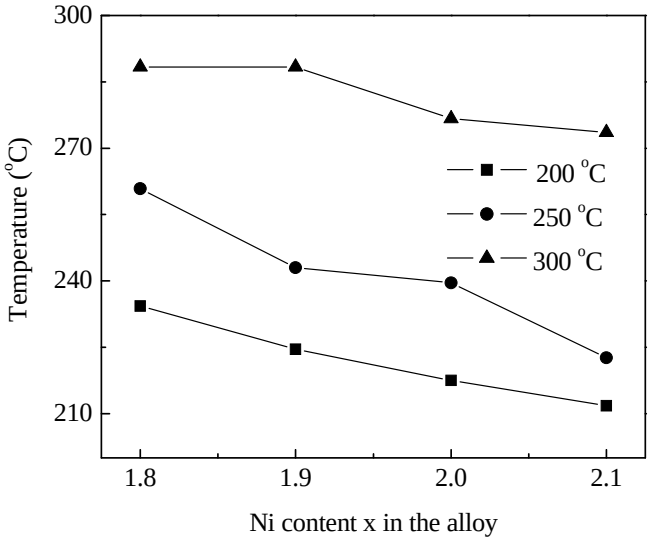

Fig. 4.12. Desorption peak temperatures of the as-prepared $Mg_{1.9}Cu_{0.1}Ni_x$ (x = 1.8, 1.9, 2.0, and 2.1) alloys hydrogenated at 200 °C, 300 °C, and 350 °C in 5 atm. hydrogen for 20 mins.

4.6 Effects of nickel content on hydrogenation and desorption

From the above results, we can see that the hydride formation and decomposition have a close relationship with the nickel content. This can be interpreted from the viewpoint of formation of nickel monovacancies. Amorphous structure exists in the as-prepared samples, as can be seen from the X-ray diffraction patterns (Fig. 4.2), although the nickel content varies from 1.8 to 2.1. The compositions of the alloys become very different from each other after hydrogenation, as evidenced by XRD (Fig. 4.6, Fig. 4.8, and Fig. 4.10). For hydrogenation carried out at the same temperature, there is more Mg_2NiH_4 in the alloys with lower nickel content, as can be deduced from the main DSC endothermic peak areas (Fig. 4.7, Fig. 4.9, and Fig. 4.11). This is corroborated by the stronger Mg_2NiH_4 peaks in the alloys in the XRD patterns (Fig. 4.6, Fig. 4.8, and Fig. 4.10).

There are three types of regions in the hydrogenated alloys: the intra-grain region of Mg_2NiH_4, the amorphous regions, and the interfaces between Mg_2NiH_4 grains and between Mg_2NiH_4 and neighboring amorphous regions. This is similar to the model that S. Orimo used to interpret the notable hydriding properties of Mg-Ni alloys (Orimo et al. 1998 and 2001). The volume fraction ratios of the three regions are different with different nickel contents; more specifically, the higher the nickel content, the higher the volume fraction of amorphous regions, the lower the volume fraction of Mg_2NiH_4, and the higher the volume fraction of the interfaces. Considering the formation enthalpy of nickel monovacancies in the alloys, this variation can be easily explained. The calculated formation enthalpies of nickel monovacancies in the alloys are 61.5 kJ/mol, 62.6 kJ/mol, 63.8 kJ/mol, and 64.9 kJ/mol, increasing with nickel content from x = 1.8 to 2.1, which means that it is very easy for an alloy with lower nickel content to crystallize (Fig. 4.4). In the magnesium and nickel based amorphous alloys, the magnesium and nickel atoms are arranged randomly. There are no favorable interstitial sites to accommodate hydrogen atoms. In crystallized alloys, the orderly arrangement of atoms gives rise to favourable interstitial sites for hydrogen to occupy. Consequently, at the same hydrogenation temperature, more Mg_2NiH_4 forms in the alloys with lower nickel content, since they can crystallize more easily than alloys with higher content. The alloy hydrogenated at 300 ^oC with the lowest nickel content shows the highest hydrogen storage capacity (around 2.3 wt. % for x = 1.8), while the alloy with the highest nickel content has the lowest capacity (1.4 wt. % for x = 2.1).

These results appear to contradict those of S. Orimo et al. (1998 and 2001), who found that the capacity increased from 1.7 wt. % to 2.2 wt. % when the nickel content increased from 33 at. % to 50 at. % for the Mg-Ni system. However, this is likely due to

differences between the starting powders and milling methods used. In their experiment, bulk Mg_2Ni was ball milled with additional nickel in argon, and then in hydrogen, so that nanostructured Mg_2Ni already existed in the ball-milled alloys, even for 50 at. % nickel. Hydrogenation took place during ball milling, and the hydrogen content in the inter-grain regions was very high, which can be attributed to the catalytic effect on hydrogen absorption that was induced by the impacts of the balls. In this experiment, the hydrogenation was carried out in hydrogen during heat treatment. The as-prepared amorphous alloy does not supply favourable interstitial sites for hydrogen atoms (Au 2005). During heating, both magnesium and nickel atoms move, with a more and more ordered arrangement obtained, which then provides the sites for hydrogen to occupy.

The relation between peak desorption temperatures and nickel content can also be interpreted in terms of the formation of nickel monovacancies. According to the calculation, more energy is needed for crystallization, or expressed in another way, for an ordered arrangement of atoms, when the nickel content increases. As deduced from X-ray diffraction (Fig. 4.8 and Fig. 4.10), the grain size of Mg_2NiH_4 becomes smaller when the nickel content increases, which is consistent with the proposition that amorphous regions in the alloy suppress the formation and growth of Mg_2NiH_4. It is well known that smaller grain size contributes to hydrogen desorption, mainly due to the reduction in the hydrogen diffusion distance. Therefore, the peak desorption temperature decreases when the nickel content increases. In addition, the amorphous region is also a nickel-rich area. Nickel may play an important catalytic role in facilitating hydrogen desorption and, as a result, lowers the desorption temperature.

4.7 Conclusions

The thermal stability and hydriding/dehydriding properties of ball-milled amorphous $Mg_{1.9}Cu_{0.1}Ni_x$ (x = 1.8, 1.9, 2.0, and 2.1) alloys were discussed. X-ray diffraction patterns and DSC traces indicate that the thermal stability and hydriding/dehydriding properties are closely related to the nickel content. The underlying reason is attributed to the formation of nickel monovacancies during heating and its associated affects on crystallization. Since the formation of nickel monovacancies dominates the crystallization process, namely, the ordered arrangement of atoms, it controls the formation of suitable interstitial sites for hydrogen to occupy. The calculated formation enthalpies of nickel monovacancies are 61.5 kJ/mol, 62.6 kJ/mol, 63.8 kJ/mol, and 64.9 kJ/mol, corresponding to nickel content x = 1.8, 1.9, 2.0, and 2.1, respectively. This result indicates that the higher the Ni content, the more stable the amorphous alloy and the smaller the amount of hydrides formed at the same hydrogenation temperature. On the other hand, the alloys with higher nickel content display lower desorption temperatures, which is due to the formation of hydrides with smaller crystallite sizes.

Chapter 5

Electrochemical properties of

$Mg_{1.9}Cu_{0.1}Ni_x$ (x = 1.8, 1.9, 2.0, and 2.1) alloys

5.1 Introduction

It is well known that Ni has good electrochemical catalysis and electronic conductivity (Notten et al. 1991, Ye et al. 2000, and Fukumoto et al. 1995), and many researchers (Inoue et al. 2004, Senoh et al. 1998, and Nohara et al. 1998) have found that nickel has excellent catalytic activity during the hydrogen cycling process. With an additional 33.3 wt. % Ni added to Mg_2Ni, Nohara et al. (1998) achieved a maximum discharge capacity of 870 $mAhg^{-1}$, which is almost up to the theoretical capacity of 999 $mAhg^{-1}$ (Cui and Luo 1998). Inoue et al. (2004) found that Ni greatly improved the high rate discharge capability and cycle performance of $Mg_{0.9}Ti_{0.06}V_{0.04}Ni_x$ (x = 1.0, 1.1, 1.2, and 1.3). Zhang et al. (1999) have suggested that a Ni-enriched layer under the top surface of Mg-based alloy facilitates the hydriding and dehydriding processes, and Han et al. (2002) found that Ni was very effective in protecting the electrode surface from oxidation, which consequently improved the cycling performance. Cu can also act as a catalyst for the absorption and dissociation of hydrogen molecules. In hydrogen storage alloys, Cu substituted alloy shows an obvious improvement in the reaction rate and a decreased operating temperature (Li et al. 2002, Liang et al. 1998, and Liao et al. 2004).

The previous chapter has discussed the effect of nickel on the hydrogen storage properties of $Mg_{1.9}Cu_{0.1}Ni_x$ (x = 1.8, 1.9, 2.0, and 2.1) alloys through gas-solid reaction. In this chapter, I report on a series of measurements that were conducted in order to investigate the electrochemical properties of these alloys in relation to nickel content. The details of electrode preparation, battery construction, and electrochemical characterization can be found in Chapter 3.

5.2 Discharge capacities

Discharge capacities as a function of cycle number for the $Mg_{1.9}Cu_{0.1}Ni_x$ (x = 1.8, 1.9, 2.0, and 2.1) electrodes are shown in Fig. 5.1. The maximum discharge capacities, 490 $mAhg^{-1}$ for x = 1.8 and 435 $mAhg^{-1}$ for x = 2.1 were observed for the first cycle. The discharge capacity decreased during the subsequent cycles for all the four electrodes. However, the degradation of capacity increased as the nickel content in the alloys decreased. As for the electrode with x = 1.8, after 15 cycles the discharge capacity was approximately only 150 $mAhg^{-1}$, compared to 250 $mAhg^{-1}$ for x = 2.1. Evaluated from the percentage of degradation, that is $(C_1-C_{15})/C_1*100$ %, where C_1 represents the discharge capacity at the first cycle and C_{15} represents the capacity at the 15th cycle, the capacity decays were 66.7 %, 59.1 %, 57.1 %, and 47.2 %, with Ni content increasing from x = 1.8 to 2.1. Clearly, an increase in Ni content in the alloys can greatly enhance the cycle performance of the negative electrodes. Liang et al. (1998) and Liao et al. (2004) have found that Cu contributed little to the improvement of cycling performance, therefore, it is Ni that plays the major role in maintaining the cyclic stability.

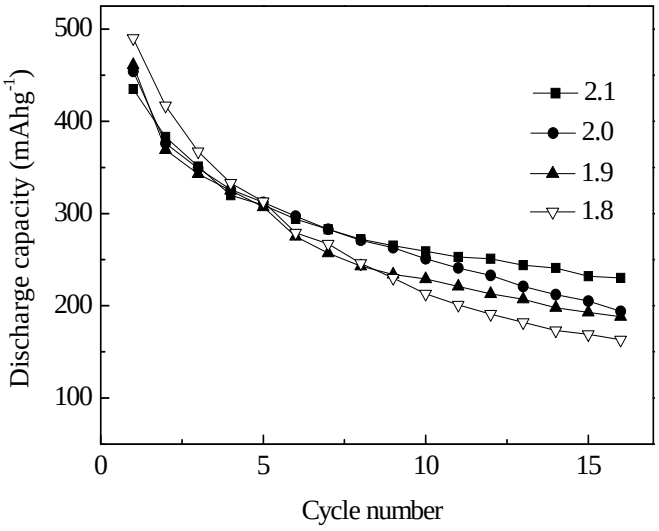

Fig. 5.1. Discharge capacities of $Mg_{1.9}Cu_{0.1}Ni_x$ (x = 1.8, 1.9, 2.0, and 2.1) alloy electrodes as a function of cycle number.

5.3 Cyclic voltammograms

Figure 5.2 shows cyclic voltammograms (CV) of $Mg_{1.9}Cu_{0.1}Ni_{1.9}$ before charge and after 5 cycles at room temperature. It shows a large redox reaction current density associated with hydrogen absorption and desorption before cycling. The current density decreased after five cycles, indicating that the number of active sites for hydrogen absorption and desorption in the alloys had decreased during the subsequent cycles. Abe et al. (2003) studied the CV of amorphous MgNi negative electrode using a special micropaste electrode technique. The shapes of their CV curves are different from these, although the potentials at i = 0 are similar. Because the working electrode they used was made by packing MgNi powder into a concave area in a tungsten metal bar with a diameter of 1mm, and the scan rate they used was 1 mV/s, instead of 10 mV/s, the polarization should be much smaller than in our experiment. According to other reports (Ma et al. 2005, Pasturel et al. 2003, and Cui et al. 2000), the degradation of capacity is

due to the corrosion of Mg, which forms $Mg(OH)_2$. This irreversible reaction has two results: a) reduction in the amount of active Mg metal atoms in the alloy, which play a major role in the hydrogen uptake and release; and b) formation of a shield which blocks the diffusion of hydrogen from the bulk to the surface and also in the opposite direction, thereby increasing the activation energy during the absorption and desorption.

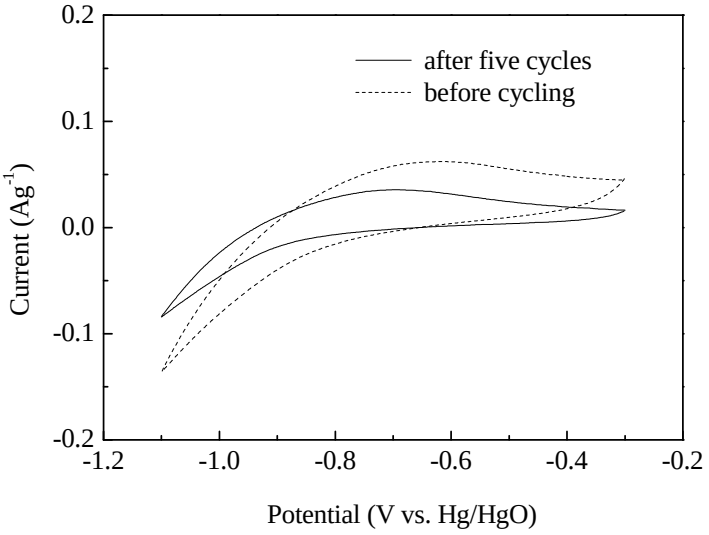

Fig. 5.2. Cyclic voltammograms for $Mg_{1.9}Cu_{0.1}Ni_{1.9}$ alloy electrode. Scan rate: 10 mV/s

Figure 5.3 shows the SEM morphologies and concentration distributions of Mg, Ni, Cu, and O in $Mg_{1.9}Cu_{0.1}Ni_{1.9}$ alloy electrode after five cycles. All the other electrode powders have similar morphology, so they are not shown here. It is clear that there are dense O atoms homogeneously distributed in the $Mg_{1.9}Cu_{0.1}Ni_{1.9}$. Because Mg is much more easily oxidized than Ni, most of the O atoms should combine with Mg, which means that Mg has been severely oxidized during cycling. Once oxidized, Mg loses the ability to absorb hydrogen. This verifies the above explanation of the cycle performance degradation. This figure also shows a uniform distribution of Mg, Cu, and Ni in the alloy, which means that no elemental agglomeration occurs during hydrogen absorption and desorption. Another point that needs to be made is that the morphology of the

particles has changed after 5 charge/discharge cycles. There are some obvious edges in the as-prepared alloy particles (as shown in Chapter 4, Fig. 4.1), while the particles become round after several charge/discharge cycles. This is probably due to the reaction priority that the atoms in the edges are the first to react. Ma et al. (2005) observed the formation of a dense corrosion layer on MgNi powder after immersion in alkaline electrolyte solution, but no appreciable content of $Mg(OH)_2$ was found after MgNi was ball milled with Pd, a modification that greatly improved the cycling performance. In this experiment, the EDS results show that the O concentration in the electrodes decreases as the Ni content in the alloy increases, which means that the formation of $Mg(OH)_2$ is inhibited. Consequently, the discharge capacity of an electrode with more Ni was kept comparatively higher for more cycles.

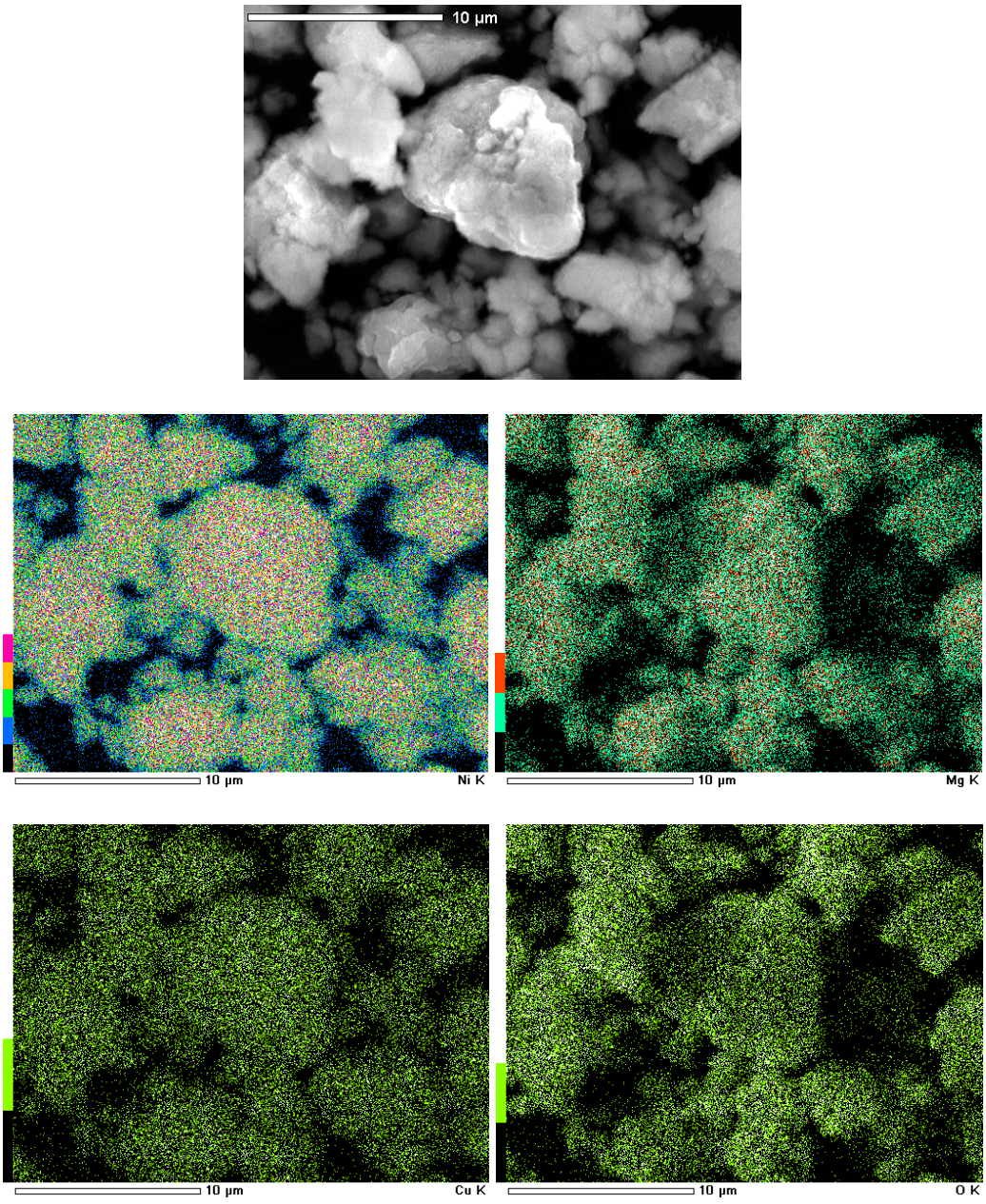

Fig. 5.3. SEM image and concentration distributions of Mg, Ni, Cu, and O in $Mg_{1.9}Cu_{0.1}Ni_{1.9}$ alloy electrode after five cycles.

Figure 5.4 shows the cyclic voltammograms of the alloys after 5 cycles. It is clear that the electrodes with higher nickel contents exhibit higher current density, which means that there are more active sites for hydrogen absorption/desorption after cycling when the nickel content is higher, and consequently, the cyclic stability is improved from x =

1.8 to 2.1. According to Zhang et al. (1999), there is a Ni enriched layer underneath the top surface of the alloy. The Ni enriched layer near the surface of the alloy acts as a protective shield for the elemental Mg. The shield suppresses the formation of $Mg(OH)_2$ and thereby improves the cyclic stability.

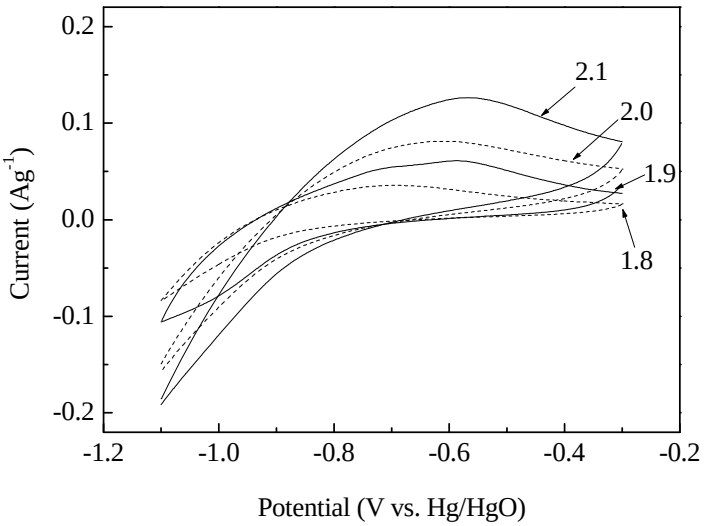

Fig. 5.4. Cyclic voltammograms for $Mg_{1.9}Cu_{0.1}Ni_x$ (x = 1.8, 1.9, 2.0, and 2.1) alloy electrodes after 5 cycles. Scan rate: 10 mV/s

5.4 Electrochemical impedance spectra

Figure 5.5 presents the electrochemical impedance spectra (EIS) of the alloy electrodes at 80 % depth of discharge after 15 cycles. It has been suggested (Luo and Cui 1998) that the semicircle in the high frequency region is characteristic of the charge-transfer process at the alloy/electrolyte interface, and the linear response in the low frequency region is indicative of hydrogen diffusion in the bulk alloy. When the depth of discharge is above 70 %, there will be a fast charge-discharge process and slow diffusion of hydrogen in the alloy electrode, because of the low hydrogen concentration in the metal

hydride electrode (Rongeat and Roué 2004 and Notten et al. 1991). As a result, the rate-determining process should be hydrogen diffusion when the depth of discharge is 80 %. However, as can be seen from the impedance spectra (Fig. 5.5), there is still a semicircle. Considering the electrode state, i.e. 80 % depth of discharge after 15 cycles, we believe that the semicircle is associated with the passivation layer on the electrode surface (Vogt et al. 1999). As the Ni content increases, the semicircle in the high-frequency region becomes smaller and even disappears. This might be ascribed to: 1) high electrocatalytic activity owing to the higher concentration of Ni; and 2) suppression of passivation on the electrode surface, which is also caused by the higher content of Ni.

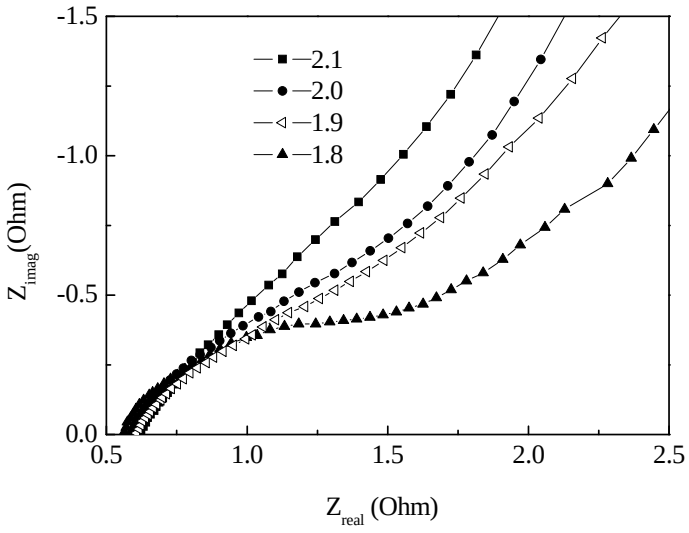

Fig. 5.5. Electrochemical impedance spectra (EIS) of $Mg_{1.9}Cu_{0.1}Ni_x$ (x = 1.8, 1.9, 2.0, and 2.1) alloy electrodes after 15 cycles at 80 % depth of discharge.

5.5 Exchange current density

The exchange current density I_o was determined from the linear polarization curves (Ruggeri et al. 2002b). The linear polarization curves were obtained at 1 mV/s at a small

overpotential versus the stabilized open circuit potential. Fig. 5.6 shows the linear polarization curves of the alloy electrodes at 20 % depth of discharge after 15 cycles. Obviously, there is a good linear dependence of the polarization current on overpotential, provided that it is small (up to 20 mV).

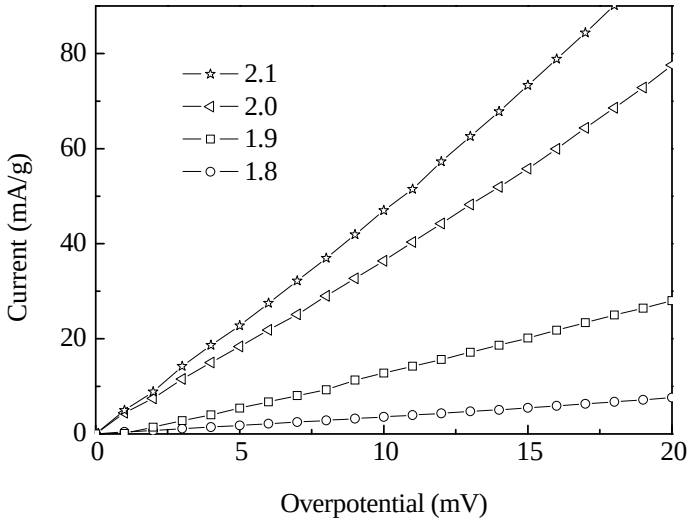

Fig. 5.6. Linear polarization curves of $Mg_{1.9}Cu_{0.1}Ni_x$ (x = 1.8, 1.9, 2.0, and 2.1) alloy electrodes after 15 cycles at 20 % depth of discharge.

The exchange current density I_o can be calculated according to the linearized form of the Butler–Volmer equation, which is valid at low overpotentials (Popov et al. 1996):

$$I = I_o F\eta / RT \quad (5.1)$$

where R is the gas constant, T the absolute temperature, F the Faraday constant, and η the overpotential. The calculated values of the exchange current densities are presented in Fig. 5.7. As is well known, the exchange current density I_o is an important kinetic parameter for the charge/discharge reaction. It represents the rate of hydriding/dehydriding, from which the reversibility and the discharge capacity can be evaluated. As can be seen from Fig. 5.7, with increasing Ni content, the exchange current density increases from 13 mAg^{-1} to 133 mAg^{-1}. Therefore, the electrocatalytic

activation of the electrodes increases with increasing Ni content, resulting in an increase of I_o. Combining this with the discharge curves (Fig. 5.1), CVs (Fig. 5.4), and EIS spectra (Fig. 5.5), it is evident that the Ni can reduce the resistance in the hydriding/dehydriding process, which consequently helps to improve the cycle performance.

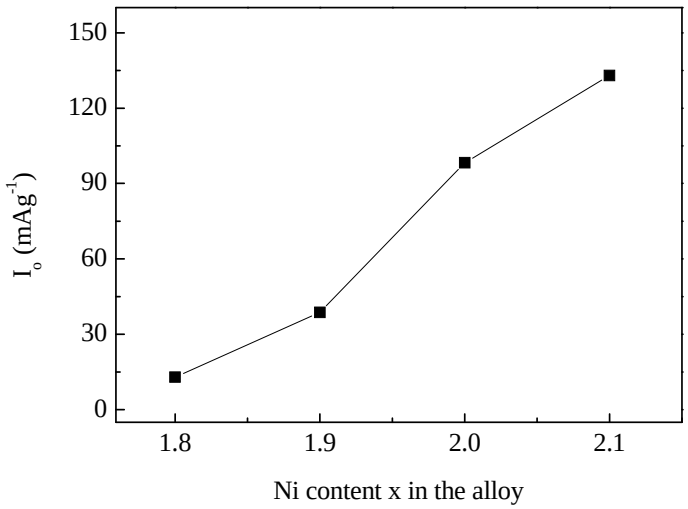

Fig. 5.7. Variation of exchange current density with x in $Mg_{1.9}Cu_{0.1}Ni_x$ (x = 1.8, 1.9, 2.0, and 2.1) alloy electrodes.

5.6 Conclusions

The effect of nickel content on the electrochemical properties of $Mg_{1.9}Cu_{0.1}Ni_x$ (x = 1.8, 1.9, 2.0, and 2.1) hydrogen storage alloys has been discussed in this chapter. Although the initial discharge capacity of the alloy electrodes with higher Ni content is slightly lower than the alloy electrodes with lower Ni content, the capacity decays are 66.7 %, 59.1 %, 57.1 %, and 47.2 %, as the Ni content increases from x = 1.8 to 2.1. The exchange current density of the electrode also increases with increasing Ni content, from 13 mAg^{-1} at x = 1.8 to 133 mAg^{-1} at x = 2.1. Clearly nickel can help maintain the

reversibility and discharge capacity over more cycles. The improvement in the electrochemical performance can be explained by the following facts: 1) the high electrocatalytic activity of Ni in alloys; and 2) the suppression of the formation of $Mg(OH)_2$ on the surface of electrodes.

Chapter 6

Effects of iron oxides on the hydrogen storage properties of magnesium

6.1 Introduction

It has been found that the introduction of transition metals (TMs), such as Nb, V, Cr, and Fe, can improve the hydrogen absorption/desorption kinetics of MgH_2 (Liang et al. 1999, Zaluska et al. 1999b, and Pelletier at al. 2001). The corresponding mixed valence transition metal oxides (TMOs), such as Nb_2O_5, V_2O_5, Cr_2O_3, and Fe_3O_4, have also shown very efficient catalytic effects (Bobet et al. 2005 and Oelerich et al. 2001). In some cases, the effects are even greater with the oxides than with the elemental metal (Barkhordarian et al. 2003). However, the exact mechanisms of the observed catalytic effects displayed by TMOs are not clear yet, and some controversy still exists. Yavari et al. (2005) proposed that the reduction of TMOs by magnesium generated a dispersion of TMs, and the TM–Mg interfaces were thought to act as catalysts to accelerate the hydrogen absorption kinetics and, in particular, the breaking up of the H_2 molecule into absorbable monotonic hydrogen (Yavari et al. 2003). On the other hand, Barkhordarian et al. (2003) claimed that TMs combined with oxygen played the most important role in the hydrogen absorption by improving the electronic exchange reactions with hydrogen molecules, which means that the TMOs will lose their catalytic properties once they are reduced.

As a multiple valence metal, Fe forms three types of oxides, i.e. FeO, Fe_2O_3, and Fe_3O_4. Both Fe_2O_3 (Song et al. 2005) and Fe_3O_4 (Barkhordarian et al. 2003 and Oelerich et al. 2001) have been studied, and catalytic effects on hydrogen cycling were discovered. The valence of Fe in Fe_2O_3 is +3, but in Fe_3O_4, two thirds of the Fe is +3, with the rest +2, resulting in a "nominal" valence of +8/3. Therefore, the differences in the electronic structure of Fe may result in different catalytic effects of the two oxides on hydrogen absorption and/or desorption. In order to clarify the proposition, we studied them as additives to magnesium, with an atomic ratio of magnesium to iron of 20:1. Ball milling was carried out using a Uni-Ball-Mill 5, with a low-energy shearing mode selected.

6.2 Properties of the as-prepared samples

6.2.1 X-ray diffraction

Figure 6.1 shows the XRD patterns of the as-prepared composites. Apart from the starting iron oxides in the composites, peaks of β-MgH_2 are visible in both patterns. For the as-prepared MgH_2 + Fe_3O_4 composite, there are still magnesium peaks in the XRD pattern (Fig. 6.1(b)), while such peaks are not visible in the XRD pattern of the as-prepared MgH_2 + Fe_2O_3 (Fig. 6.1(a)). The peak broadening in the XRD patterns is believed to be associated with the microstresses and the small grain size of the ball-milled particles.

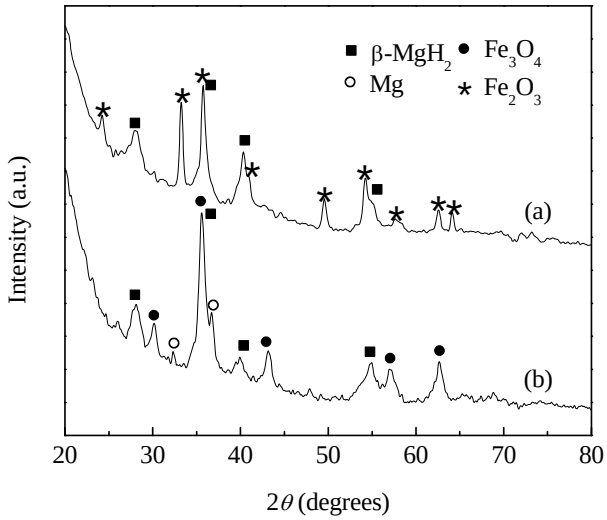

Fig. 6.1. XRD patterns obtained from the as-prepared composites: (a) MgH_2 + Fe_2O_3 and (b) MgH_2 + Fe_3O_4.

6.2.2 Morphology

Figure 6.2 shows the particle morphology of the as-prepared composites. For both samples, the particles have irregular shapes and have formed agglomerates, which is typical morphology for ball-milled powders. There is a broad particle size distribution for both samples, and the mean particle size is 300 nm for MgH_2 + Fe_2O_3 (Fig. 6.2(a)) and 400 nm for MgH_2 + Fe_3O_4 (Fig. 6.2(b)). Such a small particle size is favorable to hydrogen absorption and desorption because: 1) the particle specific surface area (SSA) is large, and 2) the diffusion length of hydrogen is dramatically reduced.

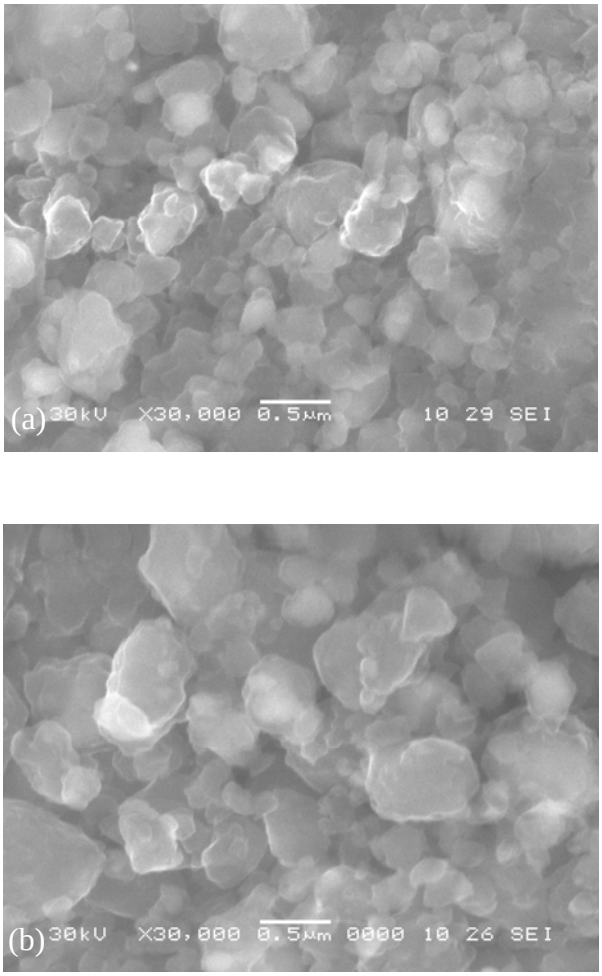

Fig. 6.2. SEM images of the as-prepared composites: (a) $MgH_2 + Fe_2O_3$ and (b) $MgH_2 + Fe_3O_4$.

6.2.3 DSC measurements

The thermal properties of the as-prepared composites can be deduced from the DSC curves (Fig. 6.3). As can be seen from the curves, there is little difference in the hydrogen desorption kinetics between the two samples. For both of them, the decomposition of β-MgH_2 starts at around 310 ^oC and ends at about 370 ^oC, with the peak temperatures occurring at about 340 ^oC. There is one broad exothermic peak situated at around 206 ^oC for the $MgH_2 + Fe_3O_4$ composite and 180 ^oC for the MgH_2 +

Fe_2O_3 composite, which is believed to be associated with the recrystallization of Mg (Varin et al. 2004). A broad endothermic peak is observed at around 290 ^oC for MgH_2 + Fe_2O_3 and 307 ^oC for MgH_2 + Fe_3O_4. The possible origins of the endothermic peak will be discussed in the next section.

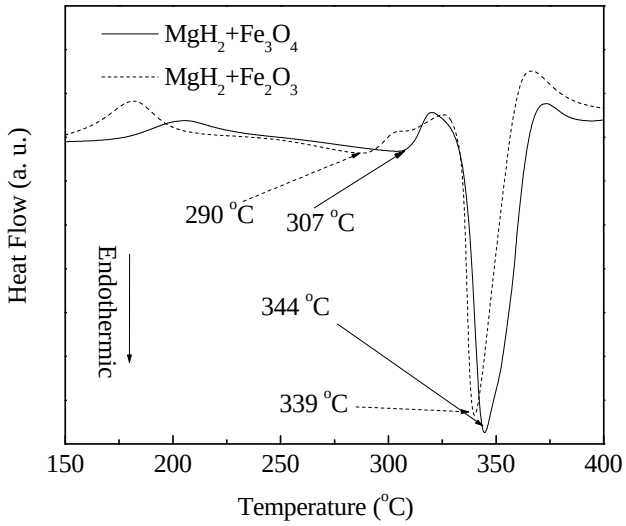

Fig. 6.3. DSC curves obtained from the as-prepared composites.

There is little difference in the hydrogen desorption kinetics between the two as-prepared composites, as can be seen in Fig. 6.4. For both of them, the desorption kinetics was sluggish, and after 15 minutes there was still about 2 wt. % hydrogen left in the composites.

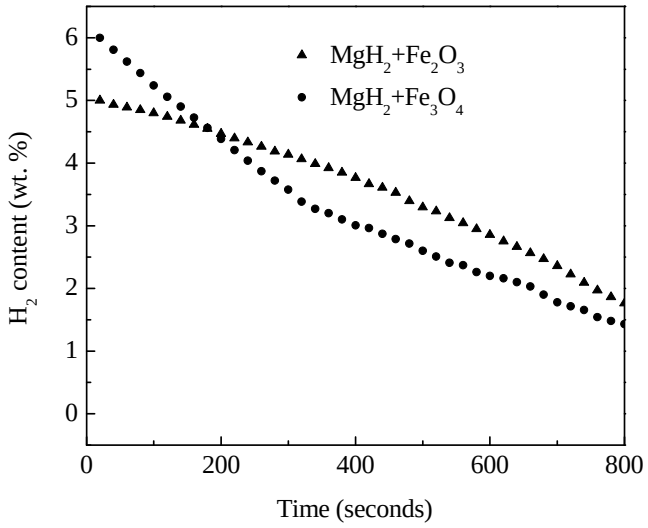

Fig. 6.4. Hydrogen desorption kinetics of the as-prepared composites at 350 ^{o}C under 0.05 MPa.

Figure 6.5 shows the weight percent of hydrogen in the as-prepared composites. There is about 6 wt. % and 5 wt. % of hydrogen stored in the as-prepared MgH_2 + Fe_2O_3 and MgH_2 + Fe_3O_4 composites, respectively. Considering the weight percentage of iron oxides in the starting composites and the theoretical capacity (7.6 wt. %) of magnesium hydride, there should be some elemental magnesium present in both the composites. This can be confirmed by the magnesium peaks in the XRD pattern (Fig. 6.1(b)) and the broad exothermic peaks resulting from the recrystallization of magnesium (180 ^{o}C for MgH_2 + Fe_2O_3 and 206 ^{o}C for MgH_2 + Fe_3O_4) in the DSC curves (Fig. 6.3).

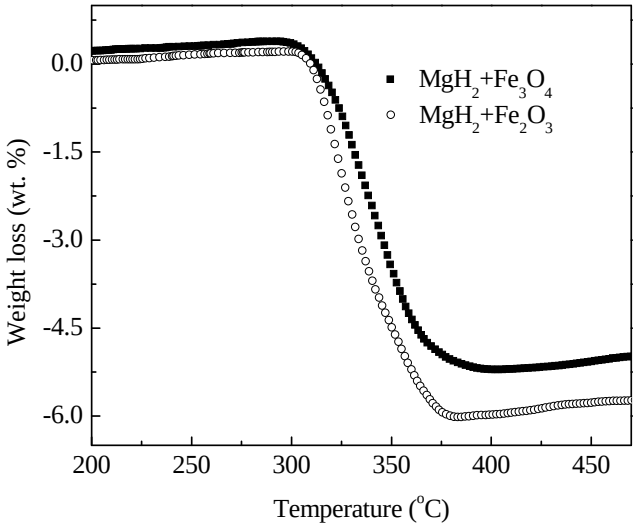

Fig. 6.5. TG curves obtained from the as-prepared composites.

6.3 Reactions during DSC measurements

Three DSC runs were stopped at 205 °C, 310 °C, and 368 °C for the as-prepared MgH_2 + Fe_2O_3 composites. The XRD patterns of the composites after heat treatment are shown in Fig. 6.6. As can be seen from the XRD patterns, there was iron in the composite when it was heated to 205 °C, implying that a reduction reaction had occurred before the decomposition of magnesium hydride. There was more iron in the composite when the temperature reached 310 °C, as can be deduced from the XRD Fe peak intensity. The reduction reaction during the heating can be expressed as:

$$3Mg + Fe_2O_3 = 2Fe + 3MgO \quad (6.1)$$

When the temperature reaches the value necessary for the decomposition of magnesium hydride, hydrogen will be released. Because magnesium is more reactive than hydrogen in terms of reducibility, magnesium should be the first to react with the iron oxide. In the starting materials, the atomic ratio of magnesium to iron is 20:1. Therefore,

according to equation (6.1), there is enough magnesium for reducing the Fe_2O_3, which means that hydrogen should be released completely from the as-prepared composites. When the temperature reached 368 ^oC, there was no hydride or iron oxide in the composites. Only iron, magnesium, and a small amount of magnesium oxide were present in the composite. This indicates that complete hydrogen desorption and reduction of iron oxide occurred during heating.

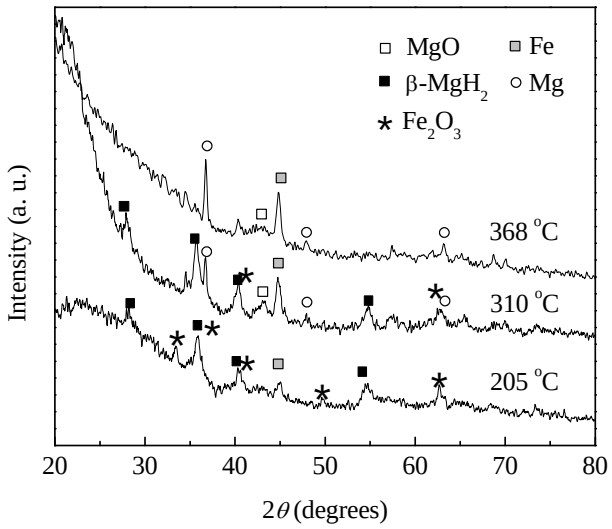

Fig. 6.6. XRD patterns obtained from MgH_2 + Fe_2O_3 composite after DSC heating of the as-prepared powders to 205 ^oC, 310 ^oC, and 368 ^oC.

Now the possible origin of the broad endothermic peak at about 290 ^oC in the DSC curve (Fig. 6.3) can be explained. When Mg was ball milled in hydrogen, both γ-MgH_2 phase and β-MgH_2 can be obtained, with the latter being the main component (Gennari at al. 2002). γ-MgH_2 is metastable and decomposes at a lower temperature (Huot et al. 1999). Magnesium coming from the decomposition reacts with Fe_2O_3, and this exothermic reduction reaction occurs over a wide temperature range. Consequently, the very broad endothermic peak at 290 ^oC originates from the concurrent exothermic

reduction reaction and endothermic decomposition of γ-MgH_2. γ-MgH_2 peaks are not visible in the XRD patterns (Fig. 6.1), which is due to: 1) the lower percentage of γ-MgH_2, and 2) very broad diffraction peaks and increased x-ray absorption, which is a result of the formation of a nanostructural and highly deformed milling product. These two factors make the diffraction peaks of γ-MgH_2 too broad and too weak to be distinguishable from the background.

Three DSC runs were stopped at 235 ^oC, 320 ^oC, and 378 ^oC for the as-prepared MgH_2 + Fe_3O_4 composite. XRD patterns of the composites after heat treatment are shown in Fig. 6.7. Iron peaks were not observed in the XRD pattern when the composite was heated to 235 ^oC, while clear iron peaks were found when the temperature reached 320 ^oC, implying that the following reaction may have occurred:

$$4Mg + Fe_3O_4 = 3Fe + 4MgO \quad (6.2)$$

Diffraction peaks of magnesium hydride and iron oxide disappeared when the temperature reached 378 ^oC, indicating that complete decomposition and reduction occurred during heating. Similarly, the broad endothermic peak at around 307 ^oC is possibly related to the concurrent exothermic reduction and endothermic decomposition of γ-MgH_2.

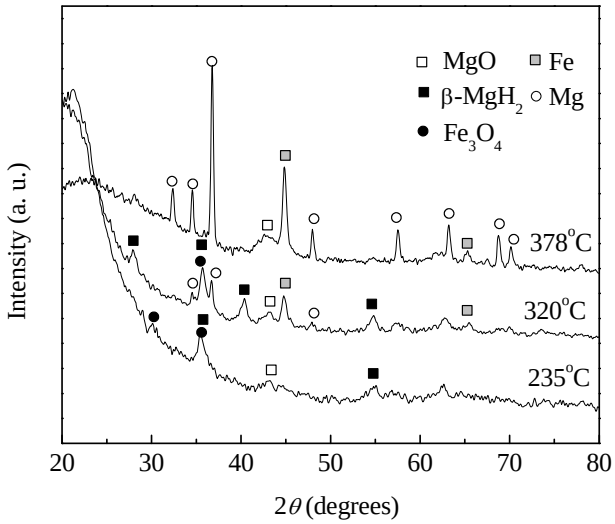

Fig. 6.7. XRD patterns obtained from MgH_2 + Fe_3O_4 composites after DSC heating of the as-prepared powders to 235 °C, 320 °C, and 378 °C.

It was found that both reduction reactions (Eq. (6.1) and Eq. (6.2)) started before the main hydride decomposition, and Fe_2O_3 and Fe_3O_4 were completely reduced after the main decomposition. In the as-prepared composites, the crystallite sizes of Fe_2O_3 and Fe_3O_4 that were calculated from the Williamson–Hall plot (as shown in Chapter 3, Eq. (3.2)) are 9.98 nm and 26.4 nm, respectively. This small crystal size facilitates the reduction reaction, because the diffusion path is greatly decreased and contact surface is increased. Consequently, both iron oxides were reduced at a low temperature during the DSC runs.

6.4 Hydrogen cycling behavior

Both composites reached saturation within 2 minutes, and the absorption kinetics are almost the same (Fig. 6.8). However, the amount of hydrogen absorbed by the MgH_2 +

Fe_3O_4 composite is 0.5 wt. % higher than the MgH_2 + Fe_2O_3 composite. The possible reasons are discussed later in this chapter.

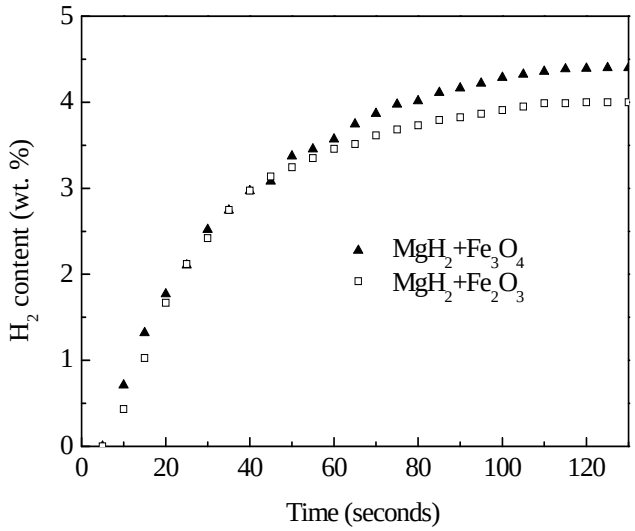

Fig. 6.8. Hydrogen absorption kinetics at 300 ^oC under 2 MPa.

XRD patterns of the rehydrogenated composites are shown in Fig. 6.9. Elemental magnesium peaks are not present in the patterns, which means that magnesium has reacted with hydrogen under the absorption conditions. Iron oxide peaks have disappeared completely in the rehydrogenated composites, with only elemental iron present. This renders it impossible to investigate the catalytic effects resulting from Fe_3O_4 and Fe_2O_3 on the hydrogen cycling properties of magnesium.

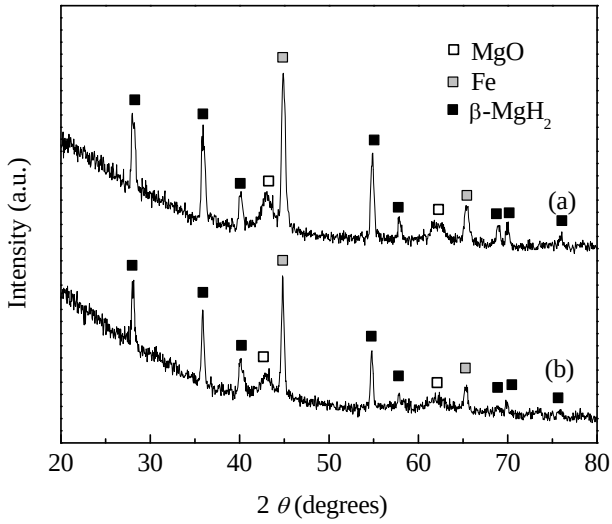

Fig. 6.9. XRD patterns obtained from rehydrogenated composites: (a) MgH_2 + Fe_2O_3, and (b) MgH_2 + Fe_3O_4.

The TG curves (Fig. 6.10) also reveal the capacity losses in both composites, compared with as-prepared samples (Fig. 6.5). The remaining capacity is 4.4 wt. % for MgH_2 + Fe_3O_4 composite and 4 wt. % for MgH_2 + Fe_2O_3 composite. This degradation is believed to be associated with the reduction reactions (Eq. (6.1) and (6.2)) occurring during heating. In these two iron oxides, the valence of Fe in Fe_2O_3 (+3) is higher than in Fe_3O_4 (+8/3). As a result, for the reduction of 1 mole Fe in each of the oxides to elemental Fe, more Mg is consumed (3/2 mole) for Fe_2O_3 than Fe_3O_4 (4/3 mole). Finally, there is less elemental Mg left in the MgH_2 + Fe_2O_3 composite than in the MgH_2 + Fe_3O_4 composite. This is the reason why there is a greater capacity loss for MgH_2 + Fe_2O_3.

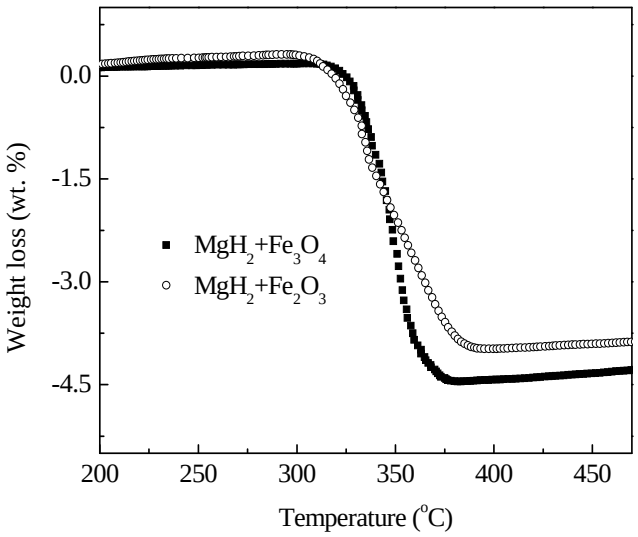

Fig. 6.10. TG curves obtained from the rehydrogenated composites.

Figure 6.11 shows the DSC properties of the rehydrogenated composites. There is almost no difference in the peak desorption temperature between the rehydrogenated composites. The only endothermic peak is attributed to the decomposition of β-MgH_2, since the γ-MgH_2 phase is metastable in the as-prepared composites and has been removed (Huot et al. 1999 and Bortz et al. 1999).

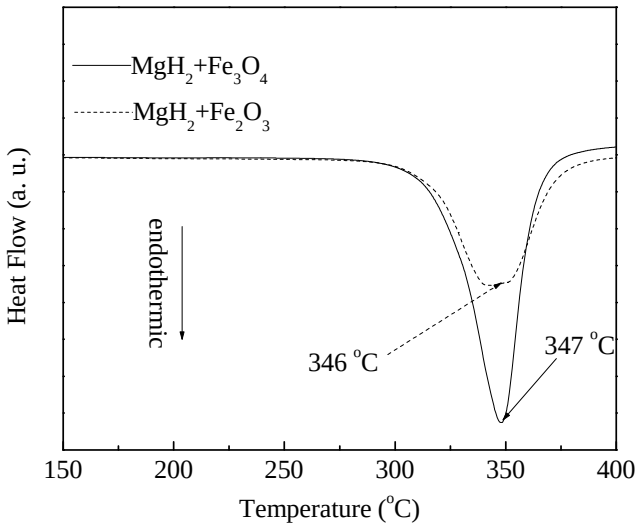

Fig. 6.11. DSC curves obtained from the rehydrogenated composites.

The hydrogen desorption kinetics of the rehydrogenated composites is shown in Fig. 6.12. The composites display a similar desorption behavior, with hydrogen released completely after just 6 minutes. This is consistent with the DSC results (Fig. 6.11). The reduction reactions (Eq. (6.1) and (6.2)) can shed light on this similarity. The differences in the electronic structures of the Fe between the two iron oxides were eliminated by the reduction reaction. Only elemental iron was present in the rehydrogenated composites. Consequently, the proposed improved electronic exchange reaction with hydrogen (Barkhordarian et al. 2003) caused by oxides did not occur. Additionally, in both composites, the Mg-Fe interfaces are presumably the same as the result of the reduction reactions.

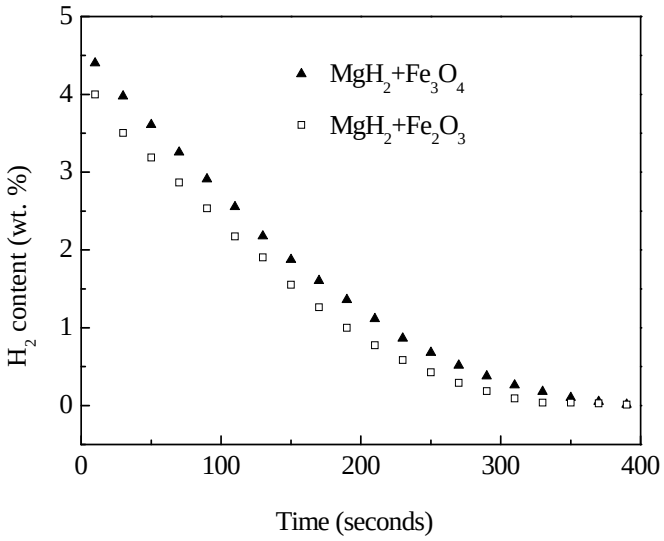

Fig. 6.12. Hydrogen desorption kinetics of the rehydrogenated composites at 350 ^{o}C under 0.05MPa.

6.5 Conclusions

Magnesium hydride and iron oxide composites were synthesized through a low-energy shearing mode magneto-ball-milling. The particle sizes of the as-prepared composites

were very small, around 300 nm for MgH_2 + Fe_2O_3 and 400 nm for MgH_2 + Fe_3O_4. There was little difference in the main peak decomposition temperature between the two as-prepared samples. During the hydrogen desorption of the as-prepared composites, both Fe_2O_3 and Fe_3O_4 were reduced by magnesium, with elemental Fe existing in the dehydrogenated composites. For the rehydrogenated composites, little difference was observed in the peak desorption temperatures. The desorption kinetics are very similar, with hydrogen release completed within 6 minutes. These similarities are presumably associated with the reduction reaction, which results in identical compositions and TM-Mg interfaces in the rehydrogenated composites. The greater capacity degradation of rehydrogenated MgH_2 + Fe_2O_3 composite is also a result of the reduction reaction, during which more magnesium was consumed than was consumed by the same amount of Fe_3O_4.

Chapter 7

Improvement in the hydrogen storage properties of magnesium through adding carbon allotropes

7.1 Introduction

Carbon allotropes such as graphite and carbon nanotubes have been tried as additives in an attempt to improve the hydrogen storage properties of magnesium. Imamura et al. (2000 and 2002) studied magnesium/graphite composites with and without organic additives. They found that organic additives helped to protect graphite from irregular breakage during ball milling and that the graphite/Mg composite showed enhanced hydrogen storage properties. In contrast, composite prepared without organic additives showed negligible improvement, and the graphite was broken irregularly. Shang et al. (2004) also found that graphite facilitated the absorption of hydrogen, apparently acting as a catalyst for the reaction. In contrast, amorphous carbon showed no benefits for hydrogen cycling. These authors attributed the improvement to the interaction of crystalline graphite with Mg and the formation of thin graphite flakes with cleavage planes during ball milling. Chen et al. (2004) found that carbon nanotubes in Mg based alloys not only helped to maintain the maximum hydrogen storage capacities but also contributed to hydrogen absorption/desorption kinetics.

There has been no comparative study of the effects of three additives: amorphous carbon black (CB) with its high specific surface area (SSA), graphite (G) with its layered structure, and multiwalled carbon nanotubes (MWCNT), on the hydrogen

storage properties of magnesium under the same conditions. In this experiment, these three carbon materials were ball milled with magnesium using a Uni-Ball-Mill 5. A low-energy shearing mode was applied. Differences in the effects of the three additives on the hydrogen storage properties of Mg were investigated.

7.2 Properties of the as-prepared composites

7.2.1 X-ray diffraction

Figure 7.1 shows XRD patterns obtained from the as-prepared composites. All the patterns indicate the presence of tetragonal β-MgH_2 (JCPDS, 12-0697) and a small amount of MgO. The peak broadening in the XRD patterns is believed to be associated with the combination of microstresses and the small grain size of the ball-milled particles.

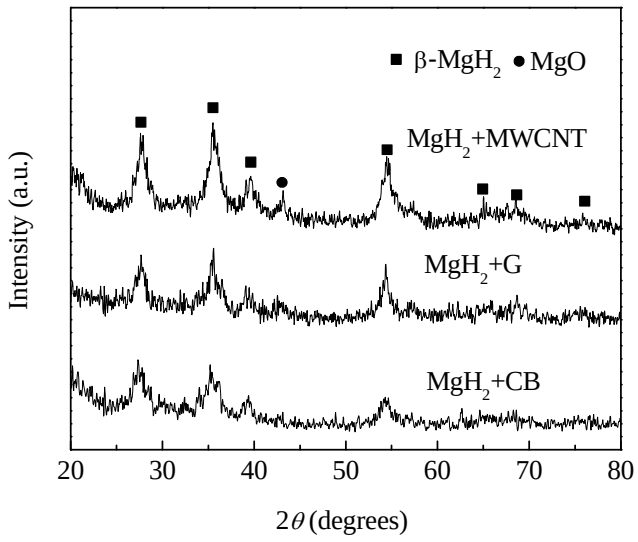

Fig. 7.1. XRD patterns obtained from the as-prepared composites.

7.2.2 Morphologies

The morphologies of the carbon allotropes and as-prepared composites, as revealed by SEM secondary electron imaging, are presented in Fig. 7.2. Energy dispersive x-ray spectroscopy (EDS) mapping of the composites confirms that the surfaces of the as-prepared composites are uniformly coated by the respective carbon allotrope (Fig. 7.2(c), Fig. 7.2(f) and Fig. 7.2(i)). Graphite flakes can not be detected after ball milling (Fig. 7.2(e)), which indicates that the structure has been broken during the ball milling. Because of the low magnifications employed, no MWCNT traces can be detected in the composite after milling (Fig. 7.2(h)). The weight percentages of carbon allotropes detected from EDS are all above 20 wt. %. Considering the initial weight percentage of 5 wt. %, it is reasonable to say that a large proportion of the carbon has accumulated on the surface. This can reduce the agglomeration of magnesium hydride particles.

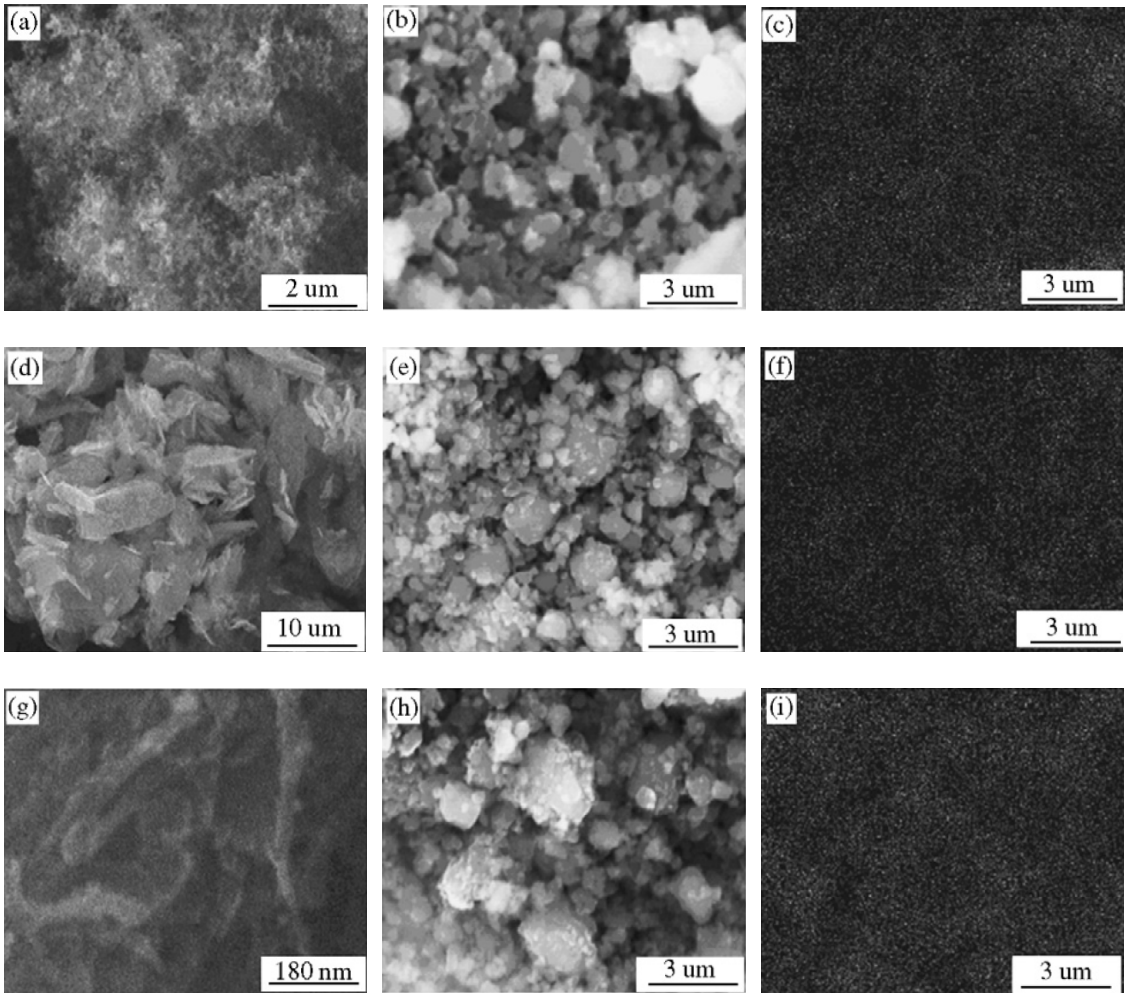

Fig. 7.2. SEM images of carbon allotropes and the as-prepared composites with associated EDS mapping for carbon: (a) CB, (b) MgH_2 + CB, (c) distribution of CB, (d) G, (e) MgH_2 + G, (f) distribution of G, (g) MWCNT, (h) MgH_2 + MWCNT, and (i) distribution of MWCNT.

The particle sizes of the CB, G, MWCNT, and the as-prepared composites obtained from a Nano ZS particle size analyser are listed in Table 7.1. Since all the particles are not round (Fig. 7.1), the value of the particle size accounts for the multi-dimensional factors affecting the size. The particle size of the starting carbon allotropes is about 2476 nm for G, 410 nm for CB, and 170 nm for MWCNTs. Among the as-prepared composites, the MgH_2 + MWCNT composite exhibits the largest particle size of 726 nm,

although MWCNT has the smallest particle size among the carbon materials. The MgH_2 + CB composite displays the smallest particle size of 494 nm, implying that CB facilitates the fragmentation of magnesium and/or magnesium hydride powder.

Table 7.1 Average particle sizes of carbon allotropes and the as-prepared composites.

Sample name	Average particle size (nm)
CB	410
G	2476
MWCNT	169
MgH_2+CB (as-prepared)	494
MgH_2+G (as-prepared)	503
MgH_2+MWCNT (as-prepared)	726

7.2.3 Raman spectra

The structural characteristics of the carbon allotropes attached to the surfaces of particles in the milled products can be inferred from the Raman spectra, as shown in Fig. 7.3. For carbon allotropes containing a mixture of sp^2 and sp^3 type C-C bondings, there are two particularly important bands, located at around 1330 cm^{-1} and 1590 cm^{-1}, designated as the D band and the G band, respectively. The relative intensity ratio of the D to the G band, I_D/I_G, can be related to the structural characteristics of carbon (Kastner et al. 1994). The ratio can give information about the perfection of the graphitic layered structure, reflecting the properties of the edge planes or boundaries of the graphite crystal faces. As the value of I_D/I_G rises, the defect structure generally increases and the degree of graphitization becomes smaller (Wang et al. 2004).

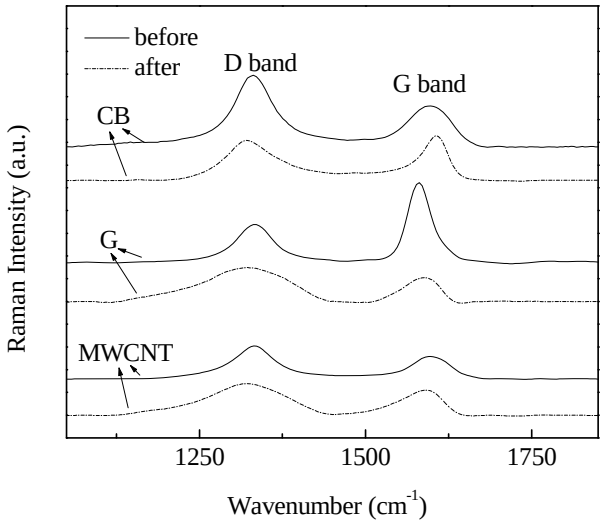

Fig. 7.3. Raman spectra of carbon black, graphite, and multiwalled carbon nanotubes before and after ball milling.

All the I_D/I_G ratios obtained from the spectra are listed in Table 7.2. It is clear that the graphite experienced the greatest structural disruption during ball milling, as the I_D/I_G ratio increased from 0.8 to 3.49 after ball milling. The graphitic structures in CB and MWCNT were partially damaged during ball milling, as evidenced by the small increase in the I_D/I_G ratio. The effects of ball milling on graphite and carbon nanotubes have been previously investigated, and similar results have been found (Pierard et al. 2004 and Tao et al. 2004).

Table 7.2 I_D/I_G values of carbon allotropes before and after ball milling.

Sample name	I_D/I_G (before)	I_D/I_G (after)
CB	1.6	2.1
G	0.8	3.49
MWCNT	1.8	2.2

7.2.4 Thermal properties

The thermal properties of the as-prepared composites were characterized using DSC, and the traces are displayed in Fig. 7.4. The variation in the onset temperatures is small, from 352 ^{o}C to 360 ^{o}C. There are two main peaks in the as-prepared composites. The smaller one, at around 370 ^{o}C, is attributed to the decomposition of γ-MgH_2, and the bigger one, at about 395 ^{o}C, is regarded as the decomposition of β-MgH_2 (Gennari et al. 2001 and Huot et al. 1999). The endothermic peak corresponding to the decomposition of β-MgH_2 has a much larger area than that of the peak corresponding to γ-MgH_2 decomposition, which means that β-MgH_2 is the main phase component in the composites. This can be verified from the XRD pattern (Fig. 7.1), in which peaks representing β-MgH_2 are visible, while peaks corresponding to γ-MgH_2 are not. The invisibility of γ-MgH_2 peaks is probably due to: 1) the small amount of γ-MgH_2, and 2) very broad diffraction peaks and increased x-ray absorption, which is a result of the nanostructural and highly deformed milled product. These two factors make the diffraction peaks of γ-MgH_2 too broad and too weak to be distinguishable from the background. The existence of γ-MgH_2 in the composites is believed to be a result of the ball milling, during which β-MgH_2 transforms into the metastable γ-MgH_2 (Huot et al. 1999). There are exothermic trends in the DSC curves at high temperature following the decomposition of hydrides. This is believed to be associated with the exothermic recrystallization of the ultra-fine magnesium formed during decomposition.

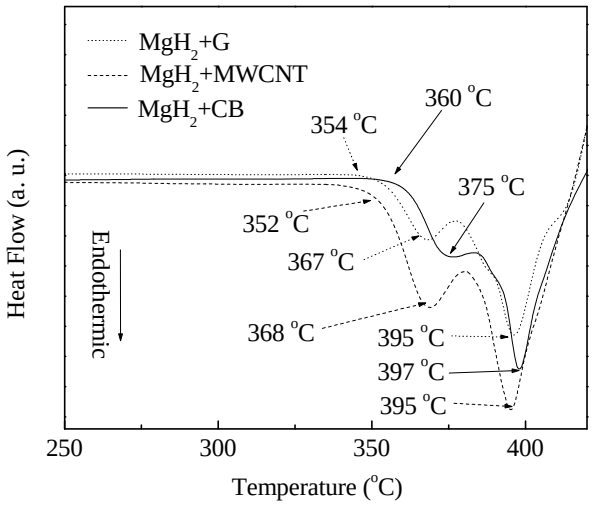

Fig. 7.4. DSC curves of the as-prepared composites as a function of temperature.

The desorption kinetics of the as-prepared composites at 350 °C are presented in Fig. 7.5. There is no significant difference in the desorption kinetics between the MgH_2 + CB and the MgH_2 + G composites. The desorption was faster for MgH_2 + MWCNT before the hydrogen content reached around 3 wt. %, but it became a little sluggish afterwards. To reach the same hydrogen content of 0.8 wt. %, it took around 20 minutes for MgH_2 + G, in contrast to 25 minutes for MgH_2 + MWCNT.

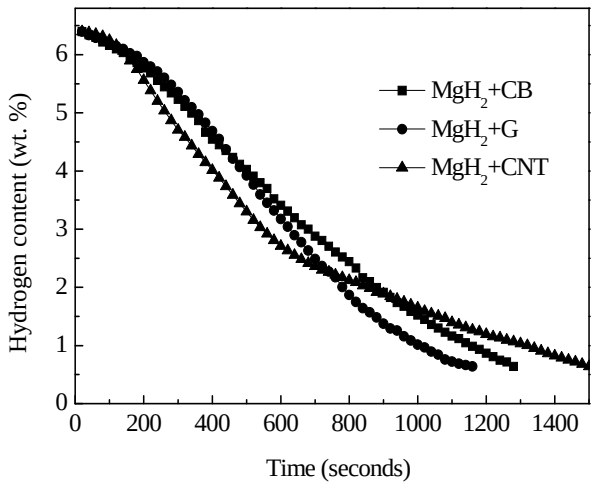

Fig. 7.5. Hydrogen desorption kinetics of the as-prepared composites at 350 °C at 0.05 MPa.

7.3 Hydrogen cycling properties

7.3.1 Hydrogen absorption

Among the three carbon allotropes, graphite shows a pronounced catalytic effect upon hydrogen absorption, as can be seen from Fig. 7.6. The MgH_2 + G composite reached its saturation level of about 6.2 wt. % after 1 minute, in contrast to 3 minutes for MgH_2 + CB and MgH_2 + MWCNT. Possible reasons for the improvement are discussed in Section 7.4

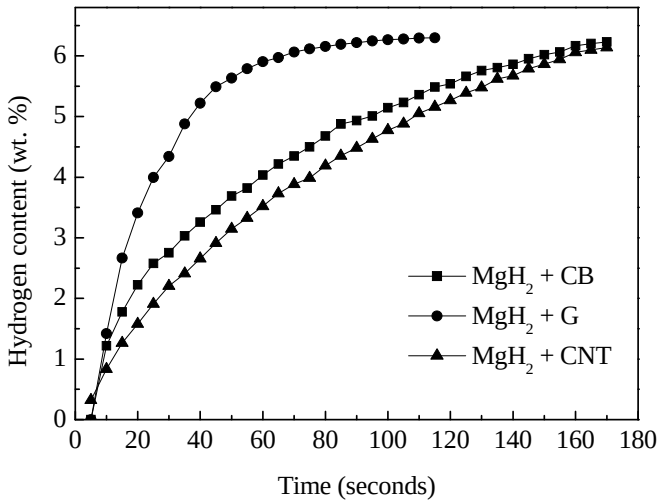

Fig. 7.6. First cycle hydrogen absorption kinetics of the composites at 300 ^{o}C under 2 MPa.

XRD patterns obtained from the rehydrogenated composites are shown in Fig. 7.7. There are strong signals of β-MgH_2. Mg peaks are not visible, implying that almost all the magnesium has reversibly changed into magnesium hydride under the absorption conditions. A very small amount of magnesium oxide is present for both composites. Peaks associated with γ-MgH_2 are not visible. Since γ-MgH_2 phase is metastable in the

ball-milled samples and can be removed when the samples are heated to 300 ^{o}C (Huot et al. 1999 and Bortz et al. 1999), it is believed that γ-MgH_2 is not present in any of the rehydrogenated composites. The peaks corresponding to β-MgH_2 after cycling are much sharper and more intense than those before cycling, which is attributable to: (i) the elimination of microstresses and (ii) the grain growth during hydrogen cycling.

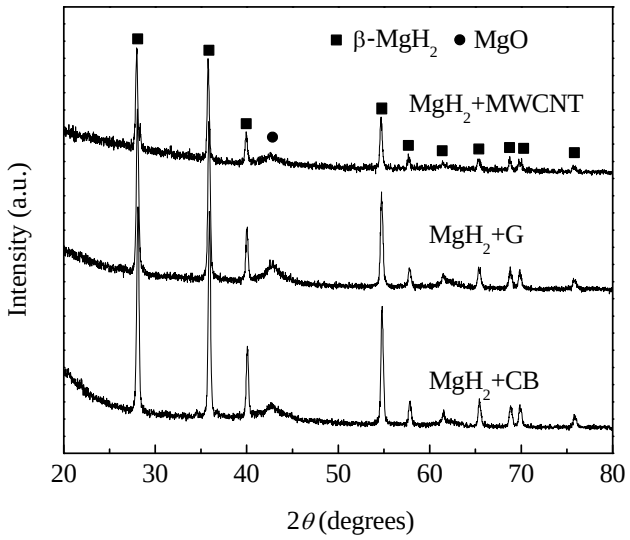

Fig. 7.7. XRD patterns obtained from the rehydrogenated composites.

7.3.2 Hydrogen desorption

The DSC traces of the first cycle rehydrogenated composites are presented in Fig. 7.8. The only endothermic peak is attributed to the decomposition of β-MgH_2, since γ-MgH_2 phase has been removed by the previous heating to 300 ^{o}C (Huot et al. 1999 and Bortz et al. 1999), which can be corroborated by the XRD patterns in Fig. 7.7. MgH_2 + G composites display a significant improvement compared with MgH_2 + CB and MgH_2 + MWCNT in terms of the onset temperature and the peak decomposition temperature. The onset temperature of MgH_2 + G is about 30 ^{o}C lower than those of MgH_2 + CB and

MgH_2 + MWCNT, and the peak decomposition temperature is more than 25 ^oC lower than the other two rehydrogenated samples. These means that β-MgH_2 in the rehydrogenated MgH_2 + G started decomposing at lower temperature than the other two composites.

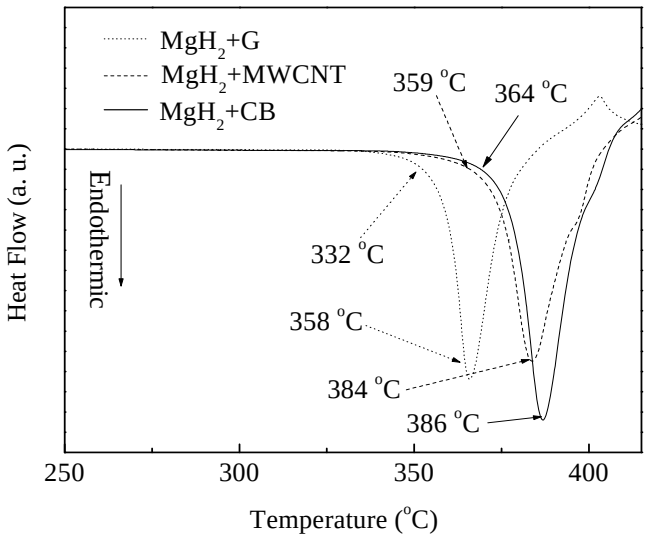

Fig. 7.8. DSC curves of the rehydrogenated composites.

The hydrogen desorption curve of the rehydrogenated composites is shown in Fig. 7.9. Among the three carbon allotropes, graphite shows a pronounced catalytic effect upon hydrogen desorption. MgH_2 + G composite shows the fastest desorption kinetics, with a complete release within 7 minutes, followed by MgH_2 + CB in 9 minutes, and then MgH_2 + MWCNT in 11 minutes. This is consistent with the DSC results. Detailed discussion of the enhancement is in Section 7.4.

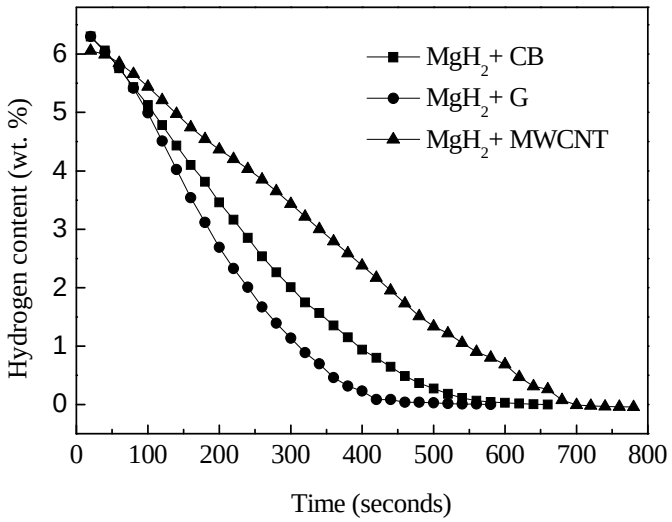

Fig. 7.9. Hydrogen desorption kinetics of the rehydrogenated composites at 350 ^{o}C.

7.4 Catalytic effect of graphite

As presented above, graphite shows a dramatic catalytic effect on the hydrogen absorption (Fig. 7.6) and desorption (Fig. 7.9) kinetics of magnesium. The possible reasons are discussed below.

7.4.1 Particles

The average particle sizes of the rehydrogenated composites, as evaluated from the Nano ZS particle size analyser, are listed in Table 7.3. Compared with the particle sizes of the as-prepared composites listed in Table 7.2, there is an obvious increase in particle size for all composites. For MgH_2 + G, the particle size increased from 503 nm to 573 nm after rehydrogenation. The concurrence of particle growth and fast hydrogen cycling properties seems contradictory to the fact that small particle size contributes to hydrogen uptake and release (Huot et al. 1999 and Schimmel et al. 2005). Therefore,

there are some other factors that can account for the improvement in hydrogen cycling, which is apparently related to the presence of graphite.

Table 7.3 Average particle sizes of the rehydrogenated composites.

Sample name	Average particle size (nm)
MgH_2+CB (rehydrogenated)	724
MgH_2+G (rehydrogenated)	573
MgH_2+MWCNT (rehydrogenated)	741

The SEM images of the rehydrogenated composites show uniformly and loosely dispersed particles (Fig. 7.10 (a), (c) and (e)), in contrast with the agglomeration in the as-prepared composites (Fig. 7.2 (b), (e) and (h)). Obviously, the agglomerates have cracked and individual particles have grown during the hydrogen cycling. This is consistent with the results listed in Table 7.3. The weight percentage of carbon detected by EDS was more than 20 %, which means that most of the carbon was still accumulated on the surfaces, and this, in turn, can reduce the adhesion and agglomeration of magnesium hydride particles.

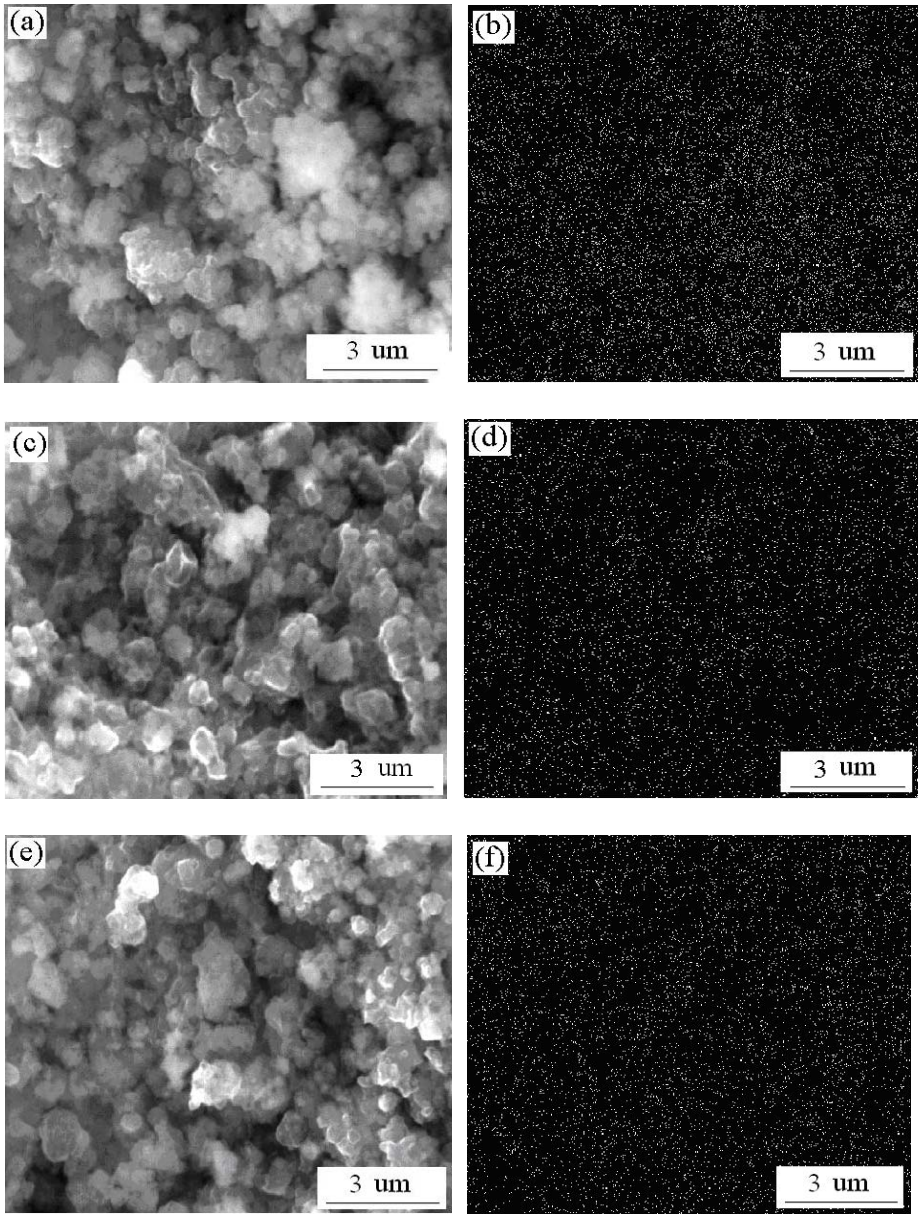

Fig. 7.10. SEM images of the rehydrogenated composites and the associated EDS maps of carbon: (a) MgH_2 + CB, (b) distribution of CB, (c) MgH_2 + G, (d) distribution of G, (e) MgH_2 + MWCNT, and (f) distribution of MWCNT.

7.4.2 Impact of heat treatment

There is an obvious structural difference between the as-prepared MgH_2 + G composite (Fig. 7.1) and the rehydrogenated one (Fig. 7.7), since the defects and microstresses

existing in the as-prepared composite were eliminated after hydrogen cycling. The influence of structural evolution on the thermal properties of the composite was tentatively clarified through DSC measurements (Fig. 7.11). The as-prepared MgH_2+G composite was heated to 300 ^oC and held at this temperature for two hours. Decomposition will not occur at this temperature, but the heat treatment can eliminate some microstresses and defects in the composites, as can be deduced from the XRD patterns (inset in Fig. 7.11). After the temperature was cooled down to 50 ºC, a normal scan to 500 ºC at heating rate of 6 ºC/min was conducted. The DSC curve reveals that the endothermic peak had shifted to higher temperature from 367 ^oC to 399 ^oC for γ-MgH_2, and 395 ^oC to 417 ^oC for β-MgH_2. It is clear that the decomposition was postponed after the composite was heat treated. During hydrogen cycling, there are hydrogen desorption and absorption processes taking place in addition to the heat transmission. Presumably, the hydrogen migration processes associated with graphite can shed light on the decrease of the decomposition temperature (Fig. 7.8).

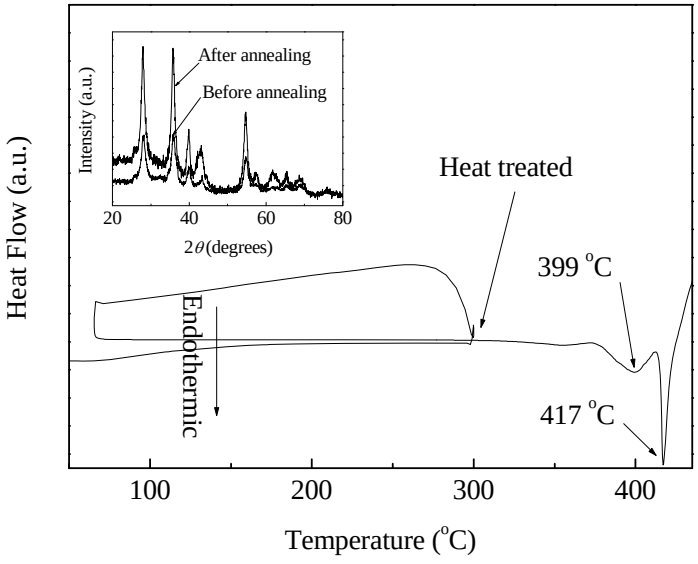

Fig. 7.11. DSC trace of the as-prepared MgH_2+G composite annealed at 300 ^oC for two hours. The inset shows the XRD patterns before and after annealing.

γ-MgH_2 phase is metastable in the ball-milled samples and can be removed when the samples are heated (Huot et al. 1999 and Bortz et al. 1999). It has been suggested that the presence of γ-MgH_2 accelerates the decomposition of β-MgH_2 (Gennari et al. 2001), since the conversion of γ-MgH_2 to Mg is accompanied by a much bigger volume contraction, which generates stress on the adjacent β-MgH_2 and facilitates the decomposition. However, there is no γ-MgH_2 in the rehydrogenated composites, as can be seen from the XRD patterns in Fig. 7.7. Consequently, this interpretation can be ruled out.

7.4.3 Structure of graphite

Imamura et al. (2002) suggested that it was the charge-transfer reactions occurring between graphite and magnesium that improved the hydrogen cycling properties of magnesium. In their experiments, they used organic additives to promote graphite cleavages along the graphite layers during ball milling. In our case, however, magnesium was milled with graphite in hydrogen without any protective additives. The layered structure of graphite experienced severe damage, and the graphite became amorphous, as can be inferred from the Raman spectra (Fig. 7.3). Therefore, the formation of magnesium hydride and the disruption of graphite occurred simultaneously. Presumably, charge-transfer reactions might occur in the composite before the graphite was totally destroyed. On the other hand, these charge-transfer sites may also form during hydrogen cycling. According to the observations, the maintenance of the layered structure seems to be unnecessary for exploiting the catalytic effect of graphite.

During hydrogen cycling, graphite may experience microstructural evolution due to heat treatment and hydrogen diffusion. To confirm this supposition, Raman spectra of pristine graphite, as well as graphite in the as-prepared and rehydrogenated MgH_2 + G composites were recorded (Fig. 7.12). There is almost no difference between the two spectra of graphite in the as-prepared and rehydrogenated MgH_2 + G composites. Therefore, graphite preserves its structure upon heating and hydrogen cycling.

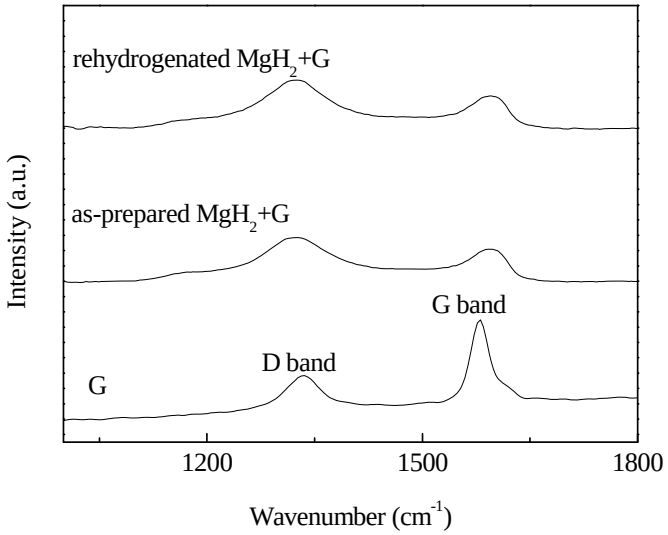

Fig. 7.12. Raman spectra of pristine graphite and of graphite in the as-prepared and rehydrogenated MgH_2 + G composites.

7.4.4 TEM analysis

The TEM image (Fig. 7.13, (a)) confirms that the as-prepared MgH_2 + G composite consists of nanostructural powder, comprising particle clumps with an average diameter of around 0.2~2 μm. Selected area electron diffraction (SAED) patterns for both the as-prepared and rehydrogenated samples are consistent with the XRD results, revealing MgH_2 and MgO phases. The dark-field images, Fig. 13(b)-(d), were obtained using a

small objective aperture size, as indicated by the circled regions on the associated SAED patterns in the respective insets. It was confirmed that the average diameters of the magnesium hydride nanocrystals produced by milling were predominately less than 30 nm (Fig. 7.13(b)), with coarser MgH_2 crystals (>50 nm average diameter) being formed after rehydrogenation (Fig. 7.13(c)). Dark-field imaging also revealed the presence of very fine amorphous or nanocrystalline MgO distributed uniformly within the nanostructural product. This distribution is clearly shown for the case of the rehydrogenated composite in Fig. 7.13(d), where very fine nanosized MgO phase is illuminated, tilted to exclude MgH_2 reflections. However, the TEM analysis gives no clues as to the mechanism of improved hydrogen desorption kinetics.

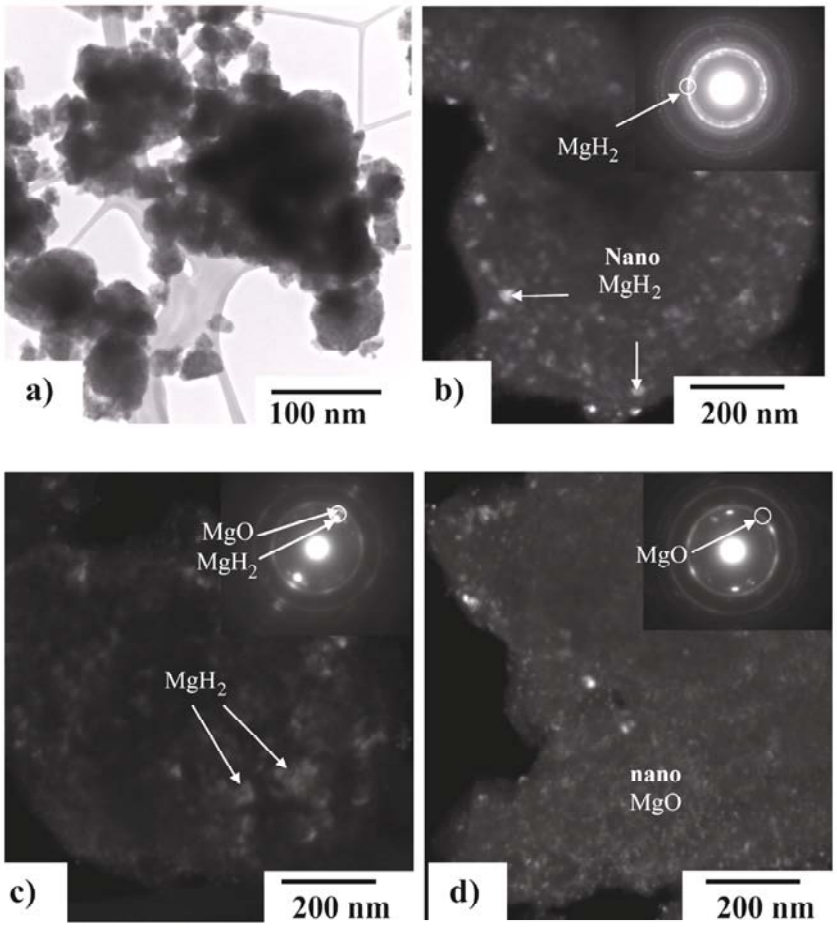

Fig. 7.13. TEM images of the as-prepared and rehydrogenated MgH_2 + G composite: (a) low magnification bright-field image of the as-prepared composite; (b) dark-field images of the as-prepared composite; (c) and (d) dark-field images of the rehydrogenated composite. (b)-(d) were obtained using the circled reflections in the insets, which contain the associated SAED patterns.

7.4.5 Interaction between graphite and hydrogen

Graphite itself has been intensively studied as a promising hydrogen storage medium (Orimo et al. 2001, Ichikawa et al. 2004, and Smolira et al. 2005). It was expected that some C-H bonding in the as-prepared and/or rehydrogenated MgH_2 + G composites would be observed. To confirm this hypothesis, the infrared (IR) absorbance was

recorded (Fig. 7.14), because this technique gives information on bonding configuration and hydrogenated bonds (Musumeci et al. 2000). The strong signals below 700 cm^{-1} originate from the equipment itself. There is no apparent difference in the IR spectra between the as-prepared and rehydrogenated composites. The main features of the spectra are associated with CO_2 and H_2O (Welham et al. 2003), and the characteristic stretching mode of the C-H bond at 2800-3000 cm^{-1} (Popescu et al. 2000) is not visible in the spectra.

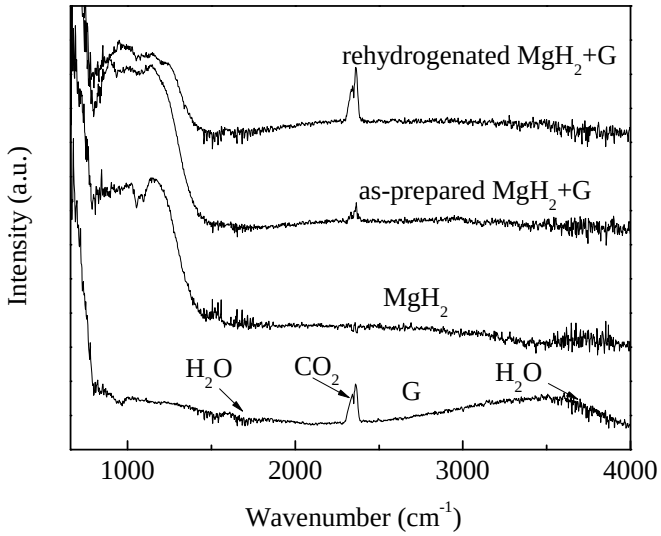

Fig. 7.14. Infrared spectra of the as-prepared MgH_2 and of the as-prepared and rehydrogenated MgH_2+G composites. An IR spectrum of ball-milled graphite is also shown here.

Graphite itself can store hydrogen via the formation of hydrogenated carbon clusters when it is milled in hydrogen and that the hydrogen can be released during heating (Chapter 8). Graphite ball milled via the same milling mode contains C_7H_2 and C_5H_4 clusters, as can be found from Table 8.3 in Chapter 8, and the trapped hydrogen can be released upon heating (as shown in Chapter 8, Fig. 8.12). The interaction between the

carbon and hydrogen atoms is probably not classical C-H bonding, as can be deduced from the IR spectra (as shown in Chapter 8, Fig. 8.13). Considering the common parts of the experiment, i.e. the same graphite and milling mode applied, there should be hydrogenated carbon clusters in the as-prepared MgH_2 + G composites, and the hydrogen trapped by the carbon clusters should be partially released upon heating. As a result, the hydrogenated carbon clusters would experience structural change. So far, there has been no report on the derivation of hydrogenated carbon clusters from carbon black and carbon nanotubes. Therefore, the formation of carbon clusters may explain the noticeable effect of graphite on the hydrogen cycling properties of magnesium.

There may be a reaction between graphite and magnesium during the hydrogen cycling. Although there are no magnesium and carbon compounds in the rehydrogenated composite, charge-transfer may occur if the heat treatment provides enough energy for this reaction. X-ray Photoelectron Spectroscopy (XPS) should be a powerful technique to validate this assumption.

7.4.6 Milling mode applied

It has to be mentioned that the milling mode applied in this experiment is very different from the mode associated with the most common vibrational (Spex) and planetary (Fritsch) mills, which generate high-energy impact forces and low-energy shearing forces concurrently and irregularly. In this experiment, a special milling mode was applied, in which the balls both rotate and oscillate around an equilibrium position at the bottom of the milling cylinder in a strong magnetic field. Consequently, a very low-energy shearing force dominates the milling process. It is well known that milling

conditions affect the properties of the product obtained (Huot et al. 2001), therefore, this low-energy shearing milling mode, in conjunction with graphite, probably contributes to the noticeable improvement in the desorption temperature.

7.5 Conclusions

1. Magnesium hydride was synthesized by reactive mechanical alloying. There are two kinds of MgH_2 in the as-prepared composites: β-MgH_2 and γ-MgH_2, with β-MgH_2 as the main component.

2. Among the carbon allotrope additives, graphite experienced the most structural transformation during ball milling.

3. All the carbon allotropes accumulated on the particle surfaces after ball milling and remained on the surface after cycling. This can prevent the particle growth of Mg and MgH_2.

4. Hydrogen cycling eliminates the γ-MgH_2 phase, resulting in only one endothermic peak in the DSC curves of the rehydrogenated composites. The rehydrogenated composites can store 6.2 wt. % hydrogen.

5. Neither the milling nor the hydrogen cycling process produces classical carbon hydrogen bonds.

6. Graphite shows dramatic catalytic behaviour towards hydrogen absorption. Full storage capacity could be reached within 1 minute in the composite containing graphite, in contrast to 3 minutes for MgH_2 + CB and MgH_2 + MWCNT.

7. Graphite shows extraordinary catalytic behaviour towards hydrogen desorption. The MgH_2 + G composite shows the fastest desorption kinetics, with a complete release within 7 minutes, followed by MgH_2 + CB and then MgH_2 + MWCNT.

8. As inferred from the Raman spectra, graphite maintains its structure upon hydrogen cycling.

9. The remarkable improvement in the hydrogen cycling properties of magnesium from graphite addition is probably due to two reasons: charge-transfer reactions between graphite and magnesium, and the existence of hydrogenated carbon clusters.

Chapter 8

Effects of milling conditions on the hydrogen storage properties of graphite

8.1 Introduction

As a very promising hydrogen storage candidate, graphite has attracted considerable research interest. However, all the results related to hydrogen storage properties are very scattered, ranging from almost 0 to 7 wt. % at room temperature (Kajiura et al. 2003, Orimo et al. 2001, Awasthi et al. 2002, Isobe et al. 2004, and Ichikawa et al. 2004). In most of the experiments, ball milling was applied to modify the graphitic structure, with the aim of enhancing the interaction between carbon and hydrogen. It is well known that the properties of milled products are very dependent on variations of milling parameters such as the milling atmosphere, the duration of milling, the materials of the milling media, and the energies applied (Huot et al. 2001). Therefore, the discrepancies in the hydrogen storage capacities of graphite are presumably due to variations in these milling parameters.

Generally, hydrogen atoms are trapped at two types of sites (Ichikawa et al. 2004, Atsumi and Tauchi 2003, and Orimo et al. 1999): 1) graphite inter-layers through solitary carbon dangling bonds, and 2) the edge surfaces of a crystallite through carbon dangling bonds. Mechanical milling contributes to the formation of dangling carbon bonds (Fukunaga et al. 1998 and Kanashenko et al. 1996). Consequently, hydrogen

storage capacities of graphite should be enhanced by ball milling. Additionally, hydrogen solubility, diffusivity, and desorption properties in graphite are defect related (Gotoh 1997 and Huang 1999), and these defects can also be generated through mechanical milling (Ong and Yang 2000 and Huang et al. 1999). So far, the hydrogen storage properties of graphite resulting from ball milling have been mainly investigated by using two types of ball mills: planetary (Fritsch) and vibrational (Spex), in which the movement of the grinding balls is very chaotic, which leads to the generation of a large spectrum of local milling energies and, in consequence, to a large spectrum of local absorption rates.

In order to control the milling energy, the movement of the grinding balls has to be controlled (Calka and Radlinski 1991). Uni-Ball-Mill 5 is a ball mill that allows the control of the milling energy via control of the movements of grinding balls. In experimental practice, low-energy shearing (Fig. 2.16) and high-energy impact (Fig. 2.17) can both be conveniently achieved. In the present work, these two milling modes (shearing and impact) were applied with the aim of clarifying the influence of the milling mode on the hydrogen storage capacity of graphite.

8.2 Synthesis of graphite hydrides

Graphite powder with a purity of 99.95 % was milled under hydrogen using the Uni-Ball-Mill 5. For comparison, graphite powder was milled under helium under the same milling conditions. For ease of description, the designations of all the samples obtained are listed in Table 8.1. SGH and IGH were annealed at 240 ^{o}C, 300 ^{o}C, 480 ^{o}C, and 600 ^{o}C, respectively.

Table 8.1 A list of sample names and synthesis methods.

Sample Name	Synthesis method
SGH	Hydrogen + shearing mode
IGH	Hydrogen + impact mode
SGHe	Helium + shearing mode
IGHe	Helium + impact mode

8.3 SGH samples

8.3.1 X-ray diffraction of SGH

Figure 8.1 shows the XRD pattern of the pristine graphite. A strong (002) diffraction peak is present. The XRD pattern in Fig. 8.2 shows that the (002) graphite reflection still exists after milling for 100 hours. The grain size is about 10 nm, which indicates that shearing mode is effective in the formation of a nanostructured layered structure. The broadening of the (002) reflection peak is probably due to the following causes: 1) the nanoscale grain size, and 2) microstresses induced during milling. The (002) reflection peak disappeared after SGH was annealed (Figs. 8.3-8.6), which means that the graphitic structure is metastable in SGH and the layered structure exfoliates upon heating. The SGH annealed at lower temperatures (240 ºC and 300 ºC) are predominantly nanostructured. The existence of austenite and magnetite (Fig. 8.6) indicates contamination from the milling media.

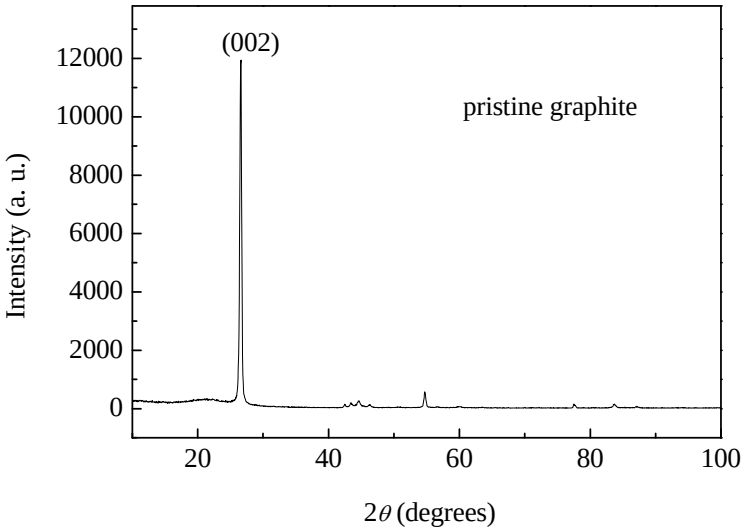

Fig. 8.1. XRD pattern obtained from the pristine graphite.

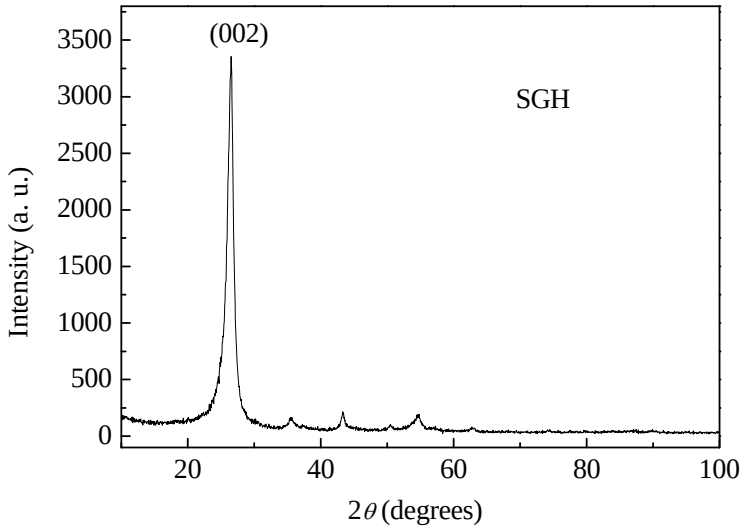

Fig. 8.2. XRD pattern obtained from the as-prepared SGH.

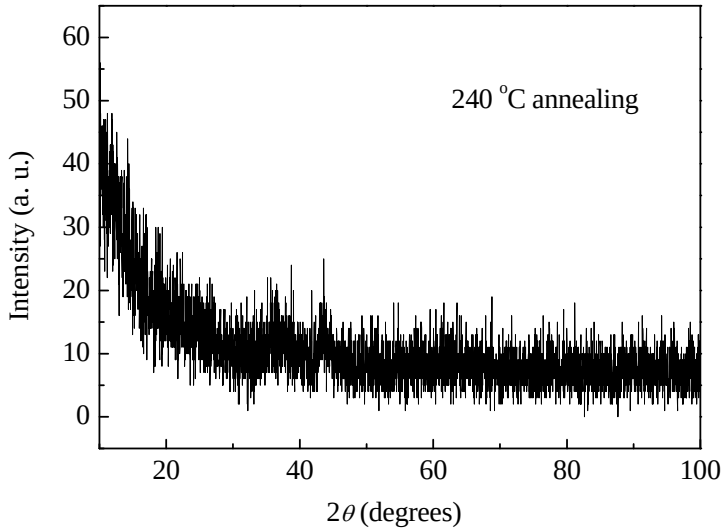

Fig. 8.3. XRD pattern of SGH annealed at 240 °C.

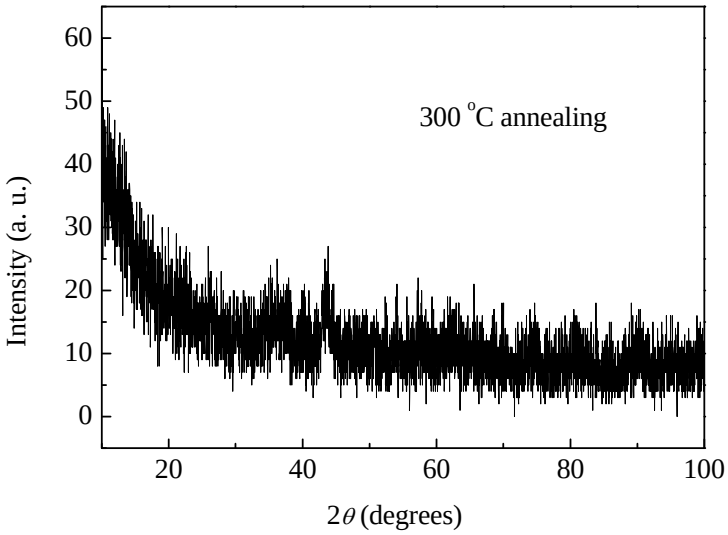

Fig. 8.4. XRD pattern of SGH annealed at 300 °C.

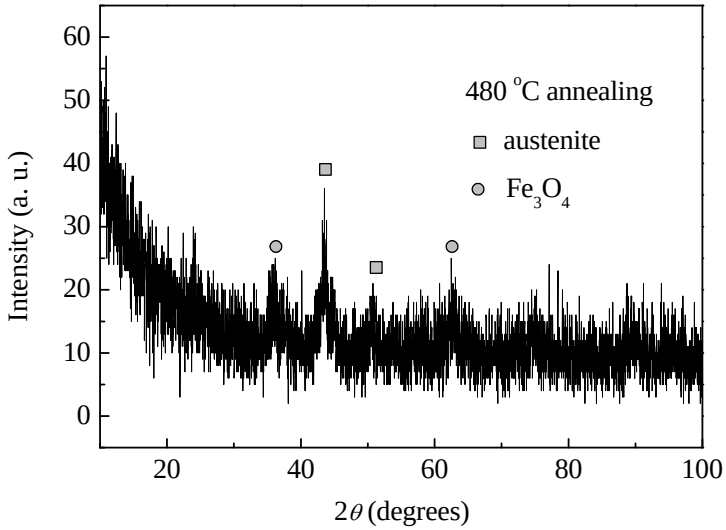

Fig. 8.5. XRD pattern of SGH annealed at 480 °C.

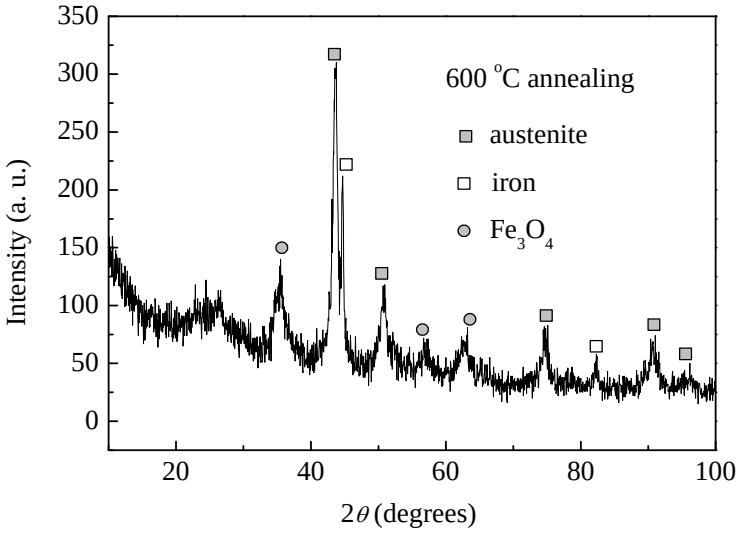

Fig. 8.6. XRD pattern of SGH annealed at 600 °C.

8.3.2 TEM analysis

The layered structure of pristine graphite can be seen under TEM (Fig. 8.7(a)), but after ball milling, the layered structure is not visible at higher magnification (Fig. 8.7(b)). The selected area electron diffraction (SAED) pattern shows that nanostructural particles exist in the sample. The emergence of spots in the SAED diffraction ring of the

sample annealed at 600 ^{o}C is associated with the formation of crystalline iron and iron oxides (Fig. 8.7 (c)). The SAED patterns of both the as-prepared and annealed samples are consistent with the XRD results.

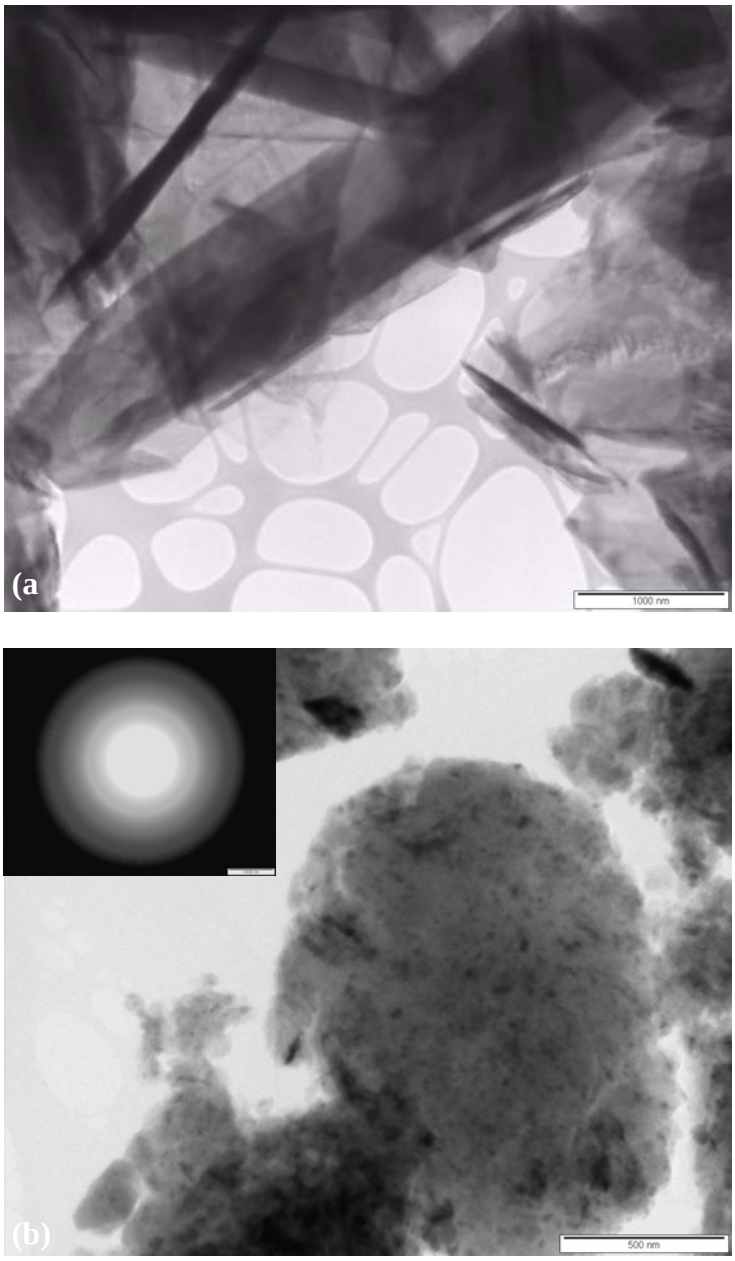

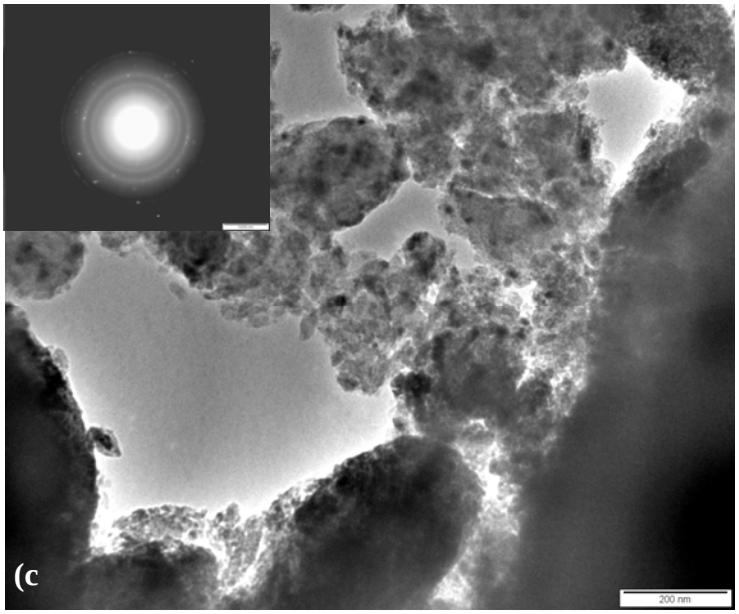

Fig. 8.7. TEM images of pristine graphite (a), as-prepared SGH (b), and SGH annealed at 600 ^{o}C (c). Insets in (b) and (c) show the associated SAED patterns.

8.4 X-ray diffraction of IGH

The (002) graphitic structure disappeared when graphite was milled using impact mode (Fig. 8.8), presumably due to the high degree of deformation caused by strong collisions between balls during milling. The high-energy impact mode led to some degree of iron contamination, as was revealed by the XRD peaks of iron carbide. Note that such peaks are not visible in the XRD pattern of the as-prepared SGH (Fig. 8.2). The annealed IGHs also became nanostructured (Fig. 8.9-11), which reveals similar structural evolution to that of the annealed SGHs.

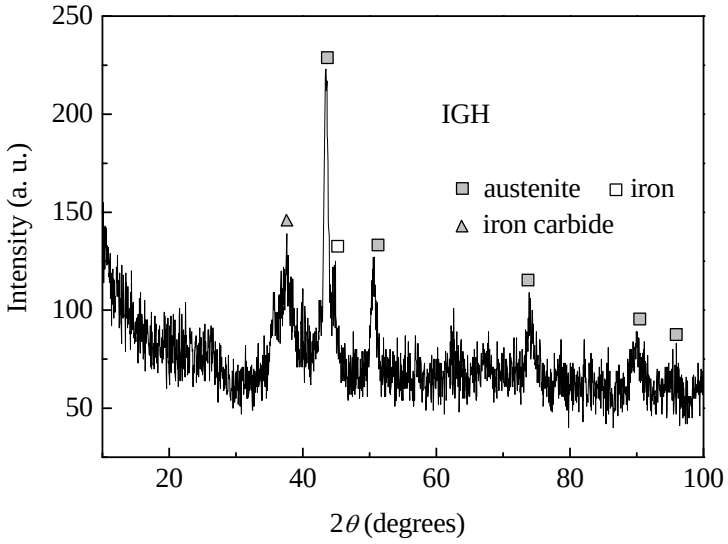

Fig. 8.8. XRD pattern obtained from IGH.

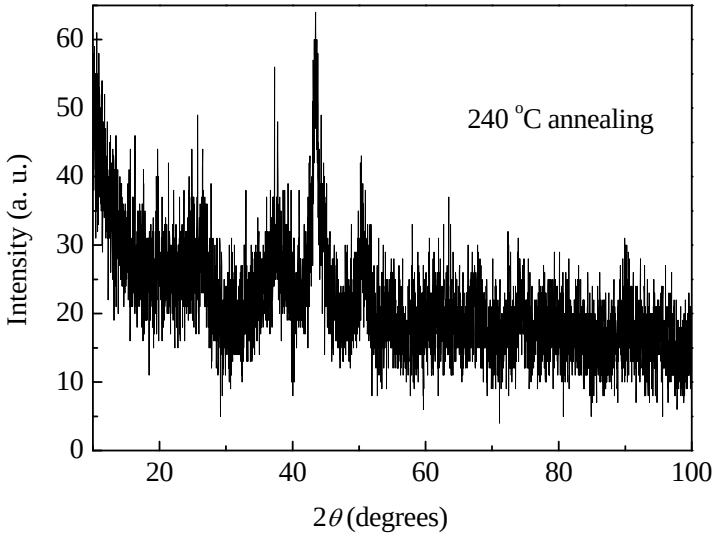

Fig. 8.9. XRD pattern of IGH annealed at 240 °C.

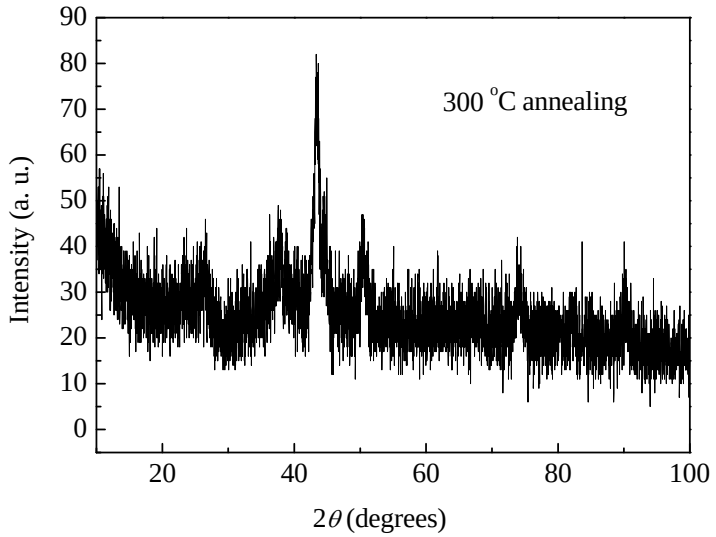

Fig. 8.10. XRD pattern of IGH annealed at 300 °C.

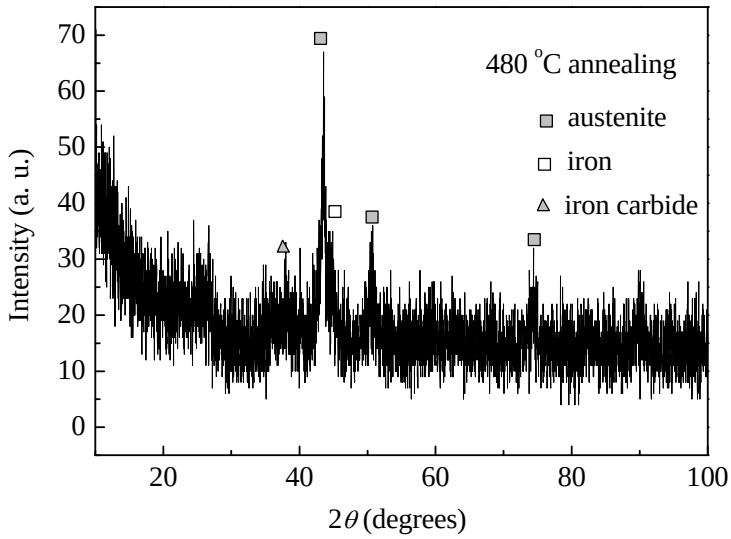

Fig. 8.11. XRD pattern of IGH annealed at 480 °C.

8.5 DSC traces

The DSC traces (Fig. 8.12) illustrate the distinctive thermal properties of the IGH and SGH. There are a series of small exothermic-like peaks in the DSC trace of IGH, while only two relatively large peaks and another small peak are found for SGH. Two small peaks were enlarged for further study (insets in Fig. 8.12). They are each revealed as one small endothermic peak closely followed by one large exothermic peak. The

possible origins of the peaks will be discussed in section 8.8.

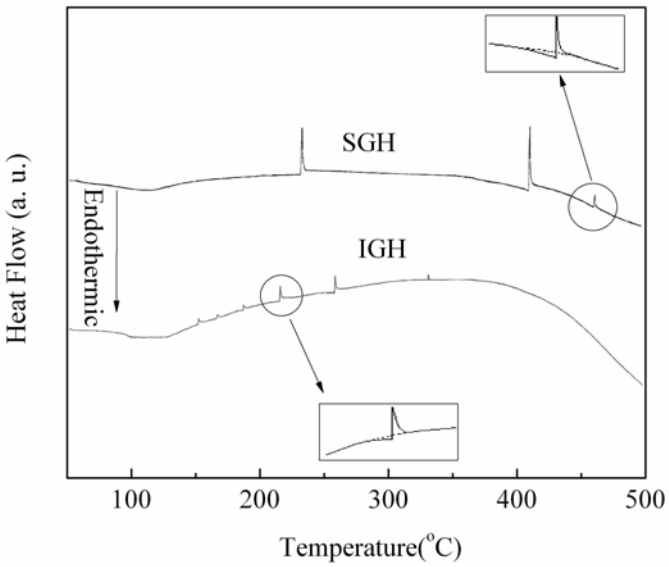

Fig. 8.12. DSC traces of SGH and IGH. The insets show enlargements of selected peaks.

Fig. 8.13 shows DSC traces obtained from the as-prepared graphite in helium. The purpose of this experiment was to investigate thermal effects due to the structural evolution of ball-milled graphite and to distinguish these effects from effects due to carbon-hydrogen interaction. There is no clear heat absorption or desorption for either sample. Since nanostructural graphite recrystallizes above 800 ^{o}C (Orimo et al. 2001), the effect of different milling modes on the structural evolution presumably can not be displayed at the temperature range applied in this experiment. Taking into account the different milling atmospheres, the series of endothermic and exothermic-like peaks obtained from SGH and IGH (Fig. 8.12) are due to the interaction between carbon and hydrogen, since all the other milling conditions remained the same.

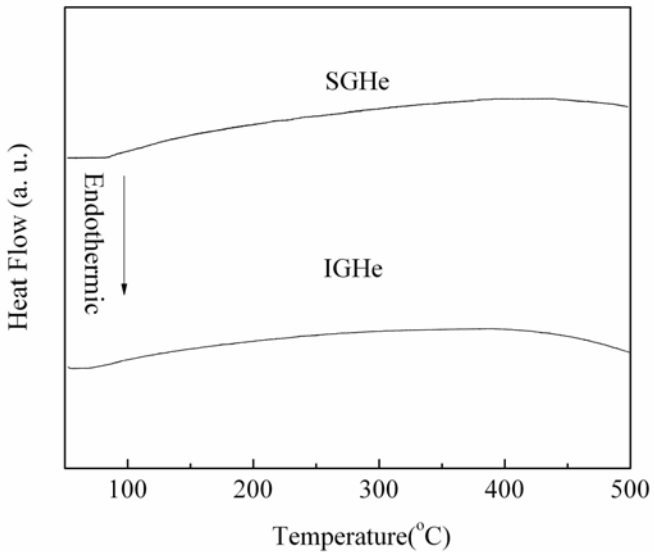

Fig. 8.13. DSC traces of SGHe and IGHe.

8.6 Hydrogen storage capacities

The CHN analysis (Table 8.2) showed that the hydrogen content reached 0.613 wt. % and 2.718 wt. % for the SGH and IGH samples, respectively. From the applications point of view, the high-energy impact mode is more favourable. It is well known that carbon dangling bonds are defect related (Fukunaga et al. 1998 and Kanashenko et al. 1996). High-energy impact in this experiment led to more defects than with low-energy shearing, and consequently, impact mode improves the hydrogen storage capacity. After the above DSC experiment, there was about 0.30 wt. % and 2.34 wt. % of hydrogen left in the SGH and IGH samples, respectively. These data imply that in IGH samples, the interaction between carbon and hydrogen is generally stronger than for SGH.

Table 8.2 Hydrogen content in SGH, IGH, and corresponding DSC treated samples.

Sample	As-prepared	After DSC
SGH	0.613 wt. %	0.30 wt. %
IGH	2.718 wt. %	2.34 wt. %

8.7 Compositions

The possible compositions of the as-prepared samples were investigated through laser desorption time-of-flight mass spectrometry (LTOF MS). The results revealed a variety of bare carbon clusters, as well as hydrogenated carbon clusters. The likely hydrogenated carbon clusters are shown in Table 8.3. The formation of hydrogenated carbon clusters can be associated with the milling mode, with impact leading to six types of clusters, and shearing resulting in only two.

Table 8.3 Possible hydrogenated carbon clusters observed in IGH and SGH.

C_nH_x in IGH	C_nH_x in SGH
C_5H_4	C_5H_4
C_7H_1	
C_7H_2	C_7H_2
C_7H_3	
C_8H_1	
C_8H_3	

In the light of the compositions listed in Table 8.3, the exothermic-like peaks can be interpreted. As can be seen in the insets of Fig. 8.12, the small peaks actually are each

an endothermic peak followed by an exothermic peak, which is presumably due to hydrogen desorption from hydrogenated carbon clusters and the succeeding carbon atom re-arrangement, leading to the formation of bigger carbon clusters (Calka et al. 1996). There are six types of hydrogenated carbon clusters in the IGH, and the desorption temperatures are different, as can be seen from the different positions of the small peaks. On the contrary, only two hydrogenated carbon clusters exist in the SGH, and as a result, only two large peaks and another small peak are visible.

Graphite itself has been intensively studied as a very promising hydrogen storage medium. Therefore, it was expected to observe some C-H bonding in the as-prepared samples. Since infrared can give information on bonding configuration and on hydrogenated bonds (Musumeci et al. 2000), infrared absorbance (IR) of the IGH and SGH were recorded (Fig. 8.14). The strong signal below 700 cm^{-1} originates from the equipment itself. The main features of the spectra are associated with CO_2 and H_2O (Welham et al. 2003), and the characteristic stretching mode of the C-H bond at 2800-3000 cm^{-1} is not visible in the spectra (Popescu et al. 2000). Considering the observation of hydrogenated carbon clusters in the IGH and SGH (Table 8.3), the correlation between carbon and hydrogen in the clusters is presumably not classical C-H bonding. The molecular formulas derived from the mass spectrometry also give a clue, since they are very dissimilar to classical hydrocarbons. For IGH, there is also a broad band at around 1250 cm^{-1}, which at this stage is difficult to explain.

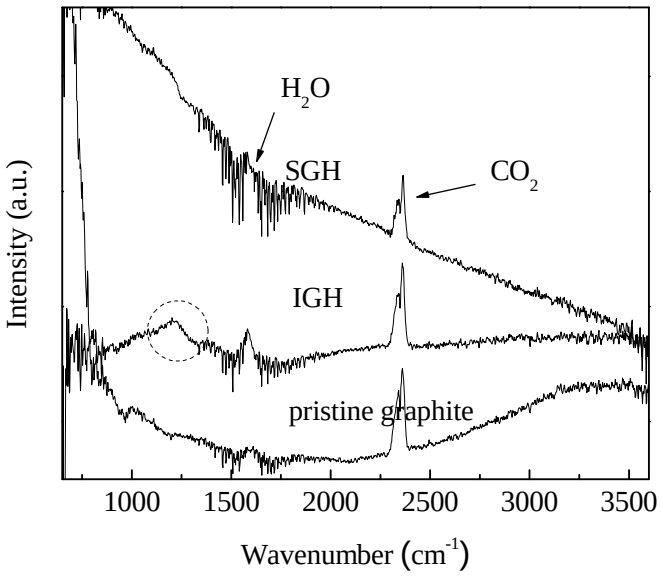

Fig. 8.14. Infrared spectra of SGH, IGH, and pristine graphite. The dashed circle indicates an unidentified peak in the IGH spectrum.

8.8 Conclusions

Different milling modes lead to dissimilar amounts of hydrogen trapped by graphite. The high-energy impact mode resulted in more hydrogen trapped by graphite than with low-energy shearing. Additionally, the formation of hydrogenated carbon clusters also depends on the milling mode applied, with the sample obtained through the high-energy mode consisting of a variety of carbon clusters, in contrast to only two existing in the sample obtained through the low-energy mode. The interaction between carbon and hydrogen seems not to be classical C-H bonding, on the basis of the IR results.

The exothermic-like peaks in the DSC curves of the as-prepared samples actually are each a small endothermic peak closely followed by a large exothermic one, which is presumably due to hydrogen desorption and subsequent re-arrangement of carbon atoms, respectively.

Chapter 9

Studies of the hydrogen storage properties of boron

9.1 Introduction

Recently, elements with small atomic numbers, such as lithium and boron, have attracted tremendous attention because they are essential elements in some very promising hydrogen storage materials, such as $LiAlH_4$ and $LiBH_4$ (Fakioglu et al. 2004 and Hagemann et al. 2004). Apart from the hydrides, nanostructural forms of boron nitride, such as nanocapsules, nanotubes, nanocages, nanoparticles, and nanoclusters, have also been studied and are expected to appear in prospective applications (Oku et al. 2001 and 2002). There are not many reports about boron itself being used to store hydrogen. Wang et al. (2003b) observed that 2.3 wt. % hydrogen could be trapped in ball-milled amorphous boron. They suggested that there are three types of B-H interaction, i.e. physisorbed H_2, B-H terminal bonds, and B-H-B bridge bonds. The bridge bonds constituted a smaller percentage and decomposed at lower temperature compared with the terminal bonds.

Since B-H terminal bonds and B-H-B bridge bonds make different contributions to the release of hydrogen trapped during ball milling, the properties of the as-prepared samples can be adjusted by modifying these two bonds. In this work, we used two ball-milling modes, a low-energy shearing mode (Fig. 2. 16) and a high-energy impact mode (Fig. 2.17), with the aim of studying their effects on the hydrogen storage properties of boron.

9.2 Synthesis of boron hydrides

Boron powder with a purity of 99 % was milled under hydrogen in a magneto-mill, the Uni-Ball-Mill 5. For comparison, boron powder was milled under helium under the same milling conditions. For ease of description, the designations applied to all the samples obtained are listed in Table 9.1.

Table 9.1 A list of sample names and synthesis methods.

Sample Name	Synthesis method
SBH	Hydrogen + shearing mode
IBH	Hydrogen + impact mode
SBHe	Helium + shearing mode
IBHe	Helium + impact mode

9.3 DSC traces

DSC traces of the fresh, as-prepared SBH samples are shown in Fig. 9.1. Apart from three major endothermic peaks situated at 105 ºC, 150 ºC, and 170 ºC, many small endothermic peaks were observed in the range of 190 ºC - 350 ºC. A descending trend at higher temperature was also observed. In the case of IBH, two big endothermic peaks are visible, with one at 147 ºC and the other at 402 ºC (Fig. 9.2). In contrast to the SBH sample, there are several exothermic-like peaks between these two large endothermic peaks. Major endothermic peaks are not visible in the second run curve for either sample. This is believed to be associated with the hydrogen desorption occurring in the first run, which can be corroborated by CHN analysis (Table 9.2). Also, all the small

endothermic peaks (SBH) and exothermic peaks (IBH) disappeared in the second run. The possible reasons are discussed later in this section.

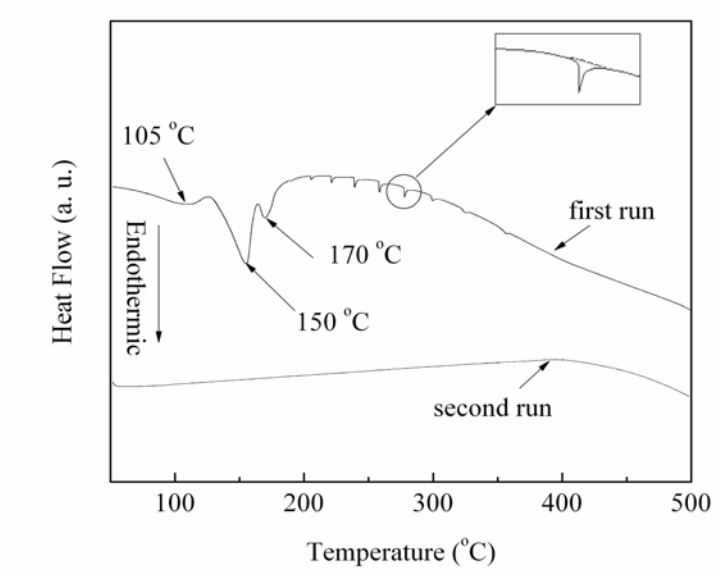

Fig. 9.1. DSC traces of the fresh, as-prepared SBH.

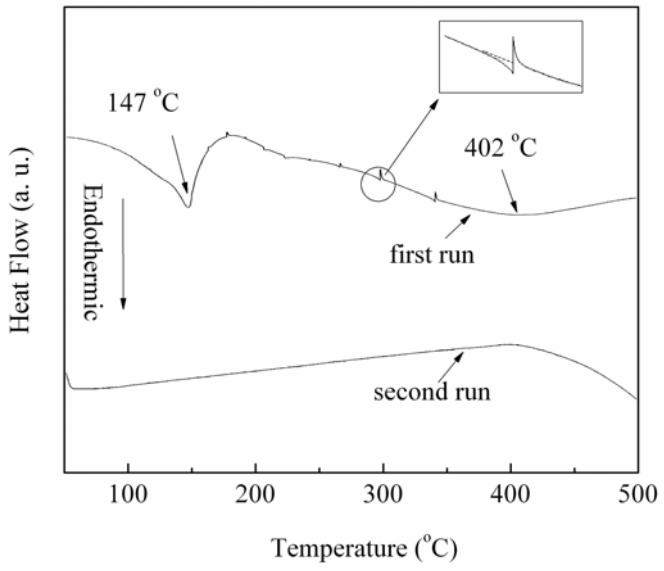

Fig. 9.2. DSC traces of the fresh, as-prepared IBH.

Figures 9.3 and 9.4 show DSC traces obtained from the boron milled in helium. The purpose of this experiment was to investigate thermal effects due to recrystallization of

ball-milled boron and distinguish these effects from effects due to the interaction between boron and hydrogen. Since the reaction between boron and iron from the steel materials is negligible, all the thermal effects are considered to be associated with the structural evolution of boron upon heating. There is no clear heat absorption or desorption in the case of the SBHe sample (Fig. 9.3). The second run curve is very similar to the first run, which means that the first run heat treatment did not alter the properties of the as-milled sample. There is an exothermic peak at around 475 ^{o}C for the IBHe sample in the second run curve (Fig. 9.4), which at this stage is difficult to explain. For the first run, there is a detectable difference between the DSC curves of SBHe and IBHe, which is presumably associated with the different milling modes.

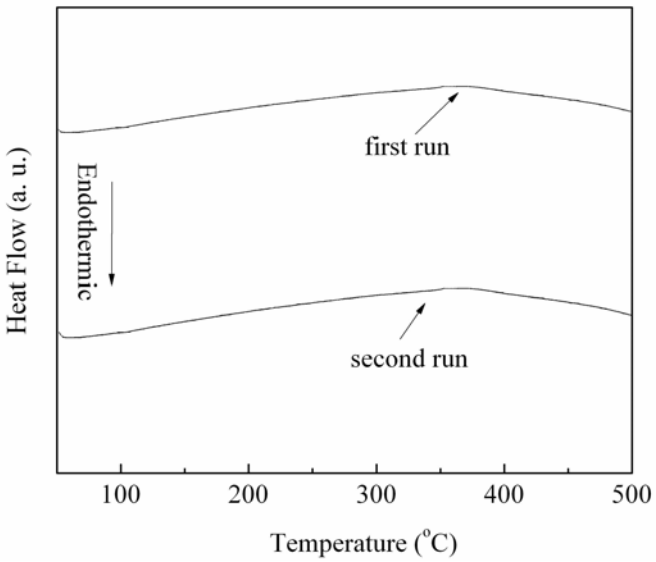

Fig. 9.3. DSC traces of the fresh, as-prepared SBHe.

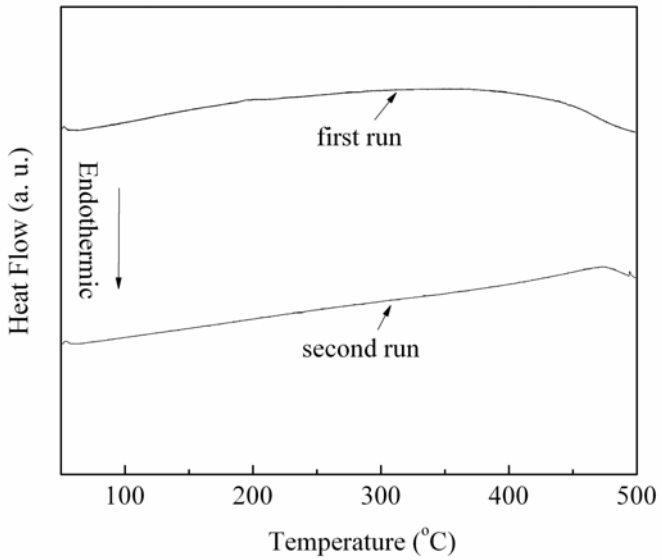

Fig. 9.4. DSC traces of the fresh, as-prepared IBHe.

Taking into account the different milling atmospheres, the series of endothermic and exothermic-like peaks obtained from fresh SBH (Fig. 9.1) and IBH (Fig. 9.2) are due to the interaction between boron and hydrogen, since all the other milling conditions remained the same. It is well known that boron is the only element other than carbon that can build molecules of unlimited size, i.e. boron clusters, and that it can form various types of polyhedral borane by covalent bonding (Grimes 2004). Chapter 8 shows that graphite forms a variety of hydrogenated carbon clusters after milling in hydrogen. The observed small peaks in the DSC curves (Fig. 8.12) of graphite that had been ball milled through impact and shearing are actually endothermic peaks followed by exothermic peaks. This is believed to be associated with hydrogen desorption from hydrogenated carbon clusters and subsequent re-arrangement of carbon atoms.

As can be seen in the inset (Fig. 9.2), the small exothermic-like peak actually is also an endothermic peak directly followed by an exothermic peak. The behavior is due to the hydrogen desorption from hydrogenated boron clusters, which is an endothermic effect,

and subsequent boron atom re-arrangement, which is an exothermic effect. There are many small similar peaks in the DSC curve of the graphite ball milled in hydrogen using impact mode (i.e. IGH, as shown in Chapter 8, Fig. 8.12), and they are related to the hydrogenated carbon clusters formed (in Chapter 8, Table 8.3) during ball milling. Presumably, there are also several types of hydrogenated boron clusters formed during ball milling.

On the other hand, the small endothermic peak enlarged in Fig. 9.1 shows an endothermic effect only, which is attributable to the hydrogen desorption. Therefore, for SBH there is no obvious subsequent boron atom re-arrangement. This difference probably originates from the milling mode. The high-energy impact mode leads to the formation of highly disordered atomic arrangements, which results in evident exothermic effects due to the microstructural evolution during heating. In contrast, the low-energy shearing mode results in fewer defects, and there is no apparent atomic re-arrangement during heating.

But why are there exothermic peaks following endothermic peaks for graphite milled using low-energy shearing mode (i.e. SGH, as shown in Chapter 8, Fig. 8.12)? The structural differences between graphite and boron can shed light on this. Compared with boron, the graphitic structure of graphite is much more vulnerable during ball milling. As a result, there are larger amounts of disordered carbon atoms to be rearranged in SGH than disordered boron atoms in SBH.

9.4 Hydrogen storage capacities

The hydrogen contents of samples were determined through CHN analysis, and the results are listed in Table 9.2. It was found that 2.05 wt. % hydrogen was trapped in the as-prepared SBH, while 2.93 wt. % hydrogen was trapped in the as-prepared IBH. This indicates that impact mode contributes more to hydrogen absorption than shearing mode. However, after the samples were heated up to 500 ^{o}C, 1.24 wt. % hydrogen was still present in the SBH, in contrast with only 0.5 wt. % for IBH. These data imply that the ratio of strong B-H bonds to weak B-H bonds in SBH is much higher than in IBH.

Table 9.2 Hydrogen content in IBH, SGH, and the corresponding DSC treated samples.

Sample	As-milled	After DSC
IBH	2.93 wt. %	0.5 wt. %
SBH	2.05 wt. %	1.24 wt. %

Wang et al. (2003a) found that the amount of hydrogen trapped by terminal bonds was approximately twice as great as that trapped by bridge bonds, with desorption occurring at around 450 ^{o}C and 200 ^{o}C, respectively. In their work, ball milling was carried out with a planetary ball mill (Fritsch 7) at 400 rpm, in which the movement of balls is quite chaotic, with shearing and impact occurring concurrently and irregularly. In this work, the effects attributed to shearing were separated from those attributed to impact by using the two respective milling modes. It is believed that the endothermic effect occurring around 150 ^{o}C is due to the breaking of B-H-B bridge bonds, while the other at 402 ^{o}C (for IBH) can be attributed to the breaking of B-H terminal bonds. For SBH, the descending trend in Fig. 9.1 is presumably associated with the breaking of B-H terminal bonds, which is postponed to a higher temperature.

The different types of DSC behavior, the amount of hydrogen trapped during milling, and the amount of residual hydrogen after heating are all related to the milling mode, more specifically, to the movement of the balls in the cylinders and the energy applied during ball milling. Impact mode is high-energy ball milling, in which the balls continuously collide with the walls of the cylinder, resulting in a high local temperature. In addition, impact generates more structural defects, which improves the diffusion rate and (together with temperature) improves capacity. In contrast, shearing mode is a low-energy type of ball milling, in which the balls roll along the walls, which acts to grind the powders in the cylinder. This mode does not favour the formation of structural defects to such a large degree as impact mode. Moreover, the local temperature is unable to rise as high as in the case of impact mode, which may also affect the reaction between boron and hydrogen.

The impact of the energy applied is also evident in the SEM images of the as-prepared samples. There are larger and denser agglomerations in boron powders milled using the high-energy impact mode, i.e. IBH (Fig. 9.5), while relatively small and uniform particles exist in the sample obtained using low-energy shearing mode, i.e. SBH (Fig. 9.6). Apparently, this is related to the energy applied during milling, with high energy impact leading to more agglomeration.

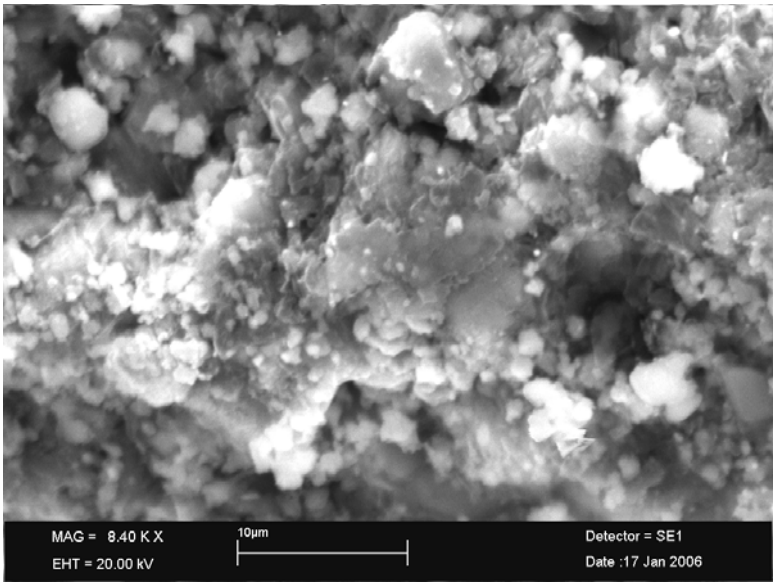

Fig. 9.5. SEM image of IBH.

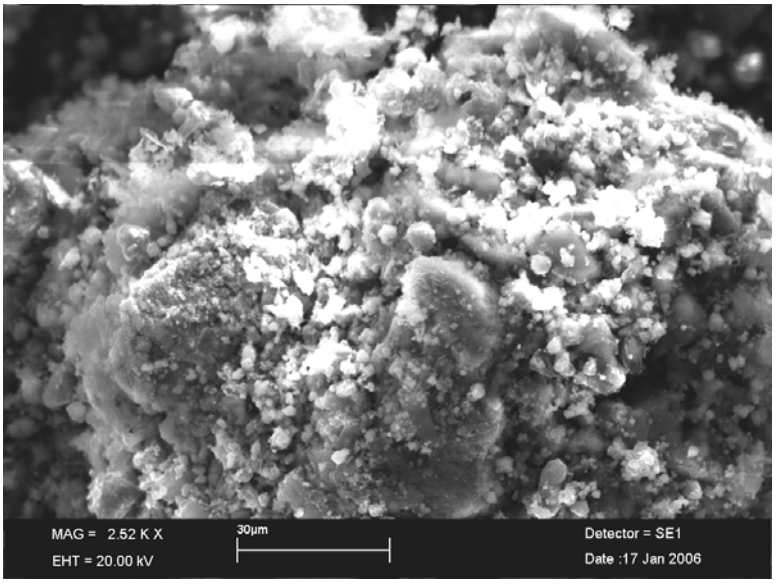

Fig. 9.6. SEM image of SBH.

9.5 DSC traces of aged sample

Figures 9.7 and 9.8 present the DSC traces of the SBH and IBH after two weeks aging in an ambient environment. These traces are quite different from those of the freshly

milled samples, which indicate that the milled samples had experienced structural evolution at room temperature. In the case of SBH (Fig. 9.7), all the small endothermic effects have vanished and a broad endothermic peak at 458 ^{o}C has appeared. In the case of IBH (Fig. 9.8), the endothermic peak at 147 ^{o}C in the fresh sample (Fig. 9.2) has split into three endothermic peaks, which are similar to those of the aged SBH. The broad peak at 402 ^{o}C obtained from the fresh sample was postponed to 485 ^{o}C. All the small exothermic-like peaks have also disappeared. Therefore, the hydrogenated boron clusters in the freshly milled samples are not chemically stable. All the endothermic peaks associated with hydrogen desorption disappeared in the second run for both samples.

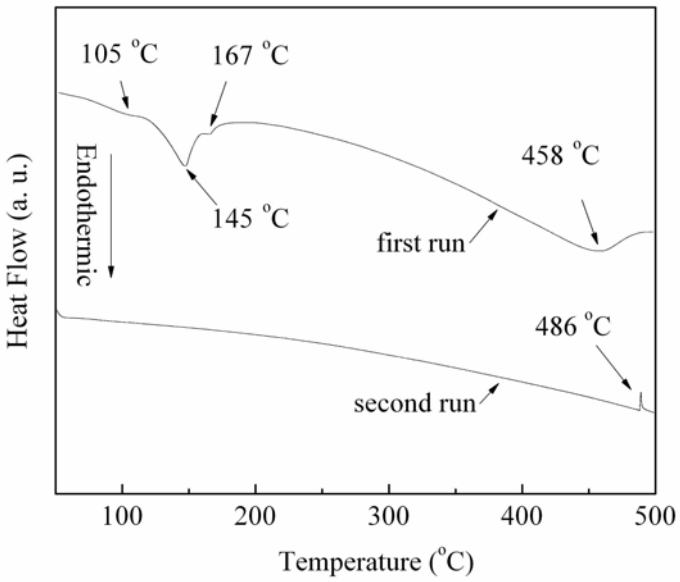

Fig. 9.7. DSC traces of the aged SBH.

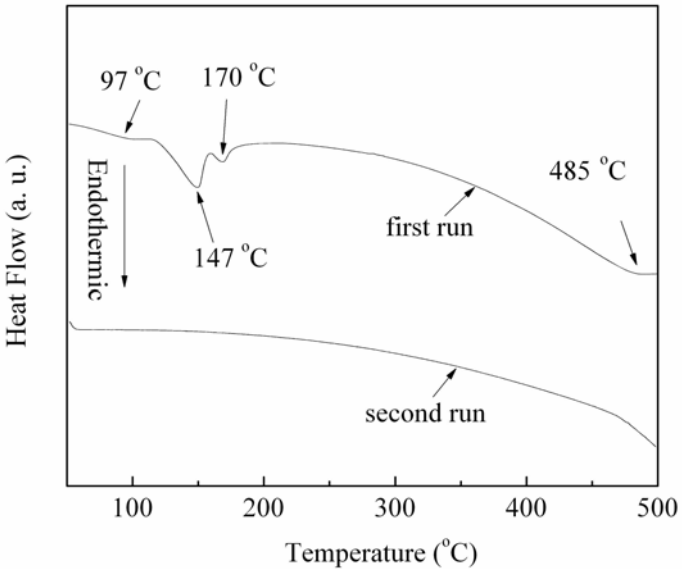

Fig. 9.8. DSC traces of the aged IBH.

9.6 Conclusions

On the basis of the above results one can conclude that different ball milling modes lead to dissimilar amounts of hydrogen being trapped by boron. Additionally, the interaction between boron and hydrogen is also different, with the low-energy shearing mode resulting in a higher percentage of strong B-H bonds, in contrast with the higher percentage of weak B-H bonds obtained through high-energy impact mode.

In the case of the samples obtained from shearing mode, there are many small endothermic peaks co-existing with bigger endothermic ones, which correspond to hydrogen desorption. Many small exothermic-like peaks, however, are visible for the sample obtained through impact mode, which is associated with hydrogen desorption and subsequent boron atom re-arrangement. For both cases, all these small peaks disappear after two weeks ageing.

Chapter 10

Summary

Experiments and results on the effects of catalysts and ball milling on the hydrogen storage properties of some promising candidate materials, such as Mg-based alloys, Mg, graphite, and boron, have been presented in the previous chapters. In brief, the findings can be summarized as follows:

10.1 $Mg_{1.9}Cu_{0.1}Ni_x$ (x = 1.8, 1.9, 2.0, and 2.1) alloys

1) $Mg_{1.9}Cu_{0.1}Ni_x$ (x = 1.8, 1.9, 2.0, and 2.1) alloys were obtained through mechanical alloying. XRD and TEM confirm that the alloys are predominately amorphous. The crystallization temperatures of the ball-milled alloys, the tendency towards forming Mg_2NiH_4, and the desorption temperatures of the hydrides are all related to the nickel content. The higher the Ni content in the alloy, the higher the temperature required for recrystallization into Mg_2Ni and $MgNi_2$, the more difficult the formation of Mg_2NiH_4, and the higher the desorption temperature. These correlations can be explained through the formation enthalpies of nickel monovacancies, which are 61.5 kJ/mol, 62.6 kJ/mol, 63.8 kJ/mol, and 64.9 kJ/mol, corresponding to nickel content x = 1.8, 1.9, 2.0, and 2.1.

2) Nickel helps increase the hydriding and dehydriding rates, and improve the reversibility and discharge capacity of $Mg_{1.9}Cu_{0.1}Ni_x$ (x = 1.8, 1.9, 2.0, and 2.1) alloy electrodes. The decay in discharge capacity decreases from 66.7 % to 47.2 %,

as the nickel content increases from 1.8 to 2.1. These enhancements are possibly due to the electrocatalytic behavior of Ni and the suppression of the formation of $Mg(OH)_2$ on the electrode surfaces.

10.2 Effects of catalysts on the hydrogen storage properties of Mg

1) Both iron oxides are completely reduced during the decomposition of the as-prepared $MgH_2 + Fe_2O_3$ and $MgH_2 + Fe_3O_4$ composites. The greater capacity loss of $MgH_2 + Fe_2O_3$ composite after rehydrogenation is due to the reduction reaction, since more Mg is consumed by reducing Fe_2O_3 than Fe_3O_4. The hydrogen absorption and desorption kinetics are very similar for both composites. This is possibly due to the reduction reaction, which eliminates the differences in the valence state of Fe in the oxides, and as a result, identical compositions and Fe-Mg interfaces are present in both composites.

2) There are two kinds of hydrides, β-MgH_2 and γ-MgH_2, in the ball-milled MgH_2 + CB (carbon black), MgH_2 + G (graphite), and MgH_2 + MWCNT (multiwalled carbon nanotube) composites. Hydrogen cycling eliminates the γ-MgH_2 phase. The rehydrogenated composites can store 6.2 wt. % hydrogen. Graphite shows dramatic catalytic behavior towards hydrogen absorption. Full capacity can be reached within one minute for MgH_2 + G, in contrast with 3 minutes for MgH_2 + CB and MgH_2 + MWCNT. MgH_2 + G shows the fastest desorption kinetics, with complete release within 7 minutes, in contrast with 9 minutes for MgH_2 + CB and 11 minutes for MgH_2 + MWCNT. The remarkable improvement in the hydrogen cycling properties of Mg from graphite addition is presumably due to the charge-transfer reaction

between graphite and magnesium and to the presence of hydrogenated carbon clusters.

10.3 Impacts of milling mode on hydrogen storage properties

1) High-energy impact and low-energy shearing modes have been applied to ball mill graphite in hydrogen. The graphite milled through different modes displays different thermal behavior under DSC measurements. The exothermic-like peaks in the DSC traces actually are each an endothermic peak followed by an exothermic peak, which is associated with hydrogen desorption and subsequent carbon atom re-arrangement. The compositions of the ball-milled graphite are correlated with the milling mode applied. There are six types of hydrogenated carbon clusters in the graphite milled under high-energy impact mode, compared with only two being present in the graphite milled under low-energy shearing mode. As a result, more hydrogen is stored using the high-energy impact mode.

2) Boron was ball milled in hydrogen using both the high-energy impact and the low-energy shearing mode. The high-energy impact mode led to the trapping of 2.93 wt. % hydrogen during milling, in contrast with 2.05 wt. % for the low-energy shearing mode. The proportion of the strong type of B-H bonds in boron milled under impact mode was lower than for the shearing mode. The different DSC behaviors observed were due to the milling energy applied. High-energy impact led to highly disordered atomic arrangements in the boron. Therefore, there are exothermic-like DSC peaks, which actually are each the combination of an endothermic peak due to hydrogen desorption and an exothermic peak due to subsequent boron atom re-arrangements.

No such peaks exist in the DSC trace of boron milled under low-energy shearing.

References

Abe T, Inoue S, Mu D, Hatano Y, and Watanabe K, 2003, J. Alloys Compd., vol. 349, p279.

Aceves S M, Berry G D, Martinez-Frias J, and Espinosa-Loza F, 2006, Int. J. Hydrogen Energy, vol. 31, p2274.

Ahn C C, Ye Y, Ratnakumar B V, Witham C, Bowman R C Jr., and Fultz B, 1998, Appl. Phys. Lett., vol. 73, p3378.

Andreasen A, Vegge T, and Pedersen A S, 2005, J. Phys. Chem. B, vol. 109, p3340.

Anton D L, 2003, J. Alloys Compd., vol. 356–357, p400.

Aoyagi H, Aoki K, and Masumoto T, 1995, J. Alloys Compd., vol. 231, p804.

Atsumi H and Tauchi K, 2003, J. Alloys Compd., vol. 356-357, p705.

Au M, 2005, Mater. Sci. Eng. B, vol. 117, p37.

Au M, Wu J, and Wang Q D, 1995, Int. J. Hydrogen Energy, vol. 20, p141.

Awasthi K, Kamalakaran R, Singh A K, and Srivastava O N, 2002, Int. J. Hydrogen Energy, vol. 27, p425.

Baer R, Zeiri Y, and Kosloff R, 1997, Phys. Rev. B, vol. 55, p952.

Bajuk A, Gluch K, and Michalak L, 2001, Rapid Commun. Mass Spectrom., vol. 15, pp2383.

Barkhordarian G, Klassen T, and Bormann R, 2003, Scripta Mater., vol. 49, p213.

Barkhordarian G, Klassen T, and Bormann R, 2004, J. Alloys Compd., vol. 364, p242.

Bloch J and Mintz M H, 1997, J. Alloys Compd., vol.253–254, p529.

Bobet J L, Castro F J, and Chevalier B, 2005, Scripta Mater., vol. 52, p33.

Bogdanovic B and Schwickardi M, 1997, J. Alloys Compd., vol. 253, p1.

Bogdanovic B, Felderhoff M, Kaskel S, Pommerin A, Sclichte K, and Schüth F, 2003, Adv. Mater., vol. 15, p1012.

Bortz M, Bertheville B, Böttger G, and Yvon K, 1999, J. Alloys Compd., vol. 282, p84.

Bösenberg U, Doppiu S, Mosegaard L, Barkhordarian G, Eigen N, Borgschulte A, Jensen T R, Cerenius Y, Gutfleisch O, Klassen T, Dornheim M, and Bormann R, 2007, Acta Mater., vol. 55, p3951.

Bououdina M, Enoki H, and Akiba E, 1998, J. Alloys Compd., vol. 281, p290.

Bououdina M, Grant D, and Walker G, 2006, Int. J. Hydrogen Energy, vol. 31, p177.

Bououdina M, Soubeyroux J L, and Fruchart D, 1997, Int. J. Hydrogen Energy, vol. 22, p329.

Bououdina M, Soubeyroux J L, de Rango P, and Fruchart D, 2000, Int. J. Hydrogen Energy, vol. 25, p1059.

Buschow K H J, 1981, J. Less-Common Met., vol. 79, p243.

Buschow K H J and Beekmans N M, 1980, Solid State Commun., vol. 35, p233.

Calka A and Radlinski A P, 1991, Mater. Sci. Eng. A, vol. 134, p1350.

Calka A, Nikolov J I, and Williams J S, 1996, Mater. Sci. Forum, vol. 225-227, p527.

Castro F J and Bobet J L, 2004, J. Alloys Compd., vol. 366, p303.

Chahine R and Bose T K, 1994, Int. J. Hydrogen Energy, vol. 19, p161.

Chambers A, Park C, Baker R T K, Rodriguez N M, 1998, J. Phys. Chem. B, vol. 102, p4253.

Charbonnier J, de Rango P, Fruchart D, Miraglia S, Pontonnier L, Rivoirard S, Skryabina N, and Vulliet P, 2004, J. Alloys Compd., vol. 383, p205.

Chen D, Chen L, Liu S, Ma C X, Chen D M, and Wang L B, 2004, J. Alloys Compd., vol. 372, p231.

Chen J, Bradhurst D H, Dou S X, and Liu H K, 1998, Proceedings of IMEA conference, p615.

Conte M, Iacobazzi A, Ronchetti M, and Vellone R, 2001, J. Power Sources, vol. 100, pp171.

Corre S, Bououdina M, Fruchart D, and Adachi G Y, 1998, J. Alloys Compd., vol. 275-277, p99.

Cui N and Luo J L, 1998, J. Alloys Compd., vol. 265, p305.

Cui N, Luo J L, and Chuang K T, 2000, J. Alloys Compd., vol. 302, p218.

Darnaudery J P, Pezat M, and Darriet B, 1983, J. Less-Commom Met., vol. 92, p199.

Dehouche Z, Djaozandry R, Huot J, Boily S, Goyette J, Bose T K and Schulz R, 2000, J. Alloys Compd., vol. 305, p264.

Dehouche Z, Goyette J, Bose T K, and Schulz R, 2003, Int. J. Hydrogen Energy, vol. 28, p983.

Dehouche Z, Klassen T, Oelerich W, Goyette J, Bose T K, and Schulz R, 2002, J. Alloys Compd., vol. 347, p319.

Digital Trends, 2005, accessed 6/06/2007, http://news.digitaltrends.com/news/story/8639/canons_fuel_cell_may_drive_portable_gear.

Dillon A C, Jones K M, Bekkedahl T A, Klang C H, Bethune D S, and Heben M J, 1997, Nature, vol. 386, p377.

Dinca M and Long J R, 2005, J. Am. Chem. Soc., vol. 127, p9376.

European Environment Agency, 2006, Annual European Community greenhouse gas inventory 1990-2004 and inventory report 2006, accessed 4/7/2007, http://reports.eea.europa.eu/technical_report_2006_6/en.

EvoBus GmBH, 2006, Detailed summary of achievements, Project of Clean Urban Transport for Europe, Germany.

ExxonMobil, 2006, Tommorrow's Energy: a perspective on Energy Trends, Greenhouse Gas emissions and Future Energy Options, accessed 7/02/2007, http://www.exxonmobil.com/Corporate/Files/Coporate/tommorrow_energy.pdf.

Fakioglu E, Yurum Y, and Veziroglu T N, 2004, Int. J. Hydrogen Energy, vol. 29, p1371.

Férey G, Latroche M, Serre C, Millange F, Loiseau T, and Percheron-Guégan A, 2003, Chem. Commun., vol. 24, pp2976.

Férey G, Mellot-Draznieks C, Serre C, Millange F, Dutour J, Surblé S, Margiolaki I, 2005, Science, vol. 309, p2040.

Ford Motor Company, 2007, accessed 6/06/2007, http://www.ford.com/en/vehicles/specialtyVehicles/environmental/fuelCell/default.htm.

Friedlmeier G and Groll M, 1997, J. Alloys Compd., vol. 253–254, p550.

Friedlmeier G, Manthey A, Wanner M, and Grollm M, 1995, J. Alloys Compd., vol. 231, p880.

Frost H, Düren T, and Snurr R Q, 2006, J. Phys. Chem. B, vol. 110, p9565.

Fukumoto Y, Miyamoto M, Matsuoka M, and Iwakura C, 1995, Electrochim. Acta., vol. 40, p845.

Fukunaga T, Nagano K, Mizutani U, Wakayama H, and Fukushima Y, 1998, J. Non-Cryst. Solids, vol. 232-234, p416.

Furuya Y, Hashishin T, Iwanaga H, Motojima S, and Hishikawa Y, 2004, Carbon, vol. 42, p331.

Garberoglio G, Skoulidas A I, and Johnson J K, 2005, J. Phys. Chem. B, vol. 109, p13094.

Gennari F C, Castro F J, and Urretavizcaya G, 2001, J. Alloys Compd., vol. 321, pp46.

Gleiter H, 2000, Acta Mater., vol. 48, pp1.

Goo N H and Lee K S, 2002, Int. J. Hydrogen Energy, vol. 27, p433.

Gotoh Y, 1997, J. Nucl. Mater., vol. 248, p46.

Green Car Congress, 2006, accessed 6/6/2007, http://www.greencarcongress.com/2006/03/bmw_to_display_.html.

Greene D L and Schafer A, Reducing Greenhouse Gas Emissions From U.S. transportation, accessed 1/6/2007, http://www.pewclimate.org/docUploads/ustransp.pdf.

Grimes R N, 2004, J. Chem. Educ., vol. 81, p657.

Grochala W and Edwards P P, 2004, Chem. Rev., vol. 104, p1283.

Gross K J, Thomas G J, and Jensen C M, 2002, J. Alloys Compd., vol. 330–332, p683.

Gross K, Chartouni D, Leroy E, Züttel A, and Schlapbach L, 1998, J. Alloys Compd., vol. 269, p259.

Hagemann H, Gomes S, Renaudin G, and Yvon K, 2004, J. Alloys Compd., vol. 363, p126.

Han S S, Lee H Y, Goo N H, Jeong W T, and Lee K S, 2002, J. Alloys Compd., vol. 330–332, p841.

Hanada N, Ichikawa T, and Fujii H, 2005, J. Alloys Compd., vol. 404–406, p716.

Hanada N, Ichikawa T, Orimo S, and Fujii H, 2004, J. Alloys Compd., vol. 366, p269.

Hettinger W, Michel F, Ott P, and Theissen F, 1996, Proceedings of the 11th world hydrogen energy conference, Stuttgart, Germany, p1135.

Hirscher M and Panella B, 2005, J. Alloys Compd., vol. 404–406, p399.

Hirscher M and Panella B, 2007, Scripta Mater., vol. 56, p809.

Holtz R L, 1996, Basic user's guide for NRL 6323 hydrogen storage system, Naval Research Laboratory, Washington DC.

Holtz R L, Imam M A, 1999, J. Mater. Sci., vol. 34, p2655.

Hou P X, Xu S T, Ying Z, Yang Q H, Liu C, and Cheng H M, 2003, Carbon vol. 41, p2471.

Huang J Y, 1999, Acta Mater., vol. 7, p1801.

Huang J Y, Yasuda H, and Mori H, 1999, Chem. Phys. Lett., vol. 303, p130.

Huot J, Liang G, and Schulz R, 2001, Appl. Phys. A, vol. 72, p187.

Huot J, Liang G, Boily S, Van Neste A, and Schulz R, 1999, J. Alloys Compd., vol. 293–295, p495.

Hythane, 2007, accessed 5/5/2007, http://www.hythane.com/.

Ichikawa T, Chen D M, Isobe S, Gomibuchi E, and Fujii H, 2004, Mater. Sci. Eng. B, vol. 108, p138.

Ikeda K, Orimo S, Züttel A, Schlapbach L, and Fujii H, 1998, J. Alloys Compd., vol. 280, p279.

Imamura H, Kusuhara M, Minami S, Matsumoto M, Masanari K, Sakata Y, Itoh K, and Fukunaga T, 2003, Acta Mater., vol. 51, p6407.

Imamura H, Masanari K, Kusuhara M, Katsumoto H, Sumi T, and Sakata Y, 2005, J. Alloys Compd., vol. 386, p211.

Imamura H, Tabata S, Shigetomi N, Takesue Y, and Sakata Y, 2002, J. Alloys Compd., vol. 330–332, p579.

Imamura H, Tabata S, Takesue Y, Sakata Y, and Kamazaki S, 2000, Int. J. Hydrogen Energy, vol. 25, p837.

Imamura H, Takesue Y, Akimoto T, and Tabata S, 1999, J. Alloys Compd., vol. 293–295, p564.

Inoue H, Iden H, Shin-ya R, Nohara S, and Iwakura C, 2004, J. Electrochem. Soc., vol. 151, ppA939.

Intergovernmental panel on climate change, 2007, Climate Change 2007: The Physical Science Basis, accessed 6/6/2007, www.ipcc.ch/SPM2feb07.pdf.

International Energy Agency, 2005, World Energy Outlook 2005, accessed 6/6/2007, http://www.iea.org//textbase/nppdf/free/2005/weo2005.pdf

Isobe S, Ichikawa T, Gottwald J I, Gomibuchi E, and Fujii H 2004, J. Phys. Chem. Solids, vol. 65, p535.

Iwakura C, Inoue H, Nohara S, Shin-ya R, Kurosaka S, and Miyanohara K, 2002, J. Alloys Compd., vol. 330-332, p636.

Iwakura C, Inoue H, Zhang S G, and Nohara S, 1998, J. Alloys Compd., vol. 270, p142.

Iwakura C, Shin-ya R, Miyanohara K, Nohara S, and Inoue H, 2001, Electrochem. Acta, vol. 46, p2781.

Janot R, Aymard L, Rougier A, Nazri G A, and Tarascon J M, 2004, J. Phys. Chem. Solids, vol. 65, p529.

Joubert J M, Latroche M, Cerny R, Bowman R C, Percheron-Guegan A, and Yvon K, 1999, J. Alloys Compd., vol. 293–295, p124.

Kajiura H, Kadono K, Tsutsui S, and Murakami Y, 2003, Appl. Phys. Lett., vol. 82, p1929.

Kanashenko S L, Gorodetsky A E, Chernikov V N, Markin A V, Zakharov A P, Doyle B L, and Wampler W R, 1996, J. Nucl. Mater., vol. 233-237, p1207.

Kastner J, Pichler T, and Kuzmany H, 1994, Chem. Phys. Lett., vol. 221, p53.

Klug H P and Alexander L E, 1974, X-ray Diffraction Procedures for Polycrystalline and Amorphous Materials, 2nd ed., John Wiley & Sons, New York.

Kohno T and Kanda M, 1997, J. Electrochem. Soc., vol. 144, p2384.

Kojima Y, Kawai Y, Haga T, Matsumoto M, and Koiwai A, 2007, J. Alloys Compd., vol. 441, p189.

Langmi H W and McGrady G S, 2007, Coord. Chem. Rev., vol. 251, p925.

Langmi H W, Book D, Walton A, Johnson S R, Al-Mamouri M M, Speight J D, Edwards P P, Harris I R, and Anderson P A, 2005, J. Alloys. Compd., vol. 404–406, p637.

L-B-Systemtechnik GmbH, 2003, Future world oil supply: International Summer School On the Politics and Economics of Renewable Energy at the University Salzburg, accessed 4/6/2007, http://www.energyshortage.com/e/documents/2003/Int.-Summer-School-Salzburg-2002.pdf.

Li L Q, Saita I, Saito K, and Akiyama T, 2002, Intermetallics, vol. 10, p927.

Li X, Zhu H, Ci L, Xu C, Mao Z, Wei B, Liang J and Wu D, 2001, Carbon, vol. 39, p2077.

Liang G, Boily S, Huot J, Van Neste A, and Schulz R, 1998, Mater. Sci. Forum, vol. 267–272, p1049.

Liang G, Huot J, Boily S, Van Neste A, and Schulz R, 1999, J. Alloys Compd., vol. 291, p295.

Liang G, Huot J, Boily S, Van Neste A, and Schulz R, 2000, J. Alloys Compd., vol. 297, p261.

Liao B, Lei Y Q, Chen L X, Lu G L, Pan H G, and Wang Q D, 2004, J. Alloys Compd., vol. 376, p186.

Lin X, Blake A J, Wilson C, Sun X Z, Champness N R, George M W, Hubberstey P, Mokaya R, and Schröder M, 2006, J. Am. Chem. Soc., vol. 128, p10745.

Lin X, Jia J, Zhao X, Thomas K M, Blake A J, Walker G S, Champness N R, Hubberstey P, and Schröder M, 2006, Angew. Chem., Int. Ed., vol. 45, p7358.

Liu C, Fan Y Y, Liu M, Cong H I, Cheng H M, and Dresselhaus M S, 1999, Science, vol. 286, p1127.

Liu H K, 2004, Encyclopedia of Nanosci. Nanotech., vol. 4. p775.

Lu D, Li W, Hu S, Xiao F, and Tang R, 2006, Int. J. Hydrogen Energy, vol. 31, p678.

Lu K, Luck R, and Predel B, 1994, Acta Metall. Mater. vol. 42, p2303.

Lueking A and Yang R T, 2002, J. Catal., vol. 206, p165.

Lukashev R V, Klyamkin S N, and Tarasov B P, 2006, Inorg. Mater., vol. 42, p726.

Luo J L and Cui N, 1998, J. Alloys Compd., vol. 264, p299.

Luo W F, 2004, J. Alloys Compd., vol. 381, p284.

Luo Y, Wang P, Ma L P, and Cheng H M, 2007, Scripta Mater., vol. 56, p765.

Ma T J, Hatano Y, Abe T, and Watanabe K, 2005, J. Alloys Comp., vol. 391, p313.

Massachusetts Institute of Technology, 2003, The Future of Nuclear Power: An interdisciplinary MIT study, accessed 7/6/2007, http://web.mit.edu/nuclearpower/pdf/nuclearpower-summary.pdf.

Miedema A R, 1979, Z. Metallkd., vol. 70, p345.

Miedema A R, 1992, Physica B, vol. 182, p1.

Montone A, Grbovic J, Bassetti A, Mirenghi L, Rotolo P, Bonetti E, Pasquini L, and Antisari M V, 2006, Int. J. Hydrogen Energy, vol. 31, p2088.

Musumeci P, Calcagno L, Makhtari A, Baeri P, Compagnini G, and Pirri C F, 2000, Nucl. Instr. Methods Phys. Res. B, vol. 166-167, p404.

National Renewable Energy Laboratory, 2004, FY2004 Annual Progress Report for the DOE Hydrogen Program, accessed 4/5/2007, http://www.hydrogen.energy.gov/annual_progress04_storage.html#carbon.

Nohara S, Fujita N, Zhang S G, Inoue H, and Iwakura C, 1998, J. Alloys Compd., vol. 267, p76.

Notten P H L, 1991, J. Electrochem. Soc., vol. 138, p1877.

Notten P H L and Hokkeling P, 1991, J. Electrochem. Soc., vol. 138, p1877.

Oelerich W, Klassen T, and Bormann R, 2001, J. Alloys Compd.,vol. 315, p237.

Oku T and Narita I, 2002, Physica B, vol. 323, p216.

Oku T, Kuno M, Kitahara H, and Narita I, 2001, Int. J. Inorg. Mater., vol. 3, p597.

Ong T S and Yang H, 2000, Carbon, vol. 38, p2077.

Orimo S and Fujii H, 2001, Appl. Phys. A, vol. 72, p167.

Orimo S, Fujii H, and Ikeda K, 1997, Acta Mater., vol. 45, p331.

Orimo S, Ikeda K, Fujii H, Fujikawa Y, Kitano Y, and Yamamoto K, 1997, Acta Mater., vol. 45, p2271.

Orimo S, Majer G, Fukunaga T, Züttel A, Schlapbach L, and Fujii H, 1999, Appl. Phys. Lett., vol. 75, pp3093.

Orimo S, Matsushima T, Fujii H, Fukunaga T, and Majer G, 2001, J. Appl. Phys., vol. 90, p1545.

Orimo S, Nakamori Y, Kitahara G, Miwa K, Ohba N, Towata S, and Züttel A, 2005, J. Alloys Compd., vol.404–406, p427.

Panella B and Hirscher M, 2005, Adv. Mater., vol. 17, p538.

Panella B, Hirscher M, and Roth S, 2005, Carbon, vol. 43, p2209.

Panella B, Hirscher M, Pütter H, and Müller U, 2006, Adv. Funct. Mat., vol. 16, p520.

Pasturel M, Bobet J L, and Chevalier B, 2003, J. Alloys Compd., vol. 356–357, p764.

Pedersen A S and Larsen B, 1993, Int. J. Hydrogen Energy, vol. 18, p279.

Pehr K, Burckhardt S, Koppi J, Korn T, and Partsch P, 2002, ATZ Auto Technol. J. vol. 104, p3.

Pelletier J F, Huot J, Sutton M, Schulz R, Sandy A R, Lurio L B, and Mochrie S G J, 2001, Phys. Rev. B, vol. 63, p052103.

Pierard N, Fonseca A, Colomer J F, Bossuot C, Benoit J M, Tendeloo G V, Pirard J P, and Nagy J B, 2004, Carbon, vol. 42, p1691.

Poirier E, Chahine R, Benard P, Cossement D, Lafi L, Melancon E, Bose T K, and Desilets S, 2004, Appl. Phys. A, vol. 79, p961.

Popescu B, Tagliaferro A, De Zan F, and Davis E A, 2000, J. Non-Cryst. Solids, vol. 266-269, p803.

Popov B N, Zheng G, and White R E, 1996, J. Appl. Electrochem., vol. 26, p603.

Reilly J J, Wiswall R H, 1974, Inorg. Chem., vol. 13, p218.

Ritschel M, Uhlemann M, Gutfleisch O, Leonhardt A, Graff A, Täschner Ch, and Fink J, 2002, Appl. Phys. Lett., vol. 80, p2985.

Rongeat C and Roué L, 2004, J. Power Sources, vol. 132, p302.

Rosi N L, Eckert J, Eddaoudi M, Vodak D T, Kim J, Keeffe M O, and Yaghi O M, 2003, Science, vol. 300, p1127.

Ross D K, 2006, Vacuum vol. 80, p1084.

Rowsell J L C, Millward A R, Park K S, and Yaghi O M, 2004, J. Am. Chem. Soc., vol. 126, p5666.

Ruggeri S, Lenain C, Roue L, Liang G X, Huot J, and Schulz R, 2002a, J. Alloys Compd., vol. 339, p195.

Ruggeri S, Roue L, Liang G X, Huot J, and Schulz R, 2002b, J. Alloys Compd., vol. 343, p170.

Sakintuna B, Lamari-Darkrim F, Hirscher M, 2007, Int. J. Hydrogen Energy, vol. 32, p1121.

Sandrock G, Gross K J, and Thomas G, 2002, J. Alloys Compd., vol. 339, p299.

Satyapal S, Petrovic J, Read C, Thomas G, and Ordaz G, 2007, Catal. Today, vol. 120, p246.

Satyapal S, Read C, Ordaz G, and Thomas G, 2006, 2006 Annual Merit Review Proceedings, accessed 4/6/2007, http://www.hydrogen.energy.gov/annual_review06_proceedings.html.

Schimmel H G, Johnson M R, Kearley G J, Ramirez-Cuesta A J, Huot J, and Mulder F M, 2005, J. Alloys Compd., vol. 393, p1.

Schimmel H G, Kearley G J, Nijkamp M G, Visser C T, de Jong K P, and Mulder F M, 2003, Chem. Eur. J., vol. 9, p4764.

Schimmel H G, Nijkamp M G, Kearly G J, Rivera A, de Jong K P, and Mulder F M 2004, Mater. Sci. Eng. B, vol. 108, p124.

Schlesinger H I and Brown H C, 1940, J. Am. Chem. Soc., vol. 62, p3429.

Scoop, 2007, EU endorses Hydrogen Combustion Engine, accessed 5/06/2007, http://www.scoop.co.nz/stories/WO0702/S00413.htm

Senoh H, Ueda M, Inoue H, Furukawa N, and Iwakura C, 1998, J. Alloys Compd., vol. 266, p111.

Shang C X and Guo Z X, 2004, J. Power Sources, vol. 129, p73.

Skripnyuk V M, Rabkin E, Estrin Y, and Lapovok R, 2004, Acta Mater., vol. 52, p405.

Smolira A, Szymanska M, Jartych E, Calka A, and Michalak L, 2005, J. Alloys Compd., vol. 402, p256.

Song M Y, 1995, J. Mater. Sci., vol. 30, p1343.

Song M Y, Ivanov E I, Darriet B, Pezat M, and Hagenmuller P, 1985, Int. J. Hydrogen Energy, vol. 10, p169.

Song M Y, Kwon I H, and Bae J S, 2005, Int. J. Hydrogen Energy, vol. 30, p1107.

Song M Y, Manaud J P, and Darriet B, 1999, J. Alloys Compd., vol. 282, p243.

Ströbel R, Jörissen L, Schliermann T, Trapp V, Schutz W, Bohmhammel K, Wolf G, and Garche J, 1999, J. Power Sources, vol. 84, p 221.

Suda S, Sun Y M, Liu B H, Zhou Y, Morimitsu S, Arai K, Tsukamoto N, Uchida M, Candra Y, and Li Z P, 2001, Appl. Phys. A, vol. 72, p209.

Sun D, Gingl F, Enoki H, Ross D K, and Akiba E, 2000, Acta Mater., vol. 48, p2363.

Tanaka K, Kanda Y, Furuhashi M, Saito K, Kuroda K, and Saka H, 1999, J. Alloys Compd., vol. 293-295, p521.

Tao Z D, Geng H R, Yu K, Yang Z X, and Wang Y Z, 2004, Mater. Lett., vol. 58, p3410.

Terashita N, Takahashi M, Kobayashi K, Sasai T, and Akiba E, 1999, J. Alloys Compd., vol. 293-295, p541.

Tran N E, Imam M A, and Feng C R, 2003, J. Alloys Compd., vol. 359, p225.

U.S. Department of Energy, 2004, Basic Research Needs for the Hydrogen Economy, accessed 4/4/2005, http://www.sc.doe.gov/bes/reports/list.html.

U.S. Department of Energy, 2005, Quantum Fuel Systems Technologies Worldwide Project Report, accessed 5/5/2006, http://www.hydrogen.energy.gov/annual_progress05_storage.html.

U.S. Department of Energy, 2007, Multi-Year Research, Development and Demonstration Plan: Planned Program Activities for 2004-2015, accessed 6/6/2007, http://www1.eere.energy.gov/hydrogenandfuelcells/mypp/pdfs/storage.pdf.

Utgikar V P and Thiesen T, 2005, Technol. Soc., vol. 27, p315.

Vajo J J and Skeith S L, 2005, J. Phys. Chem. B, vol. 109, p3719.

Varin R A and Czujko T, 2002, Mater. Manuf. Proc., vol. 17, p129.

Varin R A, Li S, Calka A, and Wexler D, 2004, J. Alloys Compd., vol. 373, p270.

Vijay R, Sundaresan R, Maiya M P, Srinivasa Murthy S, 2005, Int. J. Hydrogen Energy, vol. 30, p501.

Vogt T, Reilly J J, Johnson J R, Adzic G D, and McBreen J, 1999, J. Electrochem. Soc., vol. 146, p15.

Wagemans R W P, van Lenthe J H, de Jongh P E, van Dillen A J, and de Jong K P, 2005, J. Am. Chem. Soc., vol. 127, p16675.

Wang F X, Gao X P, Lu Z W, Ye S H, Qu J Q, Wu F, Yuan H T, and Song D Y, 2004, J. Alloys Compd., vol. 370, p326.

Wang P, Orimo S, and Fujii H, 2003a, J. Alloys Compd., vol. 359, pL1.

Wang P, Orimo S, Tanabe K, and Fujii H, 2003b, J. Alloys Compd., vol. 350, p218.

Wang P, Wang A M, Ding B Z, Hu Z Q, 2002, J. Alloys Compd., vol. 334, p243.

Wang X L and Suda S, 1995, J. Alloys Compd., vol. 231, p380.

Warner M J, 2005, Low Cost, High Efficiency, High Pressure Hydrogen Storage; accessed 6/7/2007, http://www1.eere.energy.gov/hydrogenandfuelcells/pdfs/04_warner_quantum.pdf.

Welham N J, Berbenni V, and Chapman P G, 2003, J. Alloys Compd., vol. 349, p255.

Williamson G K and Hall W H, 1951, Acta Metall., vol. 1, p22.

Wong-Foy A G, Matzger A J, and Yaghi O M, 2006, J. Am. Chem. Soc., vol. 128, p3494.

Woo J H and Lee K S, 1999, J. Electrochem. Soc., vol. 146, p819.

World Bank, 2004, World Development Indicators.

Wu C Z, Wang P, Yao X, Liu C, Chen D M, Lu G Q, and Cheng H M, 2006, J. Alloys Compd., vol. 414, p259.

Xu W C, Takahashi K, Matsuo Y, Hattori Y, Kumagai M, Ishiyama S, Kaneko K, and Iijima S, 2007, Int. J. Hydrogen Energy, available online 22 January 2007.

Yang H B, Yuan H T, Ji J T, Sun H, Zhou Z X, and Zhang Y S, 2002, J. Alloys Compd., vol. 330-332, p640.

Yavari A R, de Castro J F R, Vaughan G, and Heunen G, 2003, J. Alloys Compd., vol. 353, p246.

Yavari A R, LeMoulec A, de Castro F R, Deledda S, Friedrichs O, Botta W J, Vaughan G, Klassen T, Fernandez A, and Kvick A, 2005, Scripta Mater., vol. 52, p719.

Ye H, Zhang H, Cheng J X, Huang T S, 2000, J. Alloys Compd., vol. 308, p163.

Ye Y, Ahn C C, Witham C, Fultz B, Liu J, Rinzler A G, Colbert D, Smith K A, and Smalley R E, 1999, Appl. Phys. Lett., vol. 74, p2307.

Yu X B, Wu Z, Xia B J, and Xu N X, 2004, J. Alloys Compd., vol. 372, p272.

Yu X B, Yang Z X, Feng S L, Wu Z, and Xu N X, 2006, Int. J. Hydrogen Energy, vol. 31, p1176.

Yu Z X, Liu Z Y, and Wang E D, 2002, Mater. Sci. Eng. A., vol. 335, p43.

Zaluska A, Zaluski L, and Ström-Olsen J O, 2001, Appl. Phys. A, vol. 72, p157.

Zaluska A, Zaluski L, and Ström-Olsen J O, 1999 a, J. Alloys Compd., vol.289, p197.

Zaluska A, Zaluski L, and Ström-Olsen J O, 1999 b, J. Alloys Compd., vol. 288, p217.

Zaluski L, Zaluska A, and Ström-Olsen J O, 1997, J. Alloys Compd., vol. 253–254, p70.

Zaluski L, Zaluska A, and Ström-Olsen J O, 1999, J. Alloys Compd., vol. 290, p71.

Zaluski L, Zaluska A, Tessier P, Ström-Olsen J O, and Schulz R, 1996, J. Mater. Sci., vol. 31, p695.

Zaluski L, Zaluska A, Tessier P, Ström-Olsen J O, and Schulz R, 1995, J. Alloys Compd., vol. 217, p295.

Zenner M and Pehr K, 2005, CLEFS CEA-No. 50/51-winter 2004-2005, p62.

Zhang S G, Hara Y, Morikawa T, Inoue H, and Iwakura C, 1999, J. Alloys Compd., vol. 293–295, p552.

Zhang Y S, Yang H B, Yuan H T, Yang E D, Zhou Z X, and Song D Y, 1998, J. Alloys Compd., vol. 269, p278.

Zhou L, Zhou Y, and Sun Y, 2004, Int. J. Hydrogen Energy, vol. 29, p475.

Zhu M, Wang H, Ouyang L Z, and Zeng M Q, 2006, Int. J. Hydrogen Energy, vol. 31, p251.

Zhu X, Birringer R, Herr U, and Gleiter H, 1987, Phys. Rev. B, vol. 35, p9085.

Züttel A, 2004, Naturwissenschaften, vol. 91, p157.

Züttel A, Nützenadel Ch, Sudan P, Mauron Ph, Emmenegger Ch, and Rentsch S, Schlapbach L, Weidenkaff A, and Kiyobayashi T, 2002, J. Alloys Compd., vol. 330–332, p676.

Züttel A, Wenger P, Rentsch S, Sudan P, Mauron Ph, Emmenegger Ch, 2003, J. Power Sources, vol. 118, p1.

Züttel A, Wenger P, Sudan P, Mauron P, and Orimo S, 2004, Mater. Sci. Eng. B, vol. 108, p9.

Acronyms

BCC: body centered cubic

CGH_2: compressed gaseous hydrogen

CHN: carbon-hydrogen-nitrogen

CNT: carbon nanotube

CUTE: clean urban transport for Europe

CV: cyclic voltammogram

DSC: differential scanning calorimeter

EDS: energy dispersive x-ray spectroscopy (EDS)

EEA: European Environment Agency

EIS: electrochemical impedance spectra

FWHM: full-widths at half-maximum

GNF: graphite nanofibre

IEA: International Energy Agency

IPCC: intergovernmental panel on climate change

IR: infrared

LH_2: liquid hydrogen

LTOF MS: linear mode of time-of-flight mass spectrometry

MA: mechanical alloying

MM: mechanical milling

MOF: metal organic framework

MWCNT: multi-walled carbon nanotube

PCT: pressure-composition-temperature

RMA: reactive mechanical alloying

RMM: reactive mechanical milling

RT: room temperature

SAED: selected area electron diffraction

SEM: scanning electron microscope

SSA: specific surface area

SWCNT: single-walled carbon nanotube

TEM: transmission electron microscopy

TG: thermogravimetry

TM: transition metal

TMO: transition metal oxide

U.S. DOE: U.S. Department of Energy

XPS: X-ray photoelectron spectroscopy

XRD: X-ray diffraction

Publications

Journal papers:

1. **Z.G. Huang**, Z.P. Guo, H.K. Liu, S.X. Dou

Effect of Ni Content on the Structural and Electrochemical Properties of the $Mg_{1.9}Cu_{0.1}Ni_x$ hydride alloys, J. New Mater. Electrochem. Systems, 8 (2005) 283-289.

2. Z.P. Guo, **Z.G. Huang**, Z.W. Zhao, X. Menard, H.K. Liu

Enhanced Electrochemical Properties of Nonstoichiometric Amorphous $Mg_2Ni_{1.3}$ Electrodes, J. Appl. Electrochem., 36 (2006) 11-16.

3. **Z.G. Huang**, Z.P. Guo, A. Calka, D. Wexler, C. Lukey, H.K. Liu

Effects of iron oxide (Fe_2O_3, Fe_3O_4) on hydrogen storage properties of Mg-based composites, J. Alloys Compd., 422 (2006) 299–304.

4. Z.P. Guo, S.H. Ng, J.Z. Wang, **Z.G. Huang**, H.K. Liu, C.O. Too, G.G. Wallace

Electrochemical Hydrogen Storage in Single-Walled Carbon Nanotube Paper,
J. Nanosci. Nanotechnol., 6 (2006) 713-718.

5. **Z.G. Huang,** Z.P. Guo, A. Calka, D. Wexler, H.K. Liu

Effects of carbon black, graphite and carbon nanotube additives on hydrogen storage properties of magnesium, J. Alloys Compd., 427 (2007) 94–100.

6. Z.P. Guo, L. Yuan, K. Konstantinov, **Z.G. Huang**, H.K. Liu

Preparation of spherical clusters of metal oxide nanorods and their hydrogen storage behavior, Mater. Lett., 60 (2006) 3891–3894.

7. **Z.G. Huang**, Z.P. Guo, D. Wexler, K. Konstantinov, H.K. Liu

Thermal stability and hydrogen storage property of $Mg_{1.9}Cu_{0.1}Ni_x$ (x = 1.8, 1.9, 2.0 and 2.1) alloys, J. Alloys Compd., 426 (2006) 335–340.

8. Z.P. Guo, **Z.G. Huang,** K. Konstantinov, H.K. Liu and S.X. Dou,

Electrochemical hydrogen storage properties of nonstoichiometric amorphous $MgNi_{1+x}$–carbon composites (x = 0.05–0.3), Int. J. Hydrogen Energy, 31 (2006) 2032 – 2039.

9. **Z.G. Huang,** A. Calka, H.K. Liu

Effects of milling conditions on hydrogen storage properties of graphite, J. Mater. Sci., 42 (2006) 5437-5441.

10. **Z.G. Huang**, A. Calka, H.K. Liu

DSC study of the effect of milling conditions on the hydrogen storage properties of boron, J. Mater. Sci., 42 (2006) 3985–3989.

11. **Z.G. Huang**, Z.P. Guo, A. Calka, D. Wexler, H.K. Liu

Improvement in hydrogen cycling properties of magnesium through added graphite, Mater. Lett., 61 (2007) 3163–3166.

12. **Z.G. Huang**, Z.P. Guo, A. Calka, D. Wexler, J. Wu, P.H.L. Notten, H.K. Liu

Noticeable improvement in the desorption temperature from graphite in rehydrogenated MgH_2/graphite composite

Mater. Sci. Eng. A, 447 (2007) 180–185.

Conference papers

1. **Z.G. Huang**, Z.P. Guo, D. Wexler, K. Konstantinov, H.K. Liu

Correlation between thermal stability and hydriding property of $Mg_{1.9}Cu_{0.1}Ni_x$ (x = 1.8, 1.9, 2.0, 2.1) alloys, 18th NCTA/VSA conference, 2005, New Zealand

2. **Z.G. Huang**, Z.P. Guo, D. Wexler , A. Calka, H.K. Liu, S.X. Dou

Composites for hydrogen storage synthesized by Controlled Reactive Mechanical Ball Milling (CRMBM) of carbon allotropes and magnesium in hydrogen, Proceedings of World Hydrogen Technologies Conference, 2005, Singapore

3. Z.P. Guo, S.H. Ng, J.Z. Wang, **Z.G. Huang**, H.K. Liu

Single-Walled Carbon Nanotube Only Electrodes for Electrochemical Hydrogen Storage, Proceedings of World Hydrogen Technologies Conference, 2005, Singapore

4. **Z.G. Huang**, Z.P. Guo, A. Calka, D. Wexler, H.K. Liu

Reactive ball milling used to fabricate hydrogen storage materials, Proceeding of Australian National Science Graduate Conference, 2006, Sydney, Australia.

5. **Z.G. Huang**, Z.P. Guo, A. Calka, H.K. Liu

Fabrication of hydrogen storage materials using a special controlled reactive ball milling, Alternative Transport Energies Conference, 2006, Perth, Australia.